Computerised Image Analysis of Changes in Bone Architecture in Arthritic Disease

By

Matthew McArthur Neilson

A thesis presented for the degree of

Master of Medical Science (September 2001).
Faculty of Medicine.
University of Glasgow.

CONTENTS

The human hip

Glossary and Appendices

Glossary - Definition of image analysis terminology
Appendix A - Image analysis macro – femoral head
Appendix B - Image analysis macro – femoral neck
Appendix C - Image analysis macro – Heberden's nodes
Appendix D - Modified van Gieson stain

Acknowledgements

I would like to express my heartiest thanks to my project supervisor, Dr. Stuart McDonald, for his help, advice and guidance during this project.

I am also indebted to Professors JC McGrath and AP Payne for allowing me the opportunity to complete this project.

I would also like to thank Dr. IG Logan, Dr. CJ Daly, Mr. J McGadey, Mr. D Russell, Mr. A Lockhart, Mr. G Neilson, Dr. E Morrison, Ms. L McAlpine and Ms. U Malik for their help and support.

Lastly, I would like to thank my wife Eleanor and sons Jamie and Donnie for their love, support, encouragement, patience and understanding and for just being there.

Declaration

I declare that the work contained within this thesis has been by myself, Mr. Matthew McArthur Neilson, under the supervision of Dr. Stuart McDonald and that it has not been presented in whole or in part to any other university before.

List of abbreviations

3D	Three-dimensional.
BSE-SEM	Backscattered electron imaging analysis in a scanning electron microscope.
CCD	Charge coupled device.
CM	Confocal microscope.
DEXA	Dual energy X-ray absorptionometry.
DIP	Distal interphalangeal.
EDTA	Ethylenediaminotetra-acetic acid.
LUT	Look up table.
Micro-CT	Microcomputed tomography.
OA	Osteoarthritis.
OP	Osteoporosis.
PDT	Point dependent thresholding.
QCT	Quantitative computed tomography.
ROI	Region of interest.
SEM	Scanning electron microscope.
RA	Rheumatoid arthritis.
RAM	Random access memory.
VEL	Virtual environment laboratory.
VRCLSM	Video rate confocal laser scanning microscopes.

List of figures, table and charts **Page No.**

Summary

The development of computerised image analysis techniques with modern microscopy has allowed for more diversity in methods of collecting and collating quantitative data from biological material. This project is concerned with the development of computerised image analysis techniques, developed on the Kontron VIDAS image analyser, used to extract morphometric information from osteoarthritic bone specimens. The study also investigates and quantifies bias and random error, the effects of magnification, scaling, focusing, thresholding and inter- and intra-user variability, when developing an image analysis macro.

Osteoarthritis of the human hip results in bony changes within the femoral head and neck in both force-transmitting and non-force-transmitting regions. Image analysis macro programs were written to help quantify these changes. Separate macros were necessary to quantify the distribution in both the femoral head and neck. Five osteoarthritic hips were obtained from patients undergoing total hip replacement and five control hips were obtained from dissecting room subjects.

The femoral head macro measured the area of intertrabecular spaces within each of four divisions of a region of interest taken from a photograph of a dried coronal slice of the femoral head. The femoral

neck macro was used to measure the distribution of cortical and medullary bone in van Gieson-stained transverse sections through the upper femoral neck. The neck macro attempted to automate the process as much as possible. The distribution of bone was measured by implementing an automated method in which the computer divided the cortex into 12 sectors. The medullary bone was automatically divided into 25 sectors. The sectors were created by radiating lines plotted from a centroid at 30° intervals. The radiating lines were intersected by two computer calculated concentric rings.

Clearly defined image analysis operator protocols and adequately trained operators are required to ensure reproducibility. To avoid fractal effects distorting the data, if possible all specimens in an experiment should be measured using the same scale and magnification.

Compared to controls the intertrabecular spaces in the femoral heads of osteoarthritic specimens were smaller in the compressive areas. In addition, bony trabeculae in the inferior parts of the head were sparser, which may be in response to a remodelling process to redistribute the load forces. The analysis of the osteoarthritic femoral neck shows that the cortical bone thickens at the inferior aspect and the trabecular bone volume is reduced. This suggests differential bone deposition and resorption in osteoarthritis.

This study is the first to correlate architectural changes in the osteoarthritic femoral head with architectural changes in the femoral neck in specimens obtained from the same subjects.

Heberden's nodes are clinical swellings seen at the distal interphalangeal (DIP) joints when they are affected by osteoarthritis. They are associated with bony spurs at the DIP joints. This project develops a purpose-written image analysis macro to determine the midline on radiographs of distal and middle phalanges radiographed in the posteroanterior and lateral planes. The computed midline was used to determine the extent of abnormal growth on either side of the midline. It was shown that specimens with severe Heberden's nodes exhibited substantial enlargement on both distal and middle phalanges and that these changes occur as a result of *localised* bony changes.

Introduction

Introduction

Historical overview of image analysis

When a relationship between the volume fraction of a randomly distributed phase or object within a multiphase solid was shown to correspond with the sectioned area fraction of that phase (Delesse, 1847), the door was opened into the world of image analysis. It was not long before scientists saw the enormous benefits that Delesse's observation had made possible.

Stereology

The exploration of three-dimensional (3D) space from two-dimensional (2D) sections is given the term stereology. The number of different stereological methods that have been developed are varied and vast, but they are all based on statistically exact expressions that relate points, lines, surfaces and volumes in space to measurements made on 2D sections. The methods employed in stereology require that unbiased random sampling is used. Stereology usually uses superimposed points or intercept lines (Howard & Cohen, 1948) on an image to derive area and then volume estimates. The measurement of these points or lines must be made randomly or with statistical uniformity. The preciseness of the estimated area or volume is dependant on the number of measurements taken.

Volume fraction (V_v) can be estimated by point counting, lineal analysis (measurement of lineal intercepts) or areal analysis (measurement of areas). Early workers employed areal measurement methods such as photographing the specimen and then cutting around the object and weighing it. These objects could be compared to the weight of the whole photograph and the area fraction calculated. The technique of drawing objects on to graph paper and counting the boxes was also frequently used. These methods were superseded by faster and more accurate methods. Since the advent of computer systems the use of areal methods has again become popular.

This study will use areal analysis.

Digital image analysis

Digital image analysis has only been possible since the late 1960's, with the first utilisation of electronic systems (Joyce-Loebl, 1985). Digital image analysis can be described as a method of extracting quantitative information from an image by digitally processing the image followed by some form of '*classification*' (logical sorting of image data into definable differentiated bins). It is used in many different fields including biomedical sciences, material sciences, astronomy, quality control and military defence. These image-measuring techniques are only possible with some kind of computer or processor.

From the early 1970's we saw the introduction of manual systems, such as the Kontron Manual Optical Picture Analyser (MOP1,2 & 3), very basic by today's standards, and very expensive, thus restricting their use to a few scientists. These basic systems usually took the form of a digitising plate, an electronic pen and a control processor unit. The user would place a photograph on the tablet and either draw around an object of interest, count objects or mark two or three points for a distance or angular measurement. No actual image was digitised. Only a digital measure of the object could be stored in a volatile memory. These machines were capable of storing a scale, so that the output could be in mm or mm^2 for lengths and areas respectively. They may also have had a few programmed calculations stored in the machine, for the user to obtain derived measurements i.e. a circularity factor. Although these machines were basic, they were a great improvement on previous methods, particularly on the time saved to collect data.

Digital image analysis has only been feasible on any real scale since the mid 1970's. Systems from the mid 1970's up to early 1990's were purpose built proprietary machines, such as the Kontron Elektronik IBAS and the Vision GOP 300 systems (Wootton et al, 1995). These systems were still relatively expensive compared to the systems of today. These image analysers employed an array processor (a device that spreads processor tasks to two or more processors. This will increase the computational capabilities of the computer) specially optimised for image processing (Wootton et al, 1995). These types of system were the first to incorporate a digital frame grabber, which would digitise images, via a monochromatic analogue camera. A visual display unit (VDU) could display the image. Now that it was possible to have an image in the digital domain, within the computer's memory, what is termed 'image processing' was now feasible. Image processing is when operations are performed on a digital image that changes the '*pixel*' values in some way. This can be done to make the image more interpretable to the human eye, or as the precursor to isolating an object within an image.

Modern image analysers

The advent and evolution of the personal computer (PC), from the late 1980's, brought an increase in affordable computing power. Today image analysers are usually not proprietary systems. Most image analysis software can be installed on any appropriately specified PC, which may even be used for non-image analysis purposes. The software cost is still relatively high compared to non-specialist software. This is due to the relatively low number of units sold and the need for the manufacturers to regain their considerable research and development costs. Today's image analysis systems are fast, reliable and cheap, thus enabling purchase by any reasonably funded researcher or research group.

Most modern image analysis systems offer some form of '*interpreter*' (programming language), to enable the machine to repeat imaging tasks.

The interpreter produces small programmes called *'macros'*. These can be extremely powerful and enable very complex and automated operations to be carried out e.g. the automatic processing of sequentially named images utilising a *'variable'* automatically calculated from a grey density measurement which is then used to automatically *'threshold'* the image, the macro could then take measurements and then move on to the next stored image. After the macro has been written, these complex operations can be carried out by a non-image analysis expert by simply running the macro. Today the uses for image analysis in the biomedical field are wide and varied and are increasing at an exponential rate (Wootton et al, 1995).

This study explores how an image analysis system, the Kontron Elektronik VIDAS, can be employed to extract complex morphometric information from bone specimens. Although the morphometric data obtained during this study are important to arthritic disease research, and will be reported and considered, the emphasis of the project will be on the development of image analysis techniques and the mechanics of how the data were obtained. Another main emphasis will be to investigate system bias and inter and intra observer error.

This study uses an image analysis system to extract morphological information from bone, with particular emphasis given to the analysis of the distribution of bone in the human femoral head/ neck and around the distal interphalangeal (DIP) joint of the finger in osteoarthritis.

These sites were chosen as tissue from hip replacement surgery was readily available and cadavers from the Anatomy department's dissecting room could provide the finger specimens. Also, surgeons have often reported that fracture of the femoral neck rarely occurs in patients with osteoarthritis.

Arthritic disease

A survey carried out in the United States of America for the years 1995-1996 showed that arthritic disease was the most prevalent chronic condition among adults aged over 65 years (49%), followed by hypertension (40%) and heart disease (28%) (Desai et al, 1999).

Osteoarthritis

The arthritic disease relevant to this study is osteoarthritis (OA), which was formerly referred to as osteo-arthrosis and degenerative joint disease. OA involves the degeneration of articular cartilage together with changes in subchondral bone. OA is a group of overlapping distinct diseases which may have different etiologies but share similar biological, morphological and clinical outcomes (Keuttner & Goldberg, 1995).

OA is the most common form of arthritis worldwide and is a significant health problem, owing to the progressive and debilitating nature of the condition, which results in high morbidity and a marked decrease in the quality of life. OA is a major source of disability in the elderly, potentially equalling that associated with cardiovascular disease or stroke. Surveys in the United States of America suggest that OA affects over 16 million Americans and incapacitates 2 - 6% of their general population (Felson, 1993). The radiological features associated with the disease increase in frequency with age. Symptoms occur most commonly after the age of 45. Over 50% of the general population over 65 years show radiographic evidence of the disease. This increases to 80% over the age of 75 years (Lawrence et al, 1989).

Symptoms of OA are usually limited in distribution and commonly affect only one joint. Heberden's and Bouchard's nodes at the distal and proximal interphalangeal joints, respectively of the fingers, characterise hypertrophic generalised OA. Unlike other forms of the disease Heberden's and Bouchard's nodes are more prevalent in women (Stecher, 1941) and may reflect occupational injury (Acheson et al, 1970, Hadler et al, 1978,). OA of the knee affects 11% of people over 64 years (Felson & Zhang, 1998). OA of the hip is common and affects approximately 20% of people over 55 years (Kellgren, 1961). The disease also affects other load bearing joints (Silberberg, 1990) but instances affecting the wrist and shoulder are uncommon, although OA of the elbow has been reported in men (Hough, 1983) who have engaged in heavy manual work.

The pathogenesis of osteoarthritis

Little is known of the pathogenesis of the disease and there is much debate as to the early mechanisms of the disease. Many studies have been carried out to try and determine the roles of mechanical factors and chondrocyte dysfunction in the propagation of the disease.

Mechanical forces - Investigations into the effects of repetitive forces being applied across a joint have reported thickening of the subchondral bone (Radin & Paul, 1970). Trabecular bone remodelling results in the bone being less able to absorb impact and subsequently leads to cartilage damage (Radin & Paul, 1971). This idea revived the old concept that primary OA is a wearing out of the joints, but is due to repetitive impact loading, rather than rubbing (Radin, 1972). Further studies confirmed the idea that progression of cartilage lesions probably requires stiffened subchondral bone (Radin & Rose, 1986, Ampe et al, 1986, Layton et al, 1988). Repetitive impulse loading also causes vascular changes in subchondral bone, which are related to the magnitude and the rate of loading (Farkas et al, 1987). Bone mass increase and the subsequent stiffening of the bone in response to repetitive loading would seem to be accepted, but whether this is the absolute and only precursor to articular cartilage damage is debatable.

The influence of loading velocity on the stiffness of the articular cartilage has also been investigated (Fazzalari et al, 1990, Oloyede et al, 1992) and suggests that articular cartilage becomes stiffer and likely to cause changes in the pattern in which joint stresses are transmitted to the subchondral bone. The relationships between changes in the articular cartilage and bone in the femoral head are contradictory to the idea that stiffening of subchondral bone precedes damage to the articular cartilage. These studies suggest the initial damage to be an alteration in the articular cartilage matrix. It is still unknown whether the damage to the articular cartilage is due to the effects of subchondral bony changes or that the subchondral bony changes are a consequence damage to the articular cartilage.

More recently it has been reported that abnormalities of the cartilage surface did not consistently proceed remodelling at the attachment to the subchondral plate. This observation throws into question the concept that osteoarthritis has a single pathogenesis (Gannon & Sokoloff, 1999).

Biochemical changes - It is accepted that the proteoglycan content of the matrix in OA is depleted (Bollet et al, 1963, Mankin & Lippiello, 1970). As macromolecules, proteoglycans provides most of the ionic charge within the cartilage. As the proteoglycan depletes the amount of ionic charge goes down. As water binds to the proteoglycans by hydrogen bonding and by hydrophobic inclusion, this should imply a corresponding drop in the water content of the cartilage. Paradoxically the water content of the cartilage increases. This may be caused by the depleted proteoglycan permitting water to bind to the collagen fibres with greater affinity (Jaffe et al, 1974). This depletion of proteoglycans is accompanied by an increase in proteoglycan production, by up to twice that of normal cartilage (Mankin & Lippiello, 1970). The depletion of proteoglycans and subsequent increase in production could promote osmotic stress, which results in fissuring and degeneration of the articular cartilage. Collagen has also been shown to have increased production levels in osteoarthritic cartilage (Lippiello et al, 1977).

The rate at which the proteoglycans deplete has been shown to correlate with rate and pressure applied during mechanical loading in anatomically intact cartilage. (Muller & Hanschke, 1998).

Topographical variation of proteoglycan levels has been shown through the articular cartilage of the head of the femur. The weight-bearing cartilage of the superior region has a higher glycosaminoglycan content and lower water and collagen content than the cartilage at the periphery and below the fovea. Fibrillated cartilage both from the inferior and superior perifoveal areas have been shown to have a reduced glycosaminoglycan content and higher water content than normal cartilage (Venn, 1979).

Mass spectrometry has recently been used for the structural analysis of proteoglycans in cartilage (Zaia et al 2000). This may be of use in determining any posttranslational modification of these molecules in osteoarthritis.

Chondrocyte function – Chondrocyte division only occurs in response to acute or chronic conditions, as could be caused by repetitive mechanical loading on the joint (Mankin & Lippiello, 1970). The mechanisms by which chondrocytes do this is not fully understood and is being studied by many biochemical research groups working in osteoarthritis. Studies on cartilage explants at high rates of loading have documented chondrocyte cell death which are adjacent to surface lesions (Yyen-Tiesma et al, 1999). Recently, cell death at high and low rates of mechanical loading has been measured and confirms that the distribution of dead cells during high mechanical loading is predominantly at the fissure site, but more cells die at low mechanical loading and exhibit a more diffuse distribution (Ewers et al, 2001). Biochemical changes in the articular cartilage can adversely affect the cell environment, which alters chondrocyte activity. Chondrocytes control the turnover of the matrix proteins that give the cartilage its functional properties. It has been shown recently that the maturation of chondrocytes in osteoarthritic patients is slowed and that there is a loss of normal cell structure and evidence of matrix breakdown (Corvol, 2000).

It may be the case that if any factor (biochemical, cellular or mechanical), or combination of factors, disrupts the equilibrium of the joint's repair process, then this will lead to clinical osteoarthritis (Sokoloff, 1979).

Heberden's nodes

Definition – Heberden's nodes are swellings at the distal interphalangeal joints of the fingers. They indicate osteoarthritis at the distal interphalangeal joints and may signify a predisposition to osteoarthritis at other joints.

Heberden's nodes were first described by William Heberden (1710-1801), an eminent London physician. Throughout Heberden's medical career he kept detailed notes of his observations. Each month he would add and review his writings in what was to become known as "Commentaries on the History and Cure of Diseases", which was published by his son, after his death, in 1803. Included in this work was a chapter on "Nodi Digitorum" in which he reported, "little hard knobs, about the size of a small pea, which are frequently seen upon the fingers, particularly a little below the tip, near the joint. They have no connexion with gout, being formed in persons who never had it." (Heberden, 1803).

Heberden's nodes can be classified into two types:

Traumatic Heberden's nodes – These are the result of a direct injury to one or more of the fingers. After injury the finger swells and is painful for a few days to weeks. The bone becomes enlarged and within a few months it reaches a stationary condition and no further change takes place.

Idiopathic Heberden's nodes – This is the most important form of Heberden's nodes. The direct cause has not been identified. The nodes appear spontaneously, starting usually in one forefinger and gradually spreading to other or all fingers on both hands. The nodes develop slowly and rarely appear before the age of 40 years (Stecher, 1941). In Western populations OA affecting the hands is observed in 70% of people over the age of 65 years (Van Saase et al, 1989). Heberden's nodes are much more common in women. Women are between ten to twenty times more likely to have idiopathic Heberden's nodes than men (Stecher, 1941).

Idiopathic Heberden's nodes have a hereditary diathesis. Mothers of subjects are twice as likely and sisters are three times as likely as the general population, to have Heberden's nodes (Stecher, 1941).

OA is usually regarded as a non-inflammatory disease. However, some clinical and pathological features of Heberden's nodes suggest an inflammatory component. Production of hydroxyapatite crystals have been suggested as a possible explanation of this inflammation (Dieppe et al, 1976). This inflammatory component has been described as one of the two phases of idiopathic Heberden's nodes. An initial inflammatory phase is followed several months later by the chronic phase, characterised by osteophytes around the DIP joint (Kellgren & Moore 1952).

Osteophytes are swellings of the bone, sometimes referred to as spurs, and are a main pathological indicator of OA. Osteophyte size has been reported to increase with the overall degeneration of the joint (Altman et al, 1987). The osteophyte can be regarded as an attempt to enlarge the load-bearing surface, thereby reducing the overall pressure on the joint (Radin et al, 1972). These spurs can interfere mechanically with the normal operation of the joint. Quantitative studies have shown that the number and size of osteophytes in the hand were greatest at the joint margins, rather than at sites of ligamentous attachments and were more prevalent in the dominant hand and at the sites associated with grasping or grip (Buckland-Wright et al, 1991).

Radiography of the DIP joint

Investigations into the morphological changes, which occur in the DIP joint during OA, have been carried out to try and shed more light on the pathogenesis of hypertrophic generalised arthritis.

Standard radiography - First used to create a standard for the identification of OA by Kellgren and Lawrence in 1957. This work was refined and expanded by Altman and co-workers (1986), who also suggested a further method to assess the progression of the disease (Altman et al, 1987). Standard radiography has been used to measure the joint space gap, reduction of which is regarded as a sign of cartilage loss (Altman et al, 1987, Resnick et al, 1988). The use of digital image analysis to measure the joint space in standard X-rays of the knee has shown that rapid, reliable and accurate measurement of joint space size can be achieved (Dacre & Huskisson, 1989). Standard radiography is cheap, easily accessible and well understood. The disadvantages are that no radiographic magnification is possible and that the bony margins can be difficult to visualise (Buckland-Wright, 1994). Accepting the limitations of standard radiography, its use in the clinical assessment of the disease is still preferred and is more accurate than clinical examination alone (Hart et al, 1994).

Newer digital radiographic machines are now available. These machines produce digital images, which are more practical for archive purposes, data transmission and integration into image analysis software. A recent study has shown that resolution can be increased by up to 60% over that achieved by conventional systems (Amendolia et al, 2001).

Microfocal radiography – The extremely small X-ray source, of microfocal X-ray machines, allow radiographs to be taken at high magnification and fine detail. The machine can resolve objects as small as 25μm due to its magnification ceiling of up x20 (Buckland-Wright, 1989). The use of this machine in assessing OA of the hand has been led by Buckland-Wright and co-workers. They have demonstrated how the extra definition, made possible by microfocal radiography, can be used to quantify features at almost histological levels, such as the quantitative assessment of osteophyte incidence, size distribution and progression (Buckland-Wright et al, 1990, Buckland-Wright et al, 1991).

Bone architecture and the image analyser

Bone architectural changes have been implicated in the pathogenesis of OA (Pritzker, 1998). An invaluable tool, used to investigate and analyse these changes, is the image analyser. Cancellous bone microstructure is a complex arrangement of plates and bars with variable orientation, where connectivity is a feature of structure (Compston, 1994). Studying the effects of disease on the morphology of bone can reveal useful knowledge on the aetiology and pathogenesis of the disease. Studying the complex morphology of bone can be greatly enhanced by employing image analysis techniques.

Image analysis

Use of an image analyser to quantify bone structure in a greylevel image is now widely utilised (Fazzalari, 1980). Potential pitfalls when using an image analyser must be considered: detection of contaminants, over or under segmentation of bone, operator bias and the working magnification. Good specimen preparation and consistent training for the operators can help to minimise these problems (Parkinson & Fazzalari, 1994). Pre-experimental testing should be carried out to examine the effect that the operator may have on the results.

The detection by segmentation of contaminants, such as non-specific staining of the bone marrow, is usually unavoidable, but with well-designed binary image processing techniques, designed to eliminate artefacts, these contaminants can be easily removed.

When manually thresholding trabecular bone, on a well-prepared section, it has been shown that a target of ± 2 grey levels should be achievable (Parkinson & Fazzalari, 1994).

The magnification used when comparing different bone specimens should, if possible, be the same for all specimens (Parkinson & Fazzalari, 1994). The relationship between the measured perimeter and the measuring step-size (length of the measuring ruler) changes with magnification. As the magnification increases, the relative step-size decreases which results in the measured perimeter increasing, although the area remains constant (Weibel, 1979). The degree of increased perimeter measurement, as step-size decreases with increased magnification, will be dependent on the level of magnification change from a defined starting magnification. This will effect all digitally measured perimeter measurements. Depending on which method the image analysiser uses to calculate the area of an object, digitally measured area can also be affected, albeit by a lesser amount.

Bone architecture

Since Wolff (1892) formulated that every change in the function of bone was followed by certain definite changes in the internal architecture, researchers have been employing different methods to try to measure and quantify these changes. The morphology of bone is extremely complex and workers have used many different image analysis methods to try and extract useful morphometric information on how the architecture changes through the course of an arthritic disease. The most popular sites of study are: iliac crest, femoral head, vertebra and the DIP joint.

Most of the image analysis studies carried out on bone specimens pertain to osteoporosis (OP) research. Some of the techniques used may be of relevance to OA. Methods developed to measure bone architecture in one particular arthritic disease or to measure a bone specimen from a particular anatomical site, may or may not be applicable for the study of specimens from another arthritic disease, or from a different anatomical site. The preparation of the specimen (Parkinson & Fazzalari, 1994), may also affect the method, or methods, used to measure bone architecture.

The two-dimensional image analysis of bone is predominantly carried out on histological sections, although useful information in the assessment of fracture risk has been obtained from the texture analysis of trabecular bone in high-resolution computed tomography (HRCT) images (Mundinger et al, 1993). Ground sections (Edmonston et al, 1994) have been used, but these are extremely time consuming to produce. Photographs of gross specimens and X-Ray plates, from standard or microfocal radiography, have also been used for image analysis (Altman et al, 1987; Buckland-Wright et al, 1990).

Some studies have correlated quantitative image analysis with dual energy X-ray absorptiometry (DEXA) scans to try and produce more accurate methods of interpreting DEXA scans (Grotz et al, 1994).

Three-dimensional (3D) image analysis is now feasible. Before any analysis in 3D can begin, 3D image data must be collected.

Scanning electron microscopy (SEM) has been used for the many years as a method to analysis the architecture of bone, but obtaining morphometric data has been difficult, although low resolution SEM has been able to extract meaningful data (Boyde & Jones, 1996). SEM produces a 2D image of a 3D structure and is therefore limited in the true 3D morphometric data that can be obtained.

More recently, techniques that use quantitative backscattered electron imaging analysis in a scanning electron microscope (BSE-SEM) have be used to sample a thin (0.5 - 1 μm) surface layer from a bulk specimen (Boyde et al, 1993; Howell & Boyde, 1994; Kingsmill & Boyde, 1998). This technique is usually used to measure the mean bone mineralisation density by measuring the mean grey levels of objects in the produced images, thus may be used as an indicator of bone loss. The BSE-SEM can also be use to record detailed morphological images over a range of magnifications.

Microcomputed tomographic (Micro-CT) techniques are now starting to be used (Kinney et al, 1995).

More recently, researchers have been exploring the use of confocal microscopy (CM) and fluorescence labelling to analyse thick bone sections. Researchers have been able to reconstruct and analyse micro-cracks in trabecular bone (O'Brien et al, 2000) using CM.

The introduction of the video rate confocal laser scanning microscopes (VRCLSM) used in reflection mode enabled workers to study morphological changes in bone containing living cells. Osteoclastic resroption could be studied and the areas and volumes of resorption pits measured (Kingsmill et al, 1999; Kingsmill et al 2000).

To obtain absolute 3D morphometric measurements, such as volume and surface area, the 3D structure must exist in the digital domain. Stereological methods will only ever estimate on an average or typical structure. Stereological methods do not reveal the existence of individual variation among examples of a structure (Parsons et al, 1990).

In OP research, image analysis methods have been developed to measure the bone architecture of iliac crest biopsies. These methods may or may not be of use in the study of other arthritic diseases. Using tissue obtained from iliac crest biopsy has obvious advantages, but so far has only been shown to be useful in OP research. No correlation has been found which would allow iliac crest biopsies to be used to assess bony changes in femoral OA (Fazzalari et al, 1992).

Trabecular bone connectivity

Much work on the architecture of bone in OP centres around methods used for measuring trabecular bone and, in particular techniques to quantify the connectivity of the bone.

Many different methods to extract morphological information from trabecular bone have been offered, with the emphasis on measuring connectivity of bone. Most have their own unique merits but none are exempt from criticism.

Star volumes – This is an extremely time consuming and complicated method involving the superimposing of chords (sine weighted radiating lines) within the marrow space. The star volume is defined as the mean volume of all parts of an object that can be seen, un-obscured in all directions from a point inside the object (Serra, 1982). The chords are calculated and drawn by the image analyser from randomly produced points within the marrow space. In trabecular bone the star volume of the marrow space gives an estimation of the mean size of marrow space in three dimensions, giving a measure of connectivity (Vesterby et al, 1989). As well as being time consuming and complicated, errors can be caused by the radiating lines not meeting an object before they leave the section boundary. In practice, the validity of this method for use in measuring trabecular bone remains unproven (Compston, 1994).

The technique of star volume has recently been extended to consider the mean surface-weighted star volume (Reed & Howard, 1998), defined as the volume of a continuous phase seen un-obscured from a typical point within the interface of the phase. The point of interest is allowed to move over all possible positions on the interface of the phase and the average taken of the individual star volumes measured. Although the technique was demonstrated on piglet lung tissue, it could easily be applied to cancellous bone.

Trabecular bone pattern factor – This is an ingenious method for measuring connectivity utilising the relationship between concave and convex structures that exist within the bone. If the bone has many concave elements, this reflects high connectivity and if it has many convex structures this will indicate that trabeculae have few connections. This is a two-dimensional method (Hahn et al, 1992). The method works by measuring the perimeter of a binary image of the trabeculae. A dilation is then applied and the perimeter is measured again. After dilation a structure with a concave element will have a reduced perimeter and a structure with a convex element will have an increased perimeter. The area of the dilation reduction or dilation increase is measured and the following formulae applied:

$$TBPf = \frac{P1 - P2}{A1 - A2}.$$

Where: P1 is the original perimeter.

P2 is the dilated perimeter.

A1 is the original area.

A2 is the dilated area.

One of the advantages of this approach is that artefact bone separation produced by tissue processing does not affect the overall measurement of connectivity. As these artefacts are usually cracks across the bone which are neither concave or convex, they will not contribute to the calculation. The method has several disadvantages: all specimens must be analysed at the same magnification, comparisons between different bones are difficult, the best degree of dilation can be difficult to attain as too much dilation will connect objects and too small a dilation will result in missing small objects and the use of different smoothing filters can adversely affect the values measured (Flautre & Hardouin, 1994).

Fractal analysis – Many natural objects, when observed with different magnifications, show invariance in perimeter shape. If a biological structure can be shown to exhibit this phenomenon the level of self-similarity can be measured (fractal dimension). Although many researchers have reported a level of self-similarity in biological structures including the bronchial tree and coronary arterial trees

(West, 1990), the evidence of whether the internal structure of bone has a high enough fractal index to be useful for the measurement of connectivity is debatable. Conventional Euclidean geometry cannot be used to describe boundary length and perimeter roughness. These elements can only be described by using fractal geometry. Trabecular bone, from the iliac crest, was calculated to have a fractal dimension of 0.99. This value is not greater than the topological dimension of 1, thus trabecular bone does not have a fractal structure (Cross et al, 1993), so fractal techniques are in appropriate for its analysis.

Strut analysis – A novel approach to determining connectivity was described in 1986 (Garrahan et al) based upon the topological classification of trabeculae, which are divided into struts linked by defined nodes. This method requires that the binary image of the trabeculae is *skeletonised* (binary image eroded or thinned down to a single pixel in thickness) before measuring. The binary skeleton of the trabecular network is then manually analysed (Mellish et al, 1991) by counting the different types of strut as defined by: node-to-node, node-to-loop, node-to-free-end, free-end-to-free-end and cortex-to-free-end strut. This method can be time consuming and is known to be strongly influenced by local surface variations. Artefacts can be introduced when termini with one or more struts are produced by the sectioning procedure and conversely the node-to-loop struts, which are an indicator of connectivity, cannot be created artefactually (Compston, 1994).

Euler-Poincaré's number – This is a stereological method of estimating the connectivity by counting the number of holes in a structure. This topological property can be applied to any two or three-dimensional analysis (Compston, 1994). In the two-dimensional analysis of trabecular bone, the number of enclosed medullary cavities m and the number of the connected trabeculae n are used to calculate the Euler-Poincaré's number E as:

$$E = n - m.$$

Bones with high connectivity will have a low E value. E is always a negative number.

Three-dimensional (3D) analysis – This requires a powerful computer to perform the necessary rendering of serial sections of the specimen. A PC computer populated with 1 Gigabyte of RAM and a fast 3D graphics card can process datasets of up to 200 Megabytes. For larger datasets a UNIX based super computer is required such as the Silicon Graphics Onyx 3 system. The production of a serial section set and the subsequent input into the computer is extremely time consuming. The processing speed of the computer and the available random access memory (RAM) is a limiting factor in the size of specimen that can be processed. The connectivity in three-dimensions can be assessed using the Euler-Poincaré's number technique (Goldstein et al, 1993). Using micro-CT methods, as with the X-ray tomographic microscope, makes the process less time consuming and has the added advantage of being able to analyse the specimen *in vivo*. The connectivity of the trabecular bone, as measured by the Euler characteristic, has been applied to 3D reconstructed models and was shown to correlate with trabecular bone volume (Kinney et al, 1995).

Trabecular bone volume and trabecular bone pattern factor (TBPf) has been measured using 3D images produced from micro-CT (Ikeda et al, 2001).

Cortical bone mineral density has also been calculated from 3D reconstructions obtained from quantitative computed tomography (QCT) (Maki et al, 2001).

Undoubtedly, the ever-increasing resolution made possible with the development of new micro-CT machines along with the relative affordability of adequate computing power, makes the study of the 3D structure of bone an exciting future prospect. The cost of a micro-CT machine, powerful computer and the analysis software is still considerable and, at the moment, is outwith the scope of many research groups.

Confocal microscopy can also be used to electronically section a specimen using lasers of a particular wavelength, which excite immuno-labelled tissue. The microscope collects the light from the tissue and from the resultant data, can 3D reconstruct the labelled tissue (O'Brien et al, 2000). The limiting factor in using confocal microscopy is in the physical size of specimen that can be analysed.

Medullary discrimination

Delineation of the medullary area – Automation is an on-going goal for the image analyst. Any procedure which reduces or removes inter-observer and intra-observer variability is advantageous to image analysis. A technique used to analyse iliac bone biopsies has implemented a procedure which eliminates the manual division and discrimination between cortical and trabecular bone. The fully automated technique measures a binary image of the cortical bone. The width of each hole in the image is measured to give a value w. An expanded contour is generated at a point $w/2$ away from the edge of the hole. Pixels lying along the contour are examined and if more than 75% of them are occupied by bone, the hole is filled. The image is eroded and dilated to leave a clear cortico-medullary junction (Croucher et al, 1994). This technique is novel and well considered, but does not work on specimens where there is a large variation in the cortical bone thickness, as in the femoral neck.

Bone distribution

Bone distribution – The effect of an arthritic disease on bone may result in the morphology of the bone being changed. To detect changes in bone morphology, diseased specimens can be compared with disease free control specimens. To determine and quantify these changes it is necessary to measure and compare the distribution of bone and any pattern of change noted.

The study of distribution of bone within vertebra has been described by dividing the specimen into nine sectors. The sectors cannot be of identical size, as pathological changes result in lop-sided specimens (Parkinson & Fazzalari, 1994).

Bone variations through the whole human femoral head have been studied by making a coronal slice through the middle of the femoral head and dividing the head into three equal parts corresponding to the medial, central and lateral aspects of the head. By dividing the head into three parts it was possible to make histological sections from undecalcified methylmethacrylate blocks. 30 randomly chosen fields in each region/ section was measured, for trabecular bone volume. Bone density was found to have reduced in the medial region compared to the other regions. These results suggest that the remodelling of the subchondral bone (at least in the short term) is fairly constant and not related to weight bearing (Amir et al, 1992.).

Aims of this project.

Studies have shown that the use of image analysis in the measurement of morphological changes in bone is reproducible and reliable (Parkinson & Fazzalari, 1994), with operator bias less than 5%. Full automation of image analysis procedures is the ideal goal for the image analyst, but the nature of biological tissue makes this extremely difficult to achieve.

This study centres around the development of three separate image analysis macro programmes to analyse the femoral neck, femoral head and Heberden's nodes.

The largest part of the work was aimed at creating a method to quantify the distribution of trabecular and cortical bone in the human proximal femoral neck and ensuring that this method was as automated as possible.

The study aims to add to the pool of architectural and morphometric information on bone in OA. Studying the architecture of the femoral neck and head and how they respond to the disease, particularly in the weight-bearing regions, may suggest a reason why clinicians have reported that OA patients rarely suffer from fracture of the femoral neck.

Studying the architecture of the DIP joint of cadavers exhibiting Heberden's nodes, may help to understand the mechanisms that are responsible for the underlying osteophytes. The study will investigate the distribution of osteophytes around the DIP joint of fingers with Heberden's nodes.

Methods

Methods

Many excellent texts are available detailing image analysis techniques. A few examples being: “Image analysis in histology”, Wootton, Springall and Polak (1995); “The image processing handbook”, Russ (1999); “Image analysis principles and practice”, Joyce-Lobel (1985). For the non-expert, the image analysis glossary (at the end of this thesis) contains an explanation of image analysis terminology and system commands relevant to this study.

Apparatus

Burgess BK3 band saw.

Asteil & Hearson Vacuum embedder.

Reichert-Jung, Heidelberg Sledge microtome.

Soft tissue laboratory X-ray machine using a Machlett N6656 tube.

Leitz Reprovit 11A copy camera.

Kontron Elektronik VIDAS Image Analysis System, software version 2.5. The VIDAS system uses a Kontron Elektronik *frame grabber* to digitise the images. Images were acquired from a Sony XC-77CE high-resolution ½inch CCD monochromatic camera, mounted on a Repro photographic copy stand, with an illuminated stage and using a CCTV Zoom 12.5-75mm F1.6 macro lens. The system employs a Digicad Plus digitising tablet to facilitate user input. *Macros* were written on the system’s *interpreter*.

Image analysis system and operator protocols

Image analysis is a very powerful tool for the biomedical scientist to utilise in accumulating meaningful morphometric data. Bone histo-quantification is particularly suited to image analysis techniques.

Care must be taken, before an experiment begins, to investigate and analyse the sources of potential error. Tests were carried out to determine the amount of error introduced by intra- and inter-operator variability, system bias and random error. The tests investigated the effects of: re-scaling, re-focus, cortical and trabecular bone thresholding and magnification changes. The tests were based around the operation of the femoral neck macro.

Intra observer error

The amount operator error was tested at every stage of user interaction within the macro.

A black elliptical shape (33mm X 44mm) was printed on a piece of white paper, similar to the overall shape and size of a femoral neck section. This test specimen was used in some of the testing procedures.

Scaling – As the operator changes the level of zoom/ magnification, he/she is required to re-calibrate the image analyser. A standard light illumination level was set and used for each run. A scale bar measuring 30mm in both X and Y planes was placed under the camera and was used to calibrate the system for magnification via its geometric scaling function. Once the system had been calibrated the elliptical test specimen was placed under the camera and digitised. The system uses 8-bit grey-scale images, which result in 256 shades of grey from 0 (black) to 255 (white). When an image is *thresholded* (grey-scales converted to a single grey value to create a binary image, usually white on black) the user can set the limits that are applied. The image was automatically segmented to a binary image with the same threshold limits of 1 - 80 being used for each run. This binary image was measured for *AREA*. This procedure was repeated 10 times. The whole procedure was carried out again the following day and again the day after, to produce three runs of 10 measurements.

Focus – When each specimen is presented for measurement the user must focus the camera. The standard light illumination level was again used and the 30mm scale used to calibrate the system for magnification as before. This initial scale calibration was used throughout the test i.e. the scaling calibration was not re-done. The user would now focus the camera on the elliptical test image. The image was then measured for *AREA*. The user then de-focused the camera and performed the procedure again, repeating it a total of 10 times. The procedure was again carried out on the following two days, to give a total of three runs with 10 measurements in each.

Cortical bone thresholding – A non-arthritic control femoral neck specimen was placed under the camera and digitised. The standard light illumination level was again used and the 30mm scale was used to calibrate the system. The light level and the scale calibration were not altered throughout the test. The same outside mask (a binary image mask which was produced to include all bone in the section) and medullary mask (a binary image mask which was produced to include all bone in the medulla) were used throughout the test experiment. The user was asked to threshold the cortical bone. The programming VDU screen was covered so that the user could not see the digital read-out of the level of discrimination. The total area of the cortical bone was measured. A run of 10 measurements was performed. The same test was carried out the following two days, to provide a total of 30 measurements (10 per day).

Trabecular bone thresholding – A femoral neck control specimen was placed under the camera and digitised. The light level was again fixed and the 30mm scale was used to calibrate the system. The light level and the scale calibration were not altered throughout the test experiment. The same outside mask and medullary mask were also used throughout the test experiment. The user was asked to threshold the trabecular bone. The programming VDU screen was covered so that the user could not see the digital read-out of the level of discrimination. The total area of trabecular bone and count of trabecular bone profiles was measured. A run of 10 measurements was performed. The same test was carried out the following two days, to provide a total of 30 measurements (10 per day).

Inter observer error

The amount of error between operators was tested. Three operators were used: one expert/ experienced operator – MN and two non-expert operators – RK and EP.

Trabecular bone thresholding was deemed to be the most difficult and skilful operation to carry out, owing to the small size of the objects to be thresholded. The non-experts were given instructions on the method and allowed a few runs to familiarise themselves with the procedure. A femoral neck control specimen was placed under the camera and digitised. The light level was again fixed and the 30mm scale used to calibrate the system. The light level and the scale calibration were not altered throughout the test experiment. The same outside mask and medullary mask were also used throughout the test experiment. The user was asked to threshold the trabecular bone. The programming VDU screen was covered so that the user could not see the digital read-out of the level of thresholding. The total area of trabecular bone and count of trabecular bone profiles was measured. A run of 10 measurements was performed. The same test was carried out the following day, to provide a total of 20 measurements (10 per day) per operator.

Magnification effects

Digital images suffer from a fractal effect where the measured perimeter will decrease relatively with an increase in the measured step-size i.e. if the coastline of Britain was measured with a 1cm ruler and again with a 1m ruler, the total measure obtained with the smaller ruler will be larger than that of the larger ruler. Although perimeter was not measured in this experiment some image analysis systems use a method of pixel counting to calculate area. This method of measuring area is susceptible, although not as severely as perimeter measurement, to this fractal phenomenon, as reported by Weibel (1979). Whether the range of magnifications used in this experiment would produce a significant error was determined.

The elliptical test sheet was placed under the copy stand and *grabbed* into the image analyser at three different zoom levels, which replicated the possible zoom/ magnification levels which may be used in the experiment. The test was carried out at: low magnification, medium magnification and high magnification. For each run the image analysis system was calibrated in both X and Y planes using the 30mm scale. The light level and thresholding limits were again fixed. The image was then measured for *AREA*. The image analyser measured the object 10 times. The zoom would then be altered to the next magnification (high, medium and low).

Collection and processing of hip material

The material was collected from patients undergoing hip replacement surgery during 1993. Verbal consent was given for the use of their tissue in this research project.

- Five females with osteoarthritis [OA] (aged 61, 63, 67, 74 & 76 years).
- Control groups – Five females (64, 68, 75, 79 & 85 years). Control specimens were obtained from dissecting room subjects. The specimens were ones with little evidence of arthritis on dissection. The controls had no known arthritic history.

The gross appearance of the specimens was recorded by photographing them with the copy camera (Figure 1 & Figure 2). They were then fixed by immersing in Karnovsky's fixative (3% formaldehyde + 1% glutaraldehyde in 0.1M phosphate buffer). The tissue was left in this solution for at least two - three weeks.

Division of Specimens

Each specimen was divided into head and neck areas by sawing with the band saw. A 5mm slice was taken from the uppermost part of the femoral neck proximal to the head. The femoral head was then halved in a coronal plane (Figure 3), achieved by careful reference to the gross photographs. A 5mm slice was obtained, from the posterior half, by sawing parallel to the first saw cut (Figure 4).

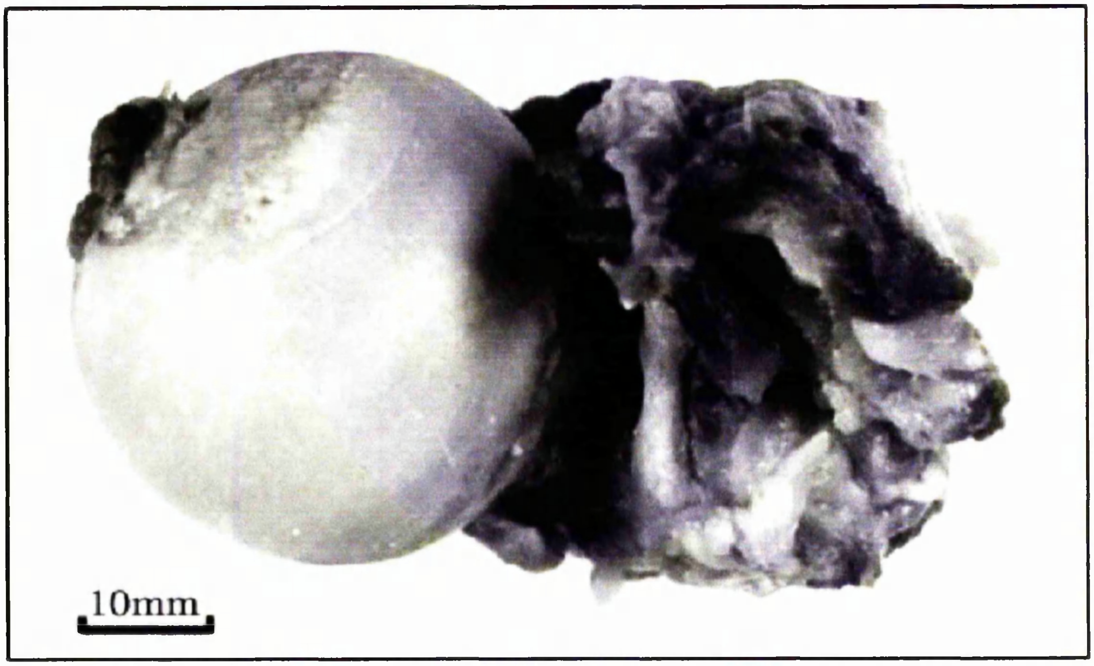

Figure 1. Normal human femoral head.

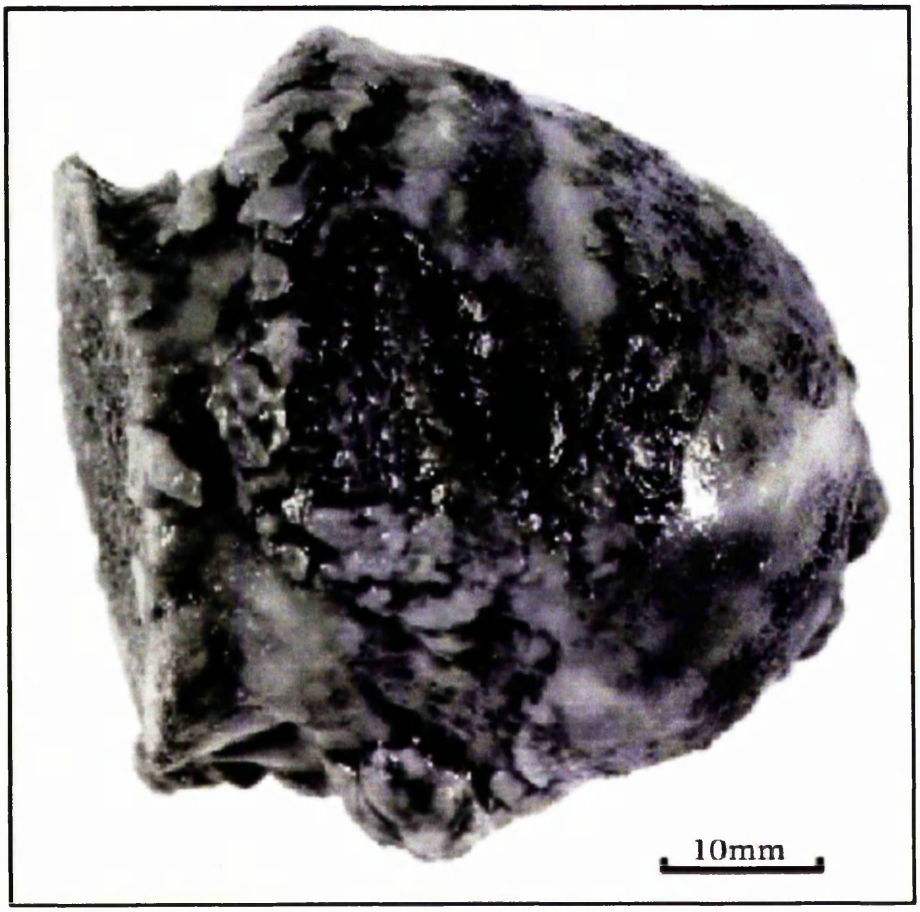

Figure 2. Osteoarthritic femoral head.

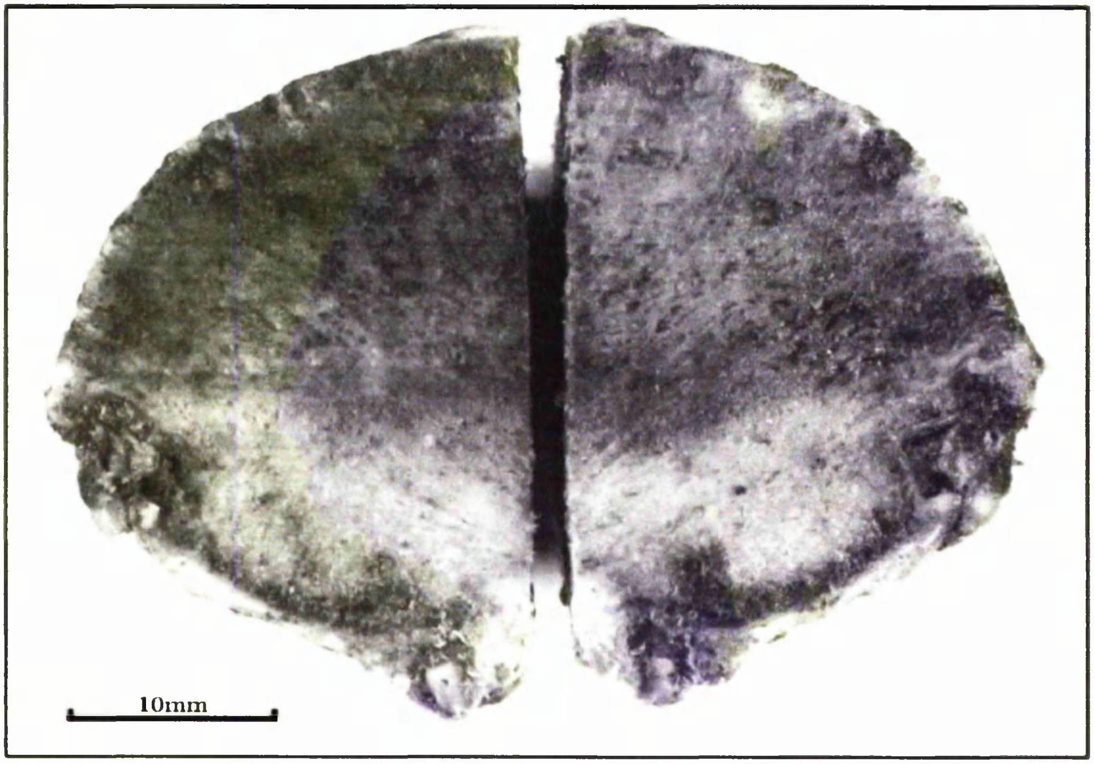

Figure 3. Coronal cut through the femoral head.

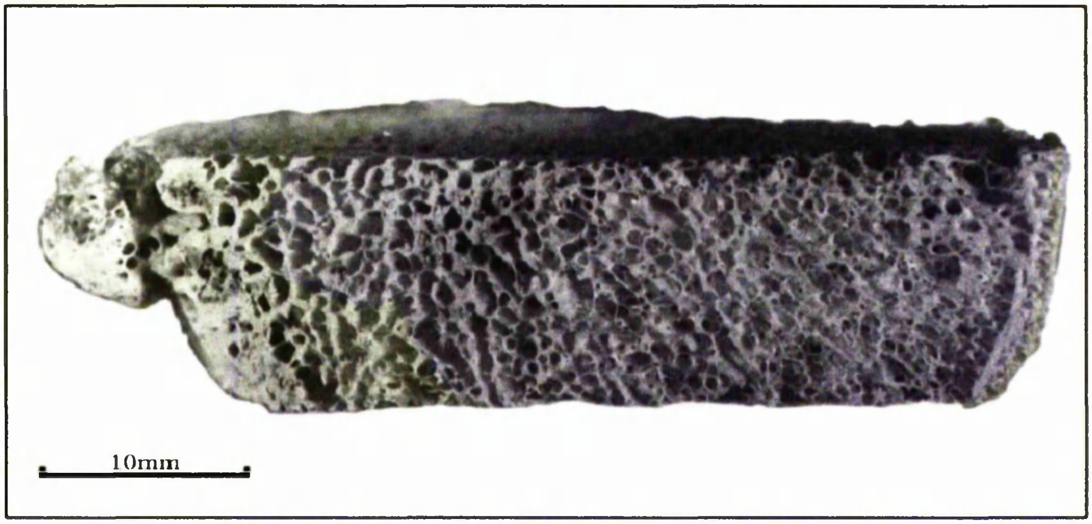

Figure 4. Slice through femoral head.

Processing of the femoral head

The slices of the femoral head were placed in a solution of 5% sodium hypochlorite for 24 hours to remove all soft tissue. The slices were washed by immersing in 0.1M phosphate buffer for four hours, the solution being changed three times. The specimens were then dehydrated through 50% acetone and three changes of 100% acetone.

The slices were air dried in a desiccator.

N.B. The traditional method of drying specimens with the Critical Point Drier was discounted as it was felt that as the bone dried and the soft tissue removed that the mechanical turbulence produced could cause some of the fragile trabecular bone to break.

Processing of the femoral neck

The histological techniques employed were modifications of well-known methods.

Decalcification - Decalcification was achieved by immersing the specimen in a solution of 10% ethylenediaminotetra-acetic acid. (EDTA) in 0.1M Phosphate buffer. The specimens were left for a minimum of three months and not more than six months. The solution was changed every week, probing with a pin tested the extent of decalcification. This gave a measure of how pliable the tissue was. If the pin penetrated easily through the tissue, the decalcification was complete. This requires considerable experience to judge accurately. N.B. Rapid decalcifiers were discounted for use, as they would have been too disruptive to the tissues.

Prior to wax processing, the specimens were stored in 0.1M phosphate buffer for two days, the solution being changed each day.

Wax embedding - The tissue was too large and dense for automated processing using the histokinette, therefore, it was necessary to process by hand.

Dehydration – The specimens were immersed in methanol for one day; ethanol for three days, with the solution changed each day; and amyl acetate for three days, with the solution changed each day.

Wax impregnation - Wax impregnation was achieved using a mixture of one part bees wax to eight parts Paraplast wax. Penetration of wax and removal of air was aided by the use of the vacuum embedder. The specimen was vacuumed for two hours, with the wax changed after one hour. The specimen was then embedded in a deep container and orientated to allow the sectioning to come into full face, on the face closest to the femoral head.

Sectioning - Sections were cut on the sledge microtome at a thickness of 12μm. The sections were collected and then stretched in a water bath at 45°C for 3 seconds. A higher temperature and shorter time than that normally used was employed to try to minimize the over-stretching of these large sections i.e. using a lower temperature over a longer time resulted in some parts of the section stretching more than others. This procedure was rigidly followed, to reduce experimental bias (Parkinson & Fazzalari, (1994). The sections were collected onto slides coated with chrome alum gelatin, the chrome alum helping the sections stick to the slide. Sections were stored for at least one-week in a 37°C oven.

Staining - Various stains were tried and tested in order to attain the best possible discrimination between the bone and the other tissue components. Initially toluidine blue, pyronin, methyl green pyronin, Masson, modified Masson (Ponceau fuchsin), van Gieson and a modified van Gieson were tried.

The stain eventually chosen was the modified van Gieson (Appendix D). Normal van Gieson (van Gieson, 1889) staining will stain bone red while the marrow will be stained with both the haematoxylin (nuclear stain) and picric acid (counter stain). The haematoxylin was omitted. The picric acid was reduced by washing, leaving only the bone stained (Figure 5 & Figure 6). The slides were then mounted using Histomount and a cover slip.

Image Analysis of the Femoral Head

The aim of the analysis of the femoral head was to measure the intertrabecular spaces within a defined *region of interest* (ROI). The ROI was further divided into four equal zones to determine whether morphological changes were evident within these zones, compared to each other, and particularly, to any change above or below the epiphyseal line.

To measure the intertrabecular spaces, the dried coronal slices were photographed. From these photographs, the ROI was determined by measuring the cut face and plotting the mid point. 10% of the total cut face distance was measured either side of this mid point. Radiating lines were drawn from these points parallel to the general direction of the bony trabeculae (Figure 7). Tracings were made by drawing round the perimeter of the bony margins of the trabeculae. The tracing was then divided into the four zones (Figure 8) by measuring the length of each side of the ROI and dividing them into the four equal parts and then joining the two corresponding points from each side. Spaces, which transversed a boundary, were allocated to the zone on which their greater part lay (Figure 9). Each tracing was then analysed with the VIDAS Image Analysis System with the aid of a purpose-written macro (Appendix A). The binary image of the ROI is shown in figure 10. The macro (Figure 11) was written, using the VIDAS proprietary language, within the system's *interpreter*.

Variables and measurement parameters - Firstly, the *macro* would define the measurements: *AREA, FERETX, FERETY* (Feret, 1931), *DMAX, DMIN,* and a form factor, *FCIRCLE,* for circularity (See glossary). Each of the above measurements were object based measurements on each

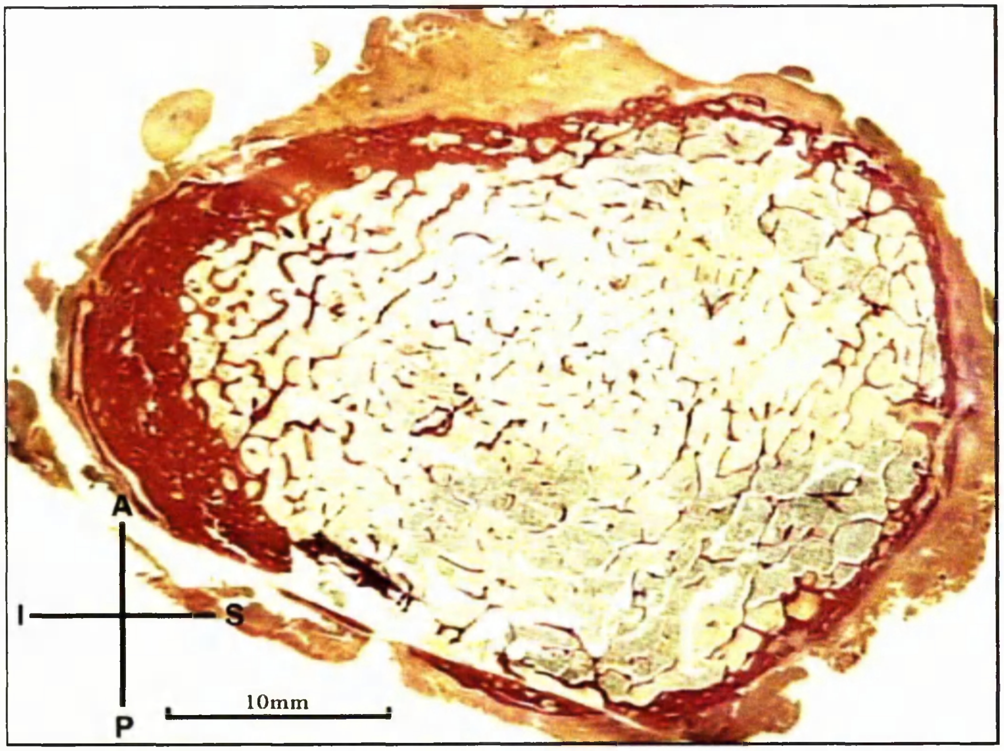

Figure 5. Normal van Gieson stain. Marrow stained with haematoxylin (nuclear stain). The picric acid gives a deep yellow counter stain.

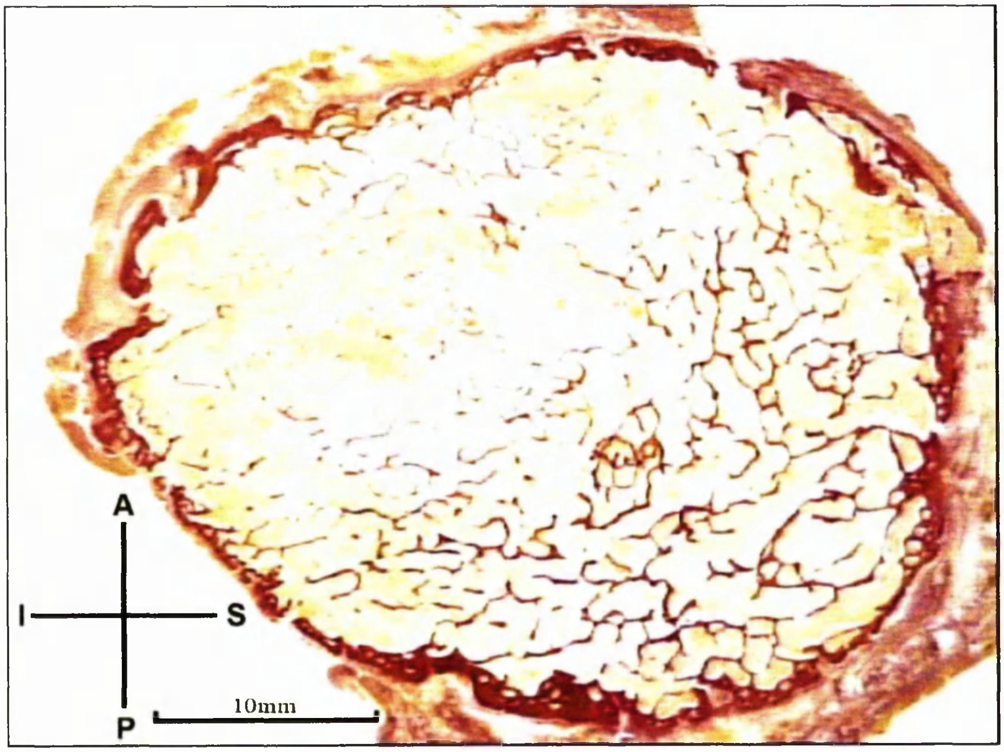

Figure 6. Modified van Gieson stain. No nuclear staining. The picric acid counter stain is much lighter.

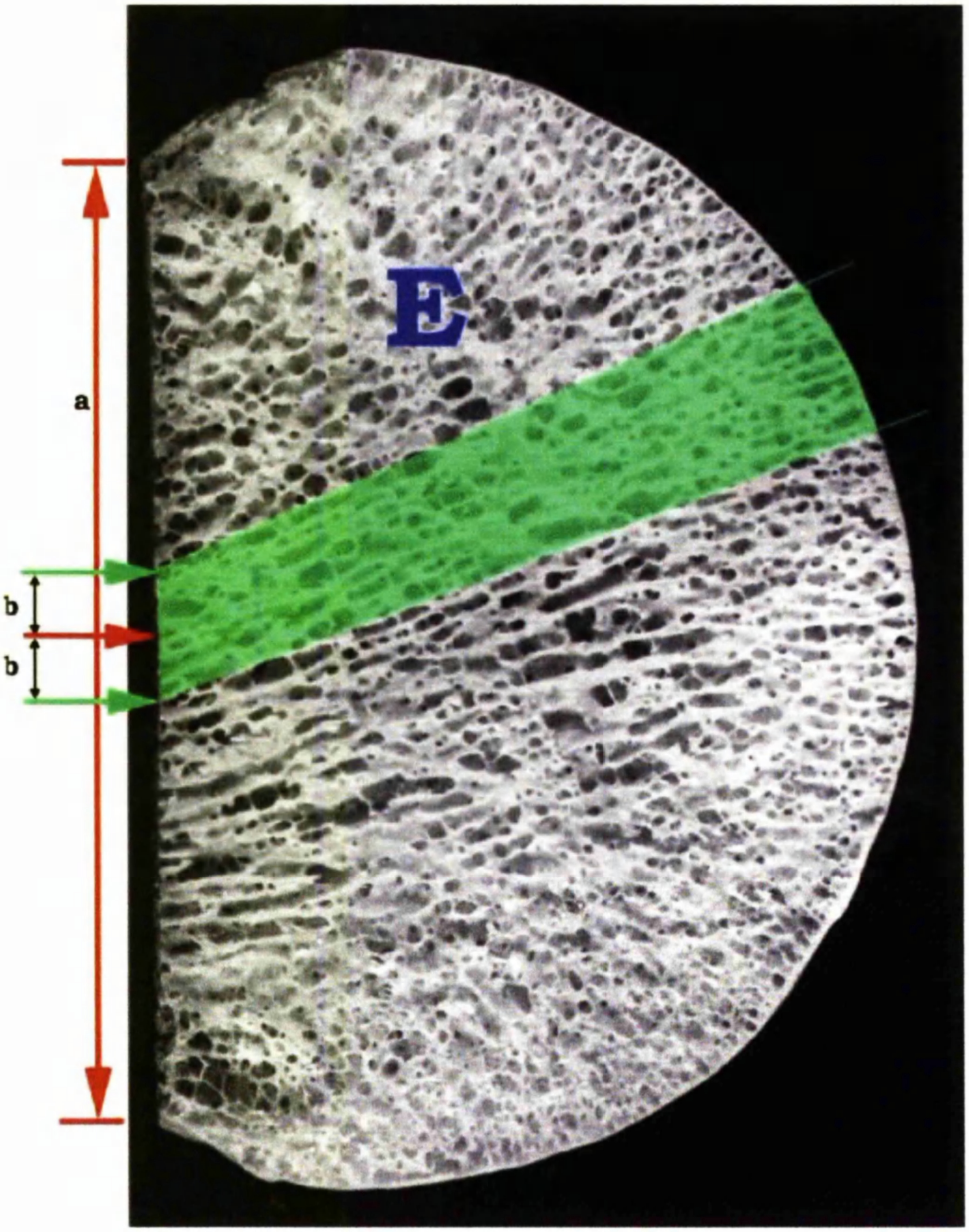

Figure 7. Femoral head slice. Control specimen. The shaded green area was the region of interest. E - Epiphyseal scar. The distance *b* = 10% of the cut face distance *a*.

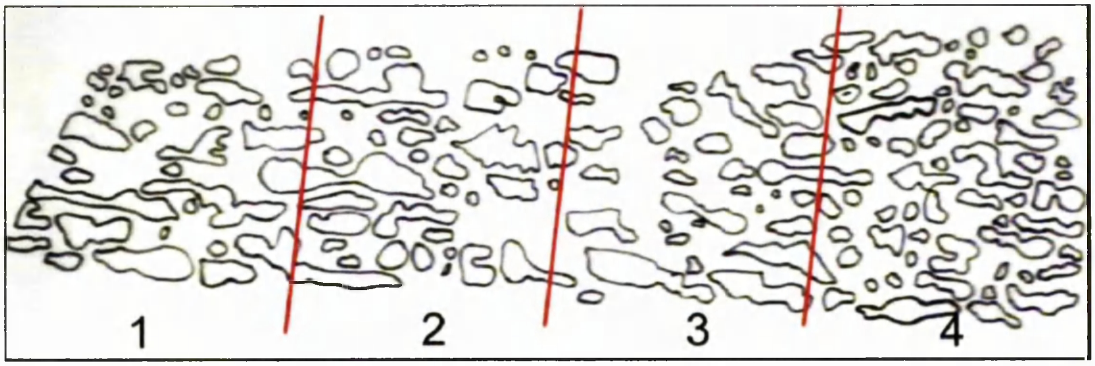

Figure 8. Tracing of intertrabecular spaces in the femoral head. The region was divided into four equal parts.

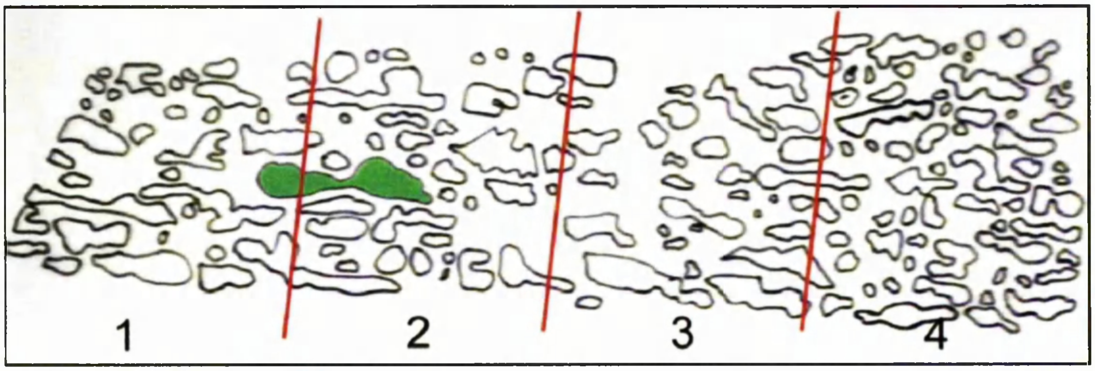

Figure 9. Intertrabecular space lying in two segments. Objects which lay across to segments, were counted in the area in which the largest proportion lay.

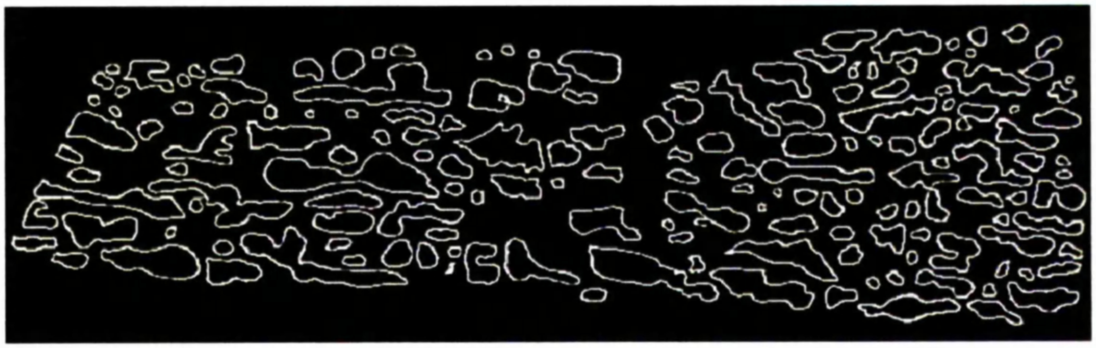

Figure 10. Binary image of the intertrabecular spaces.

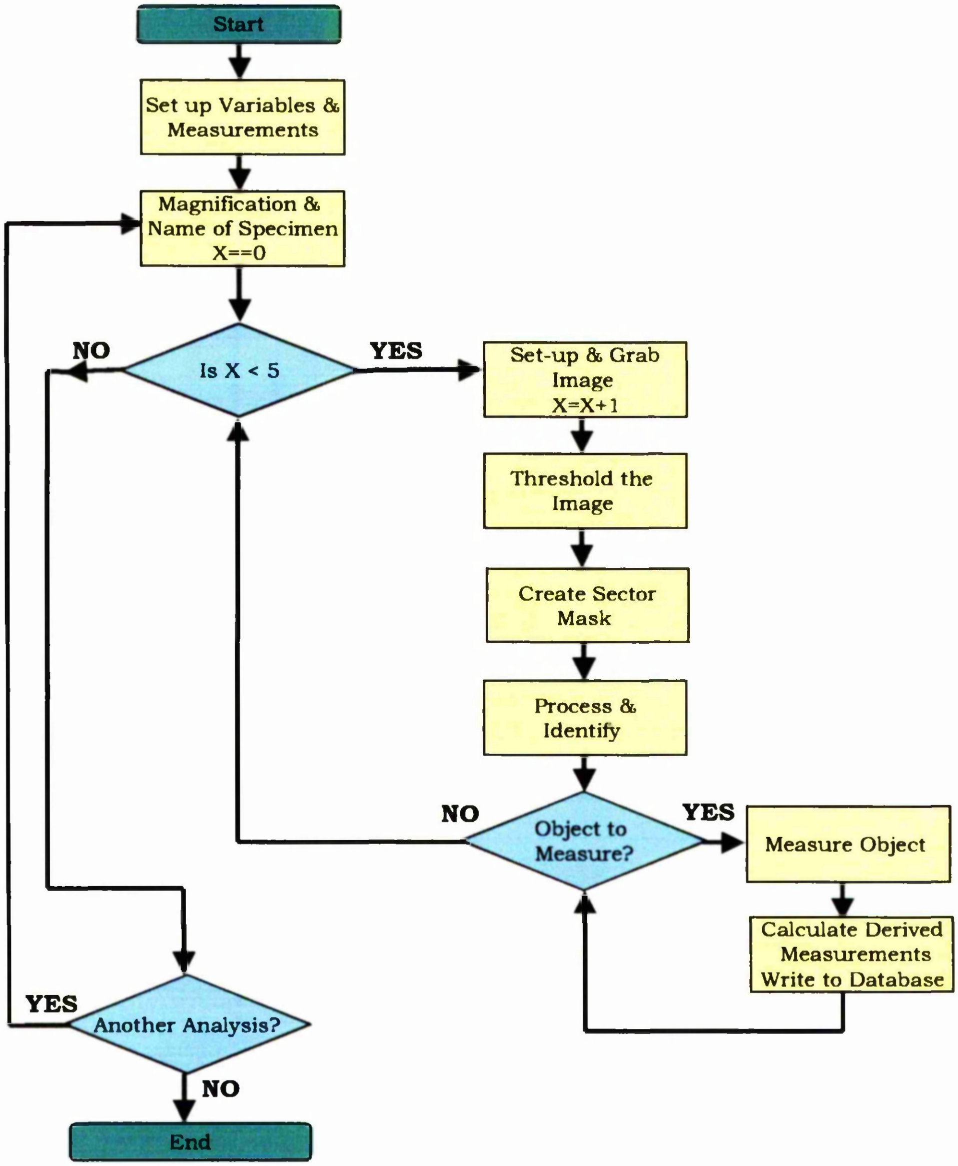

Figure 11. Flow chart of image analysis macro – Femoral Head (Appendix B).

trabecular space. The measurement and derived measurements and associated variables were defined as:

Trabecular Space Area	*trabarea*
FeretX of Trabecular Area	*ferx*
FeretY of Trabecular Area	*fery*
Form Factor Trabecular Area	*FCIRCLE*
Maximum Diameter of Trabecular Area	*DMAX*
Minimum Diameter of Trabecular Area	*DMIN*
Mean Area of Trabecular Space Area	*avetrab*

N.B. At the time of writing the macro it was undecided which measurements would eventually be used. As the VIDAS system can measure many parameters simultaneously (with no extra CPU overhead) it was decided to include all of the above measurements. Only the 'Trabecular Space Area' was used to analyse the specimens. All other data was stored and may be used in future analysis.

Resolution - To get the maximum possible resolution, the image size was set to 768 x 512 pixels (the largest available on the system).

Scaling - After all macro measurements, parameters and variables were set, the user would be prompted to frame the tracing and then place a scale bar on the copy stand. Although the scale of each tracing was slightly different (due to the photography), the specimens were digitised using exactly the same zoom on the camera lens and same distance setting on the macro stand. The scale bar would then be *digitised*, measured and stored. To correct for the slightly different magnifications of the tracings, the macro would ask for the magnification factor *'mag'* of the photograph. This variable *'mag'* and the derived variable, *'magt'* (mag^2) for areas, would be used later in the macro to calculate the actual measurements.

Main loop - After entering the name of the specimen, *'specim'*, the main *'while–endwhile loop'* (a computer scripting tool which repeats a section of code until a condition is met) would start. This loop would stop after four cycles. This enabled the macro to measure the four sectors and create a separate database for each. The automatic database file creation was achieved by incrementing the variable *'spec'*, by adding the *string* value of the loop counting variable *'x'* to the specimen name variable *'specim'*.

Image capture - The tracings were placed on the illuminated stage and the images captured and digitised via camera and frame grabber into the image analysis computer.

Segmentation of the intertrabecular spaces - After an automatic contrast adjustment, the image was automatically segmented, using a "*two thresholding levels*" technique to create a binary image (Figure 10). The structures in the zone of interest would then be determined (Figure 12). To eliminate any 'background noise' from the image, the *scrap* command was used. This would eliminate any objects with an area of

Figure 12. Binary image of zone 1.

Figure 13. Binary filled image of zone 1.

Figure 14. Binary eroded image of zone 1.

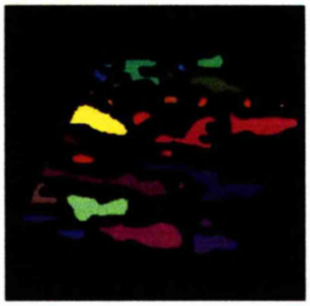

Figure 15. Identified eroded image of zone 1.

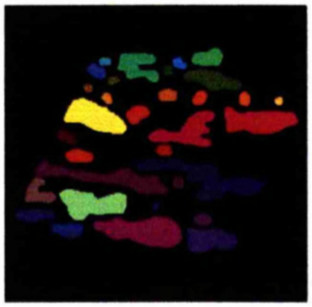

Figure 16. Identified restored image of zone 1.

less than 22 pixels. The limit of 22 was determined as 'safe' by a previous test. Next, the system would *fill* the objects (Figure 13). To separate any touching objects, the macro would *erode* them (Figure 14), until none were touching and then use the *identify* command to give each object its own identity (Figure 15). The system does this by assigning each structure a different greylevel (0-255). As the eye cannot determine the difference between a greylevel and the next, it is necessary to view the identification by applying the *Look-Up Table* (LUT) *ident,* which assigns a different colour to each greylevel. Now that each individual object has been identified, it is possible to 're-grow' the objects back to their original size by applying the *erode* command again, this time working on greylevel 0 (the background). If the background is eroded, then everything else will dilate (Figure 16). Exactly the same parameters were used in each erode command, to ensure the same amount of eroding was done each time i.e. *Shape=7, Count=2.* Measurement variables were reset before measuring was started.

Measurement of intertrabecular spaces - To measure the parameters defined on pages 39/ 44, another *'while - endwhile loop'* was used with the function *Measo*. The function *Measo* is a very powerful tool which allows the sequential measurement of objects in an *identified* image. As the loop repeats, the image processor is left in a state that "remembers" which was the last object measured, so that on the next call, it will immediately proceed to the next object. On each cycle of the loop, the system performed the measurement functions defined on pages 39/ 44.

Output - Each of the other three zones were then measured in turn and input into a database, before a print out of the data was performed. The user then measured another specimen or stopped the macro.

Image analysis of the femoral neck

The transverse sections of the femoral neck were processed on the VIDAS system. The aim was to measure a variety of morphometric parameters, including a measure of bone connectivity and to analyse the distribution of cortical and medullary bone. To facilitate this, a macro (Figure 17), (Appendix B), was developed and run on a VIDAS system. An important goal, for the macro, was that it be as automated as possible.

Resolution - To achieve the maximum possible resolution, the image size was set to 768 x 512 pixels. The morphology of the femoral neck section suited this image size. The VIDAS frame store (image memory) can support six images of this image format in the memory at any one time. To help explain the mechanics of the macro, it would be beneficial to list the image occupancy of these six frame stores. When no further use is required for an image, the frame store can be over-written.

Frame stores used for the processing of the bone and the creation of the medullary and section masks:

Image Frame Store 1	Binary image of medullary area.

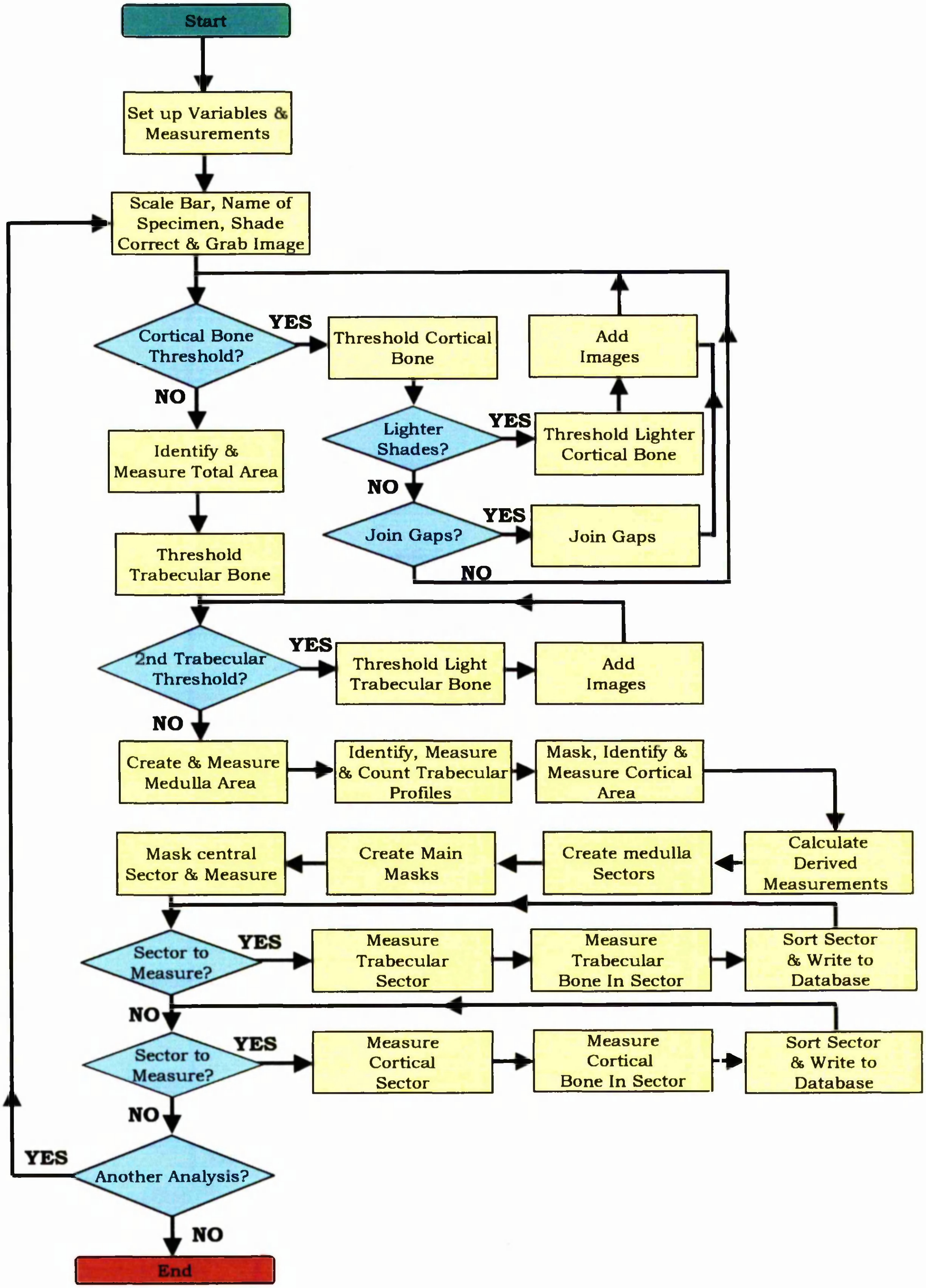

Figure 17. Flow chart of image analysis macro - Femoral neck (Appendix B).

Image Frame Store 2	Grey-scale of the specimen.
Image Frame Store 3	Binary image of cortical bone.
Image Frame Store 4	Binary image of joined cortical bone gaps (used to create the medulla mask).
Image Frame Store 5	Binary image of trabecular bone.
Image Frame Store 6	Binary image of section area.

By the time the creation of the sector masks was required by the macro, no further use for Image Frame 2 & 6 was needed. They were replaced with:

Image Frame Store 2	Identified main masks.
Image Frame Store 6	Identified trabecular sectors.

Variables and measurement parameters - The measurements made by the system were: *AREA, CGRAVX, CGRAVY, FIELDCOUNT* & *TOTALAREA*. Variables were defined to allow derived measurements to be calculated. The measurement and derived measurements and associated variables were defined as:

Total area of cortical bone	$Cortical$
Total area of trabecular bone	$Trabecular$
Total section area	$TotalSect$
Ratio of cortical bone : trabecular bone	$Ratio = \frac{Cortical}{Trabecular}$
Total bone in section	$TotalBone = Cortical + Trabecular$
Area of medulla	$MedArea$
% Bone in total section	$Perc = \frac{Cortical + Trabecular}{TotalSect} 100$

% Trabecular bone in section	$PTrb = \frac{Trabecular}{TotalSect}100$
% Cortical bone in section	$PCort = \frac{Cortical}{TotalSect}100$
% Trabecular bone in medulla	$PTrm = \frac{Trabecular}{MedArea}100$
Number of trabecular profiles	$NoProf$
Medulla sector area	$Sectarea$
Total area of bone in sector	$Sarea$
$\frac{\text{Trabecular bone area in sector}}{\text{Area of medulla sector}}$	$SA\sec tA = \frac{Sarea}{Sectarea}$
$\frac{\text{Trabecular bone area in sector/ Area of medulla sector}}{\text{Medulla area}}$	$SAMA = \frac{SA\sec tA}{MedArea}$
$\frac{\text{Cortical bone in sector}}{\text{Total section area}}$	$SATS = \frac{Sarea}{TotalSect}$

Scaling – The main *'while-endwhile loop'* would start. The user would input the name of the specimen and then proceed to calibrate the system by inputting the scale. To eliminate any lens and monitor differences in the X and Y planes, the scaling operation was done in both X and Y planes. Once the scaling had been performed, the camera distance and focus could not be changed.

Light level - In an attempt to improve automation, the light level was identical for each run. This was achieved by loading a stored blank reference image (Figure 18). When viewed with a specially constructed LUT, the shaded periphery looked red (the centre being black). The

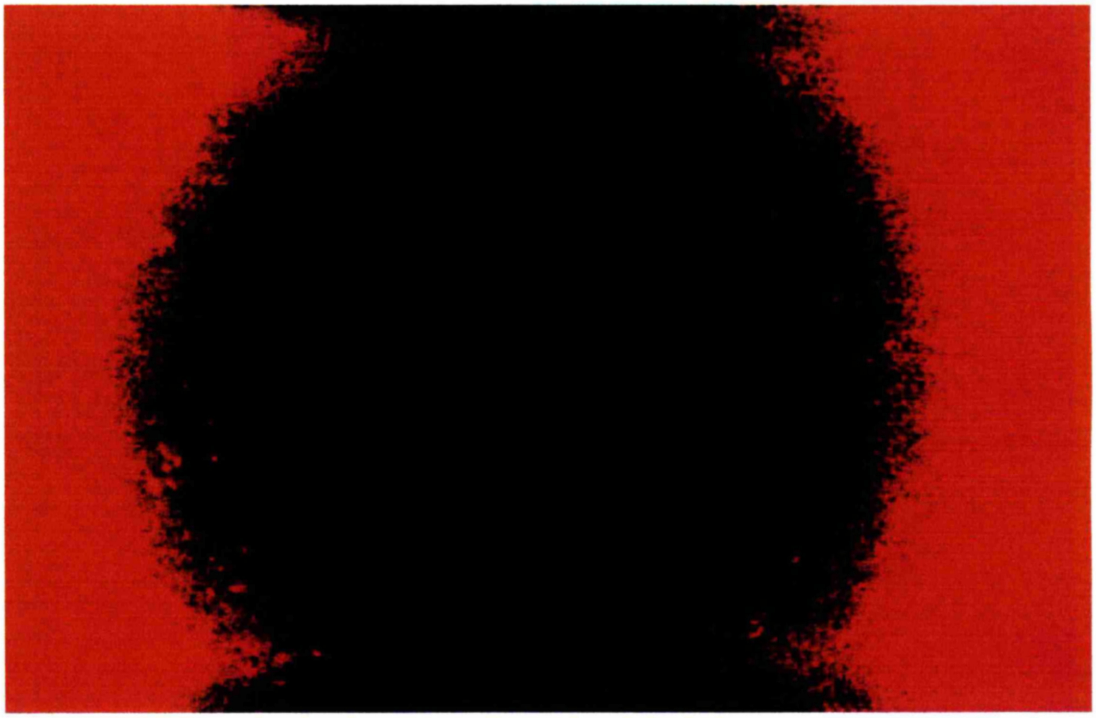

Figure 18. Reference light level image.

VIDAS command *tvalign* was used to view the live image superimposed over the reference image. As the light was increased or decreased, the user was able to adjust the live image's 'corona' to match the stored reference image.

Orientation - Each histological section was placed on the illuminated stage. To study the distribution of bone, it was very important to have each slide orientated the same way. The orientation of the slide was determined by close examination of the anatomy of the section. The slide was positioned with the extreme anterior and inferior sides of the femoral neck to be at 0° (top of the image) and 270° (left of the image) respectively (Figure 6).

Shading - To reduce periphery shading, a shade correction procedure was carried out. This was achieved by subtracting a grabbed blank image from the actual specimen image. After the specimen was grabbed into the frame store (Figure 19), an automatic contrast adjustment was made.

Segmentation of cortical bone – The inconsistency of the staining in the de-calcified specimens necessitated manual thresholding. The *'two level threshold'* method was used. If the slide's staining was particularly patchy the segmentation was done in two stages. The user would first threshold the lighter parts of the image and then the darker parts. The

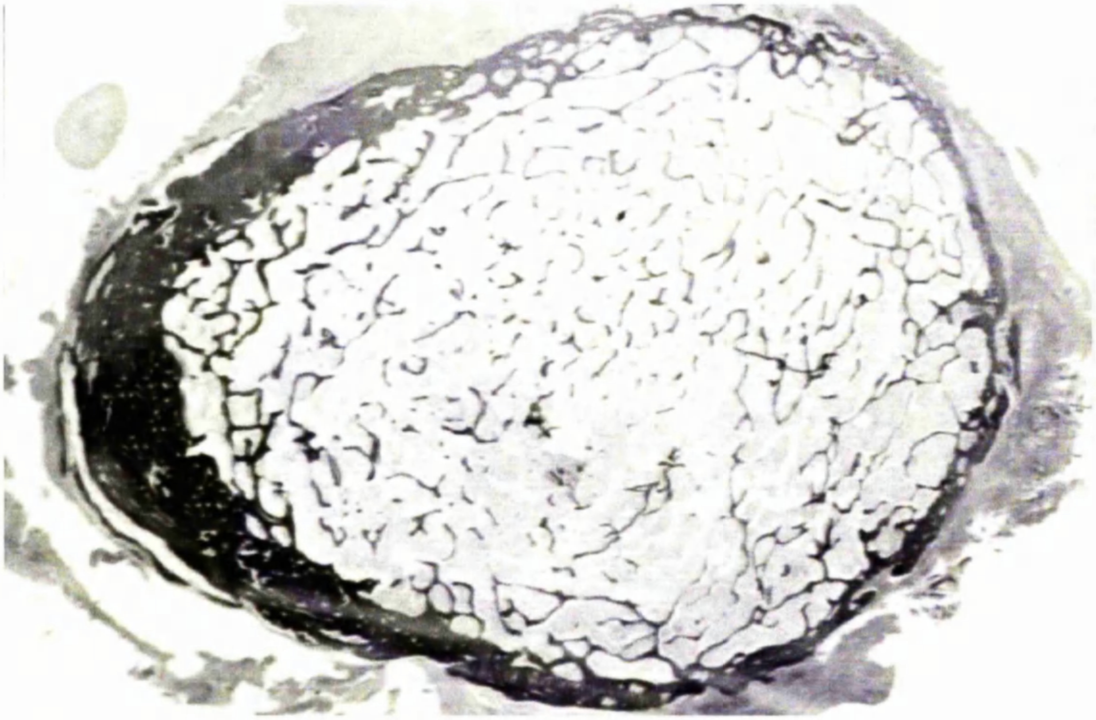

Figure 19. Greyscale image of digitised femoral neck.

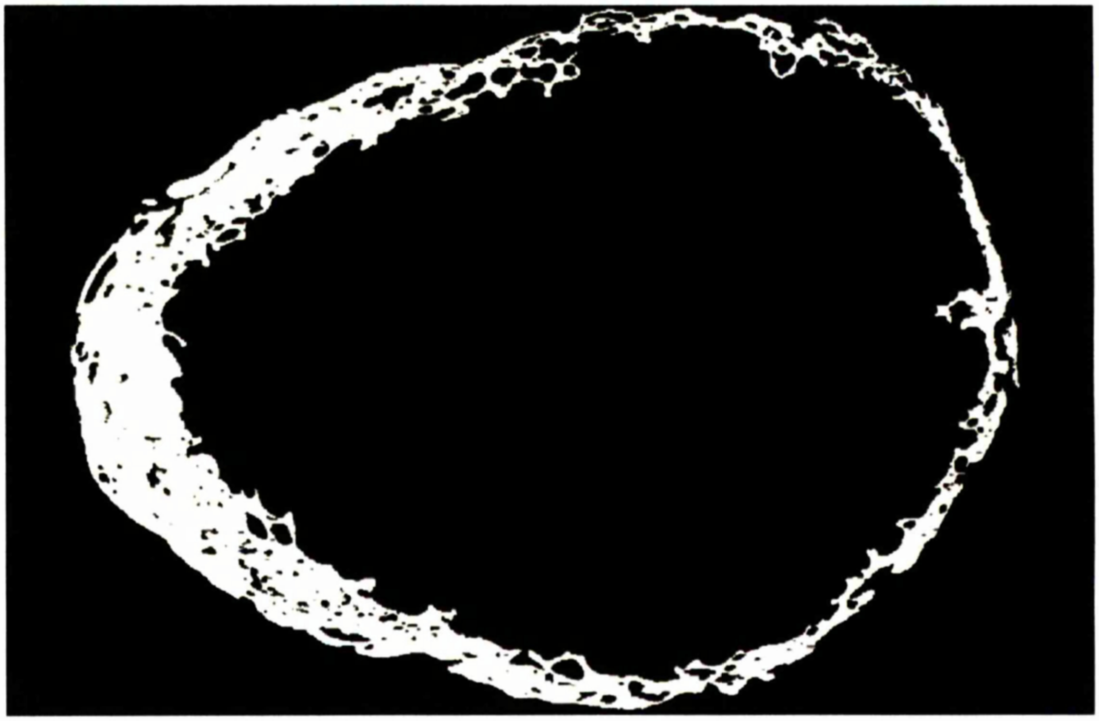

Figure 20. Segmented binary image of cortical bone.

over segmented part of the image was then discarded and the two images arithmetically added together. System *scrap* functions were used to eliminate noise and artefact material. This image was stored in Image Store 3 (Figure 20).

Creation of the section mask – The segmented cortical bone image was then dilated, filled and eroded. The same parameters, were applied in the dilation/ erosion operations. In some specimens, it was necessary to manually connect gaps in the outside of the cortical bone, to produce a continuous outside boundary. This was necessary for the efficient production of the 'outside mask' and the 'medulla mask'. The connecting lines drawn were not included in the measurements. A *scrap* operation removed all artefacts from the outside of the cortical bone. This resulted in the section mask and was stored in Image Store 6 (Figure 21). This mask was measured which gave the Total Section Area.

N.B. A method to automatically connect gaps in the cortical bone, using a binary thinning technique, was tried and proved effective, but the VIDAS system took almost 15 minutes to complete the processing. It was much quicker to manually connect the gaps.

Trabecular bone segmentation – Again, because of the inconsistency in staining, the segmentation of the trabecular bone could, if necessary, also be done in stages. The thresholding method used was *disdyn*, which is a dynamic method that computes a single adaptive threshold.

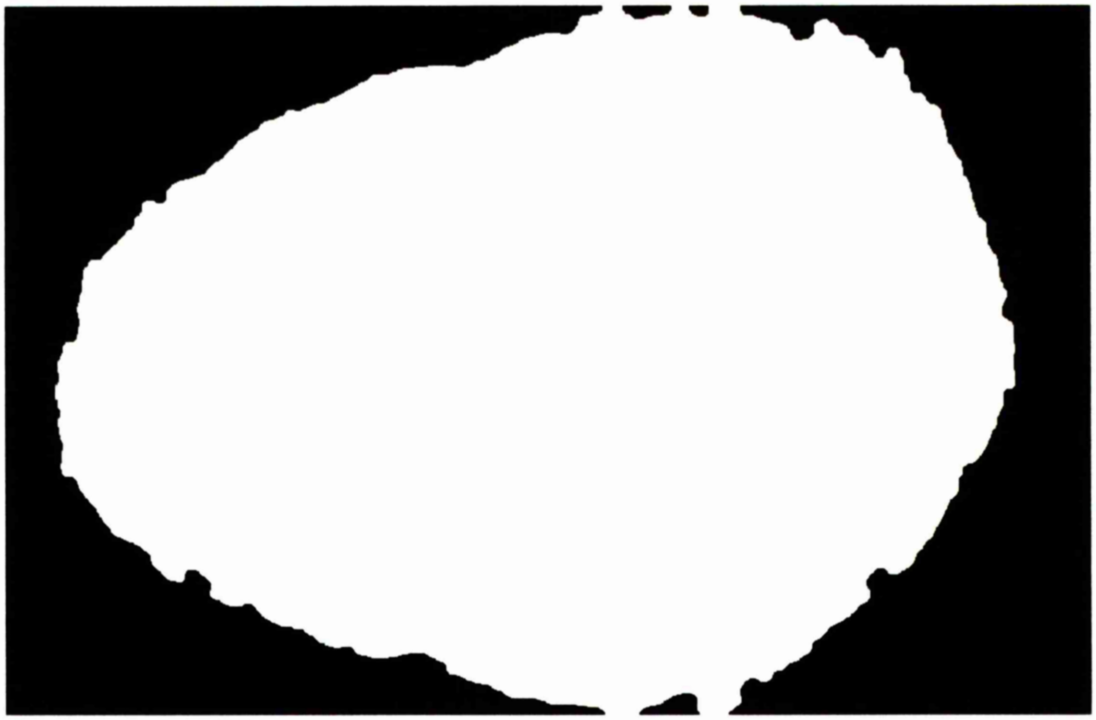

Figure 21. Segmented binary image of femoral neck. Main section mask.

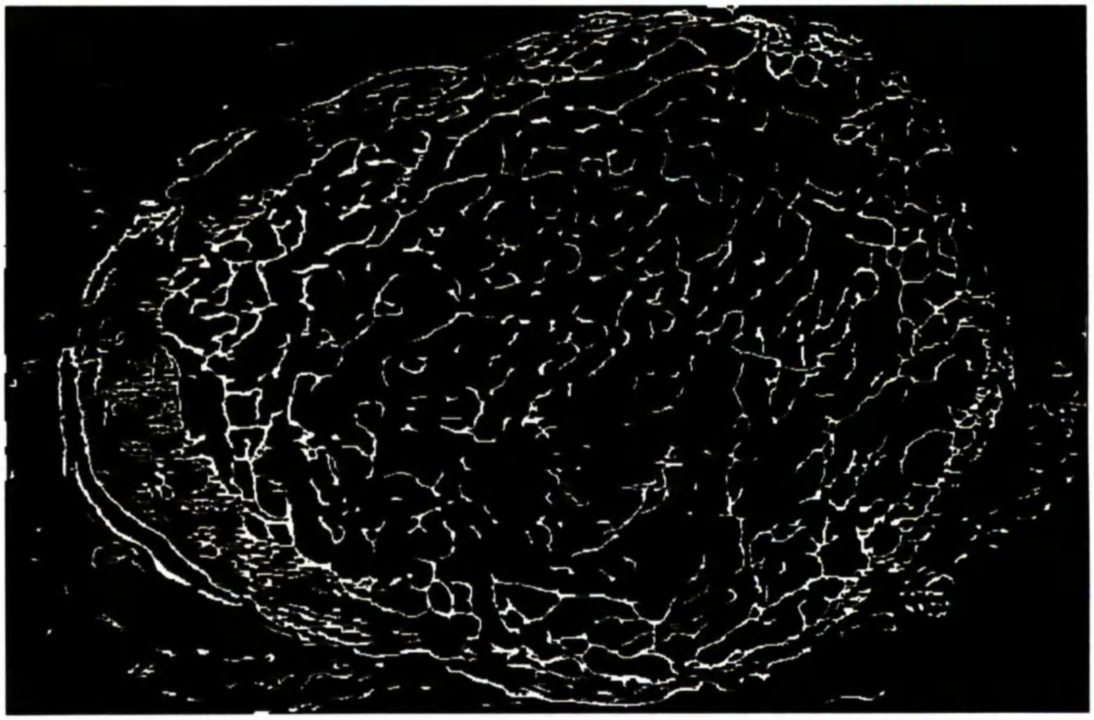

Figure 22. Segmented binary image of trabecular bone (un-processed).

This type of thresholding is particularly good at discriminating small objects on a varying background. This is achieved by applying a *low pass filter*. The matrix size of the filter was set to 5 x 5. First the operator is asked to threshold the dark areas and then, if required, to segment the lighter areas. The areas of the lighter segmentation are retained and arithmetically added to the darker segmented image. A small *scraping* operation was applied to remove noise (Figure 22). This image was stored in Image Store 5.

Determination of medullary area and isolating the trabecular bone – To avoid the operator deciding where the cortico-medullary boundary lay, an automated procedure was developed. The binary image of the connected cortical bone (Image Store 4) was further processed. To close any gaps in the cortical bone, a *close operation* was performed. A *scrap* operation and then the Boolean operator XOR (Exclusive OR) were used to correlate this image with the section mask image (Image Store 6). This procedure inverted and retained the background medulla area of image 6. It was then possible to further process using *scrap, dilate, fill* and *erode* to produce an accurate representation of the medullary area. This procedure produced a mask that cut any bone profile, protruding from the cortex. The centre of gravity of this object was measured and stored in the variables *cx* and *cy*. This image was stored in Image Store 1 (Figure 23). This image was then used to mask image 5 (Binary of trabecular bone) to produce the final trabecular bone segmented image. This image was then *identified* (Figure 24).

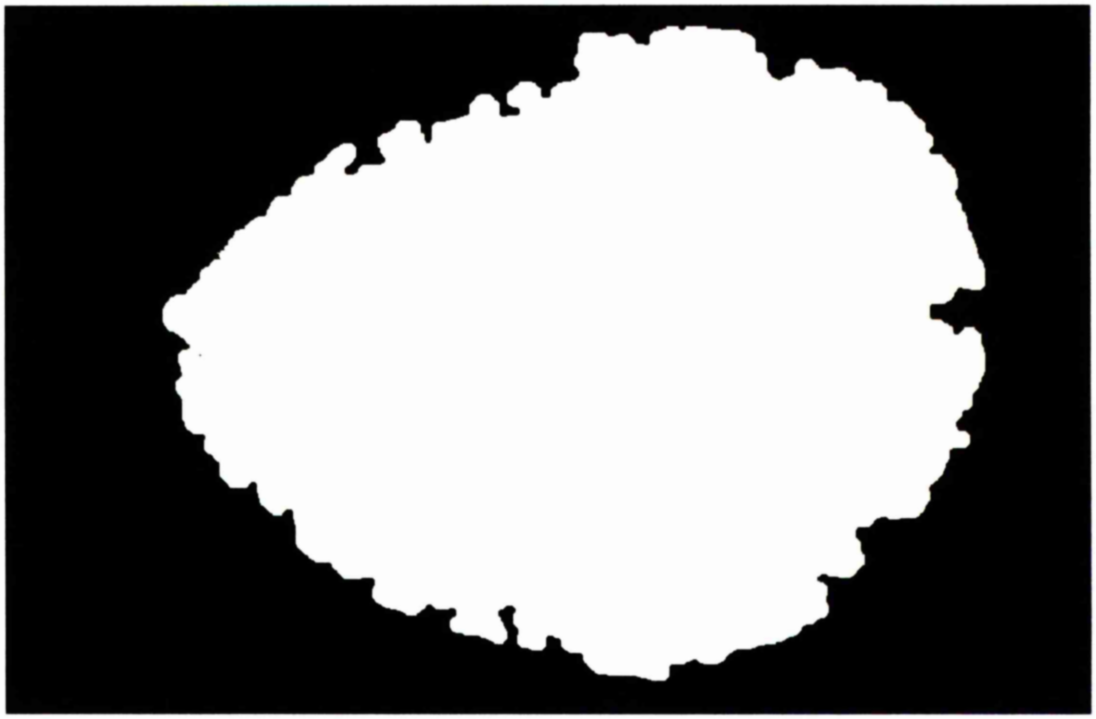

Figure 23. Binary image femoral neck. Medulla mask.

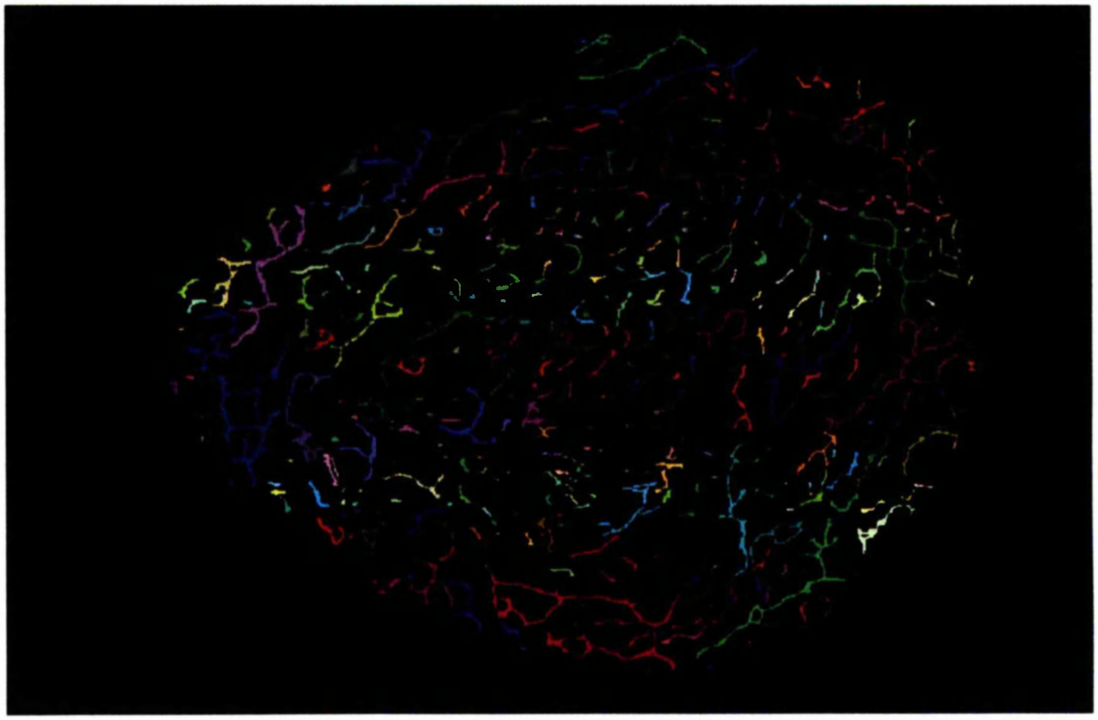

Figure 24. Identified and separated trabecular bone of the femoral neck.

Measurement of the total medullary bone - Each individual object that was not connected (using the *ident* 8-connectivity protocol) to another was considered to be one trabecular profile. The image was measured and the number of trabecular profiles (*NoProf*) and total trabecular area (*Trabecular*) were determined.

Measurement of total cortical bone – The image in Frame Store 3 was masked with the medulla mask and the total section mask to produce the final cortical bone image. The image was identified (Figure 25) and the Total Cortical Area (*Cortical*) was measured. Derived measurements: *Perc, Ratio, TotalBone, PTrb, Pcort & PTrm* were calculated.

Creation of the medulla sectors – To measure the distribution of the trabecular bone, the medulla was divided into 25 sectors. Plotted from the previously measured centre of gravity, the *'for-endfor'* loop drew radiating vectors, in the image plane, at 30° intervals.

The end points of the vectors (a, b) were calculated:

$$a = cx + \operatorname{int}\left(550 * \cos\left(\frac{step}{\_DEG}\right)\right)$$

$$b = cy + \operatorname{int}\left(550 * \sin\left(\frac{step}{\_DEG}\right)\right)$$

where: *step* is incremented by 30 on the execution of each loop.

The system variable *_DEG* = $\frac{180}{\pi}$

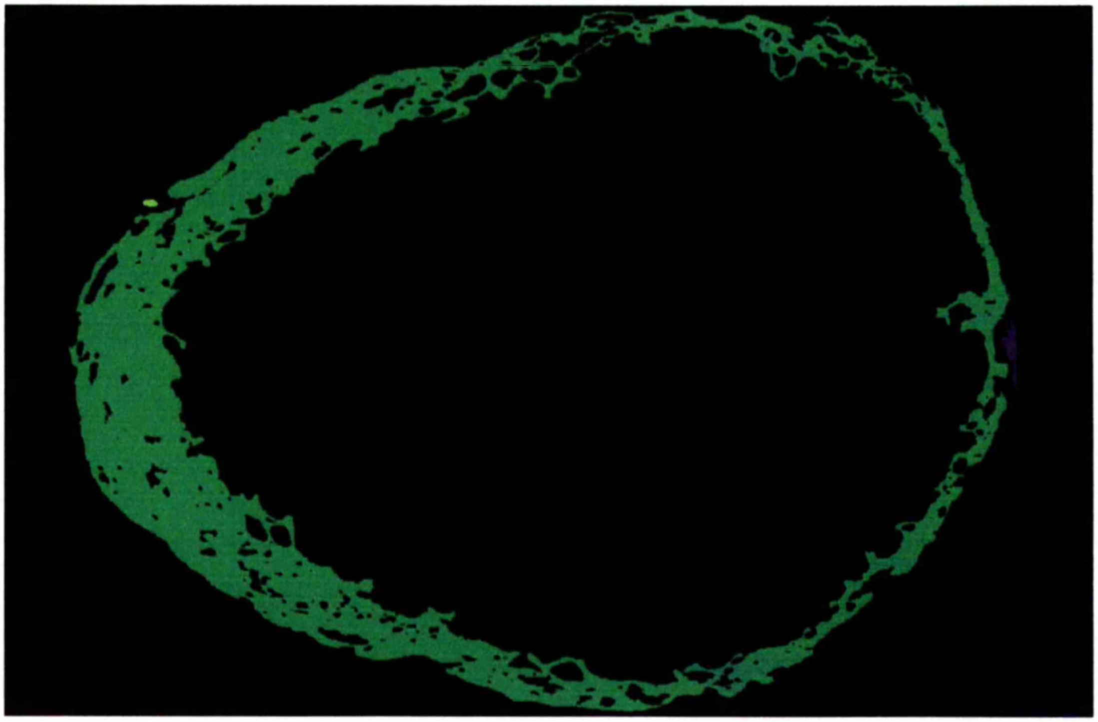

Figure 25. Identified image of femoral neck - Cortical bone.

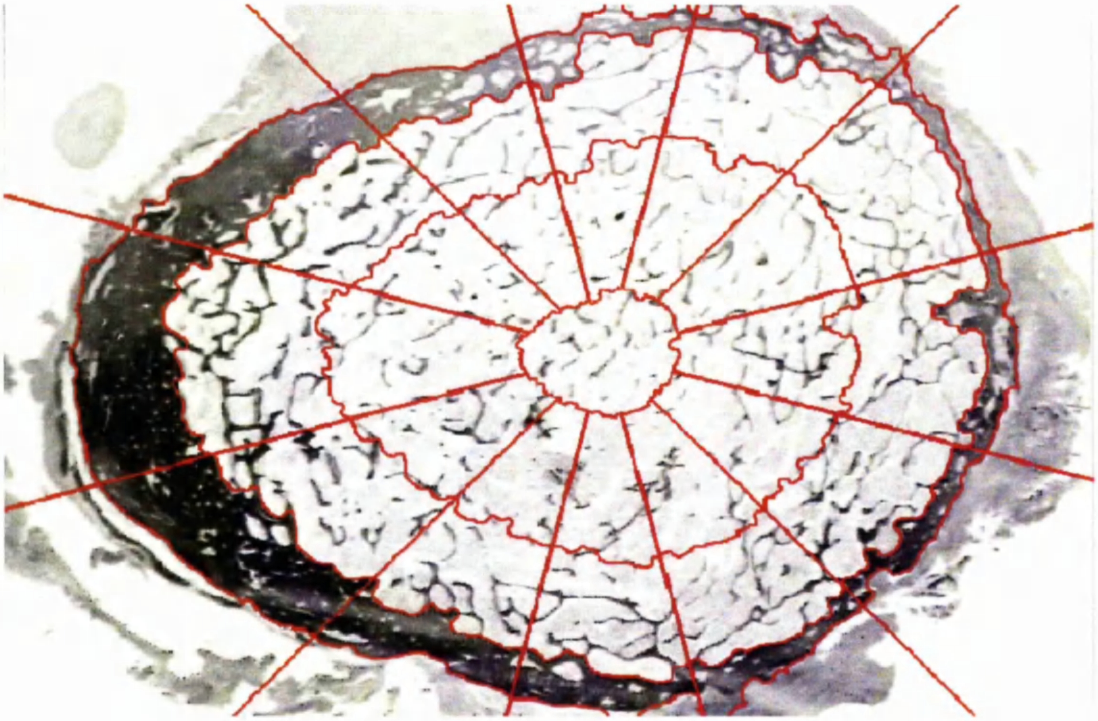

Figure 26. Greyscale image of femoral neck section. Overlay showing distribution sectors.

This ensured that the extreme inferior, anterior, superior and posterior sides of the section were allocated complete 30° slices (Figure 26). The background was eroded, resulting in the lines becoming thicker. This image was then subtracted from the medulla mask (Image Frame 1). This image was stored in Image Frame 6. To produce the 12 outer sectors it was necessary to reduce the medulla mask by one third. This was achieved by using the centre of gravity co-ordinates (cx & cy) and the VIDAS system command *'rotate'*. The command *'rotate'* was used to not only scale the medulla mask down but also to relocate the centre of gravity of the new object. The command achieved this by setting the parameters *ZoomX* and *ZoomY* to 0.66. This command is configured to work on a square image format (512 x512), which keeps the transformation uniform. As a non-square image format was used (768 x 512), an adjustment had to be applied. The variables *cga* and *cgb* were created to contain the value of $-\left(\frac{cx}{3}\right)$ and $-\left(\frac{cy}{3}\right)$, respectively. These variables set the value (in pixels) of the translations in the X and Y direction. The contour of this image was extracted and subtracted from image 6 and the result store in Image Frame 6. To create the inner 12 sectors and the centre sector a further transformation was carried out. This time the parameters *ZoomX* and *ZoomY* were set to 0.2. and the variables *cgx* and *cgy* to contain the value of $-\left(\frac{cx}{1.25}\right)$ and $-\left(\frac{cy}{1.25}\right)$ respectively. This object was added to image 6 and then the contour subtracted. This image was then identified and dilated to fill the spaces between each segment. This resulted in the final medulla segments

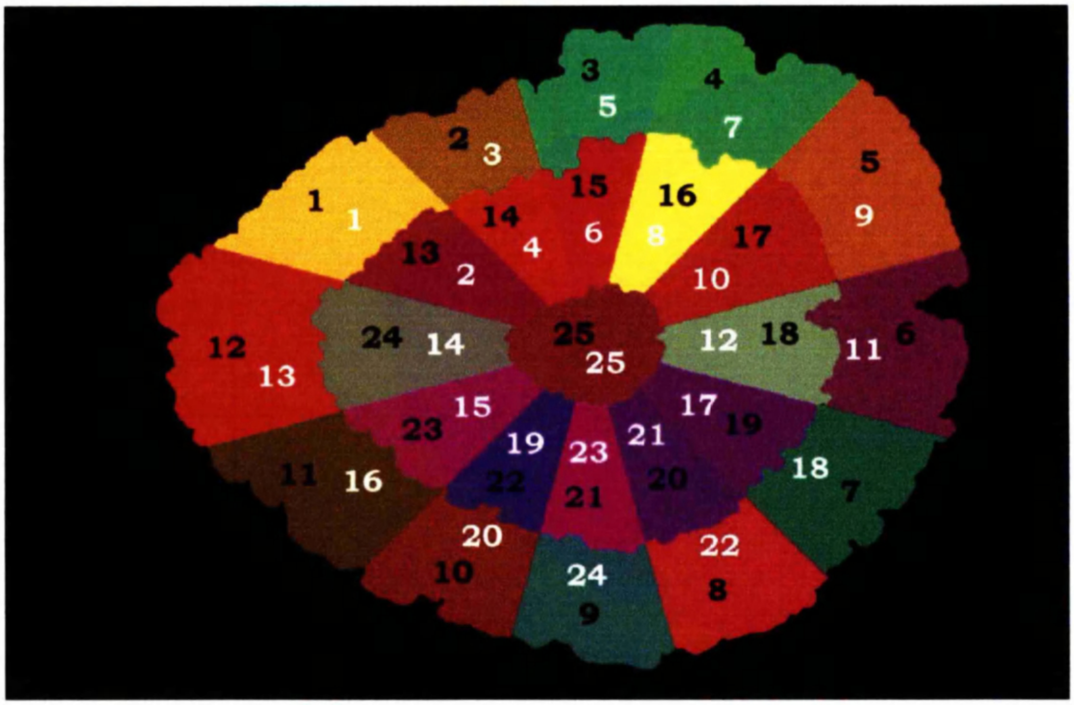

Figure 27. Identified image of the femoral neck medullary sectors. The black numbers are the computed sector order. The white numbers are the system sector order.

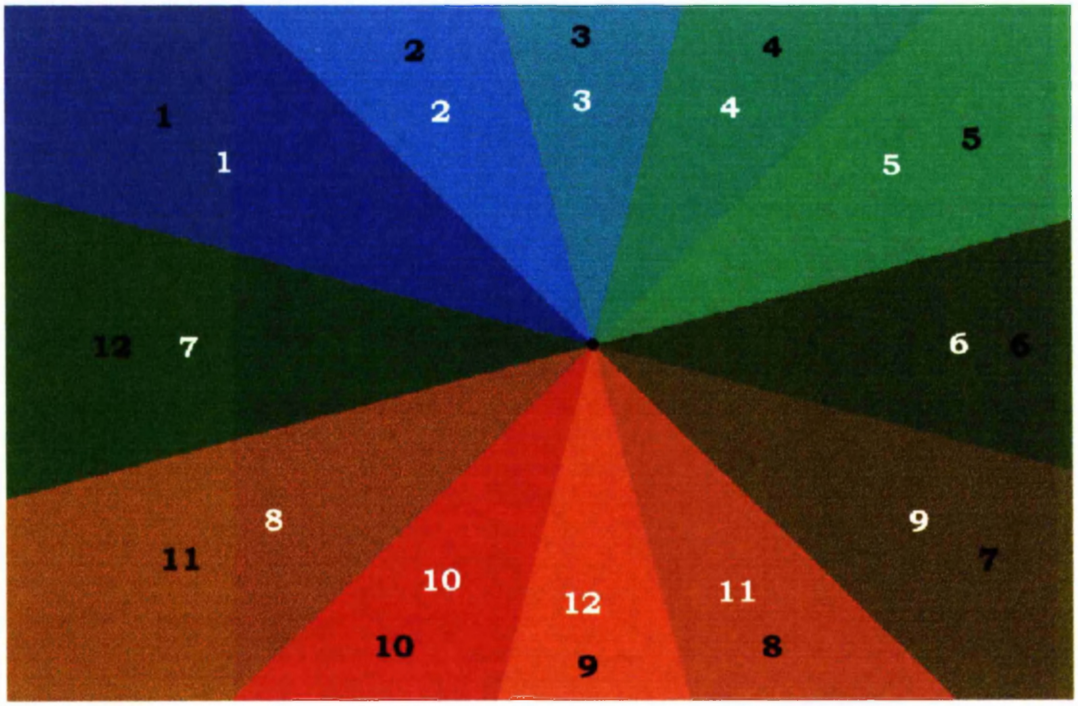

Figure 28. Identified image of the main masks. Black numbers are the computed sector order. White numbers are the system sector order.

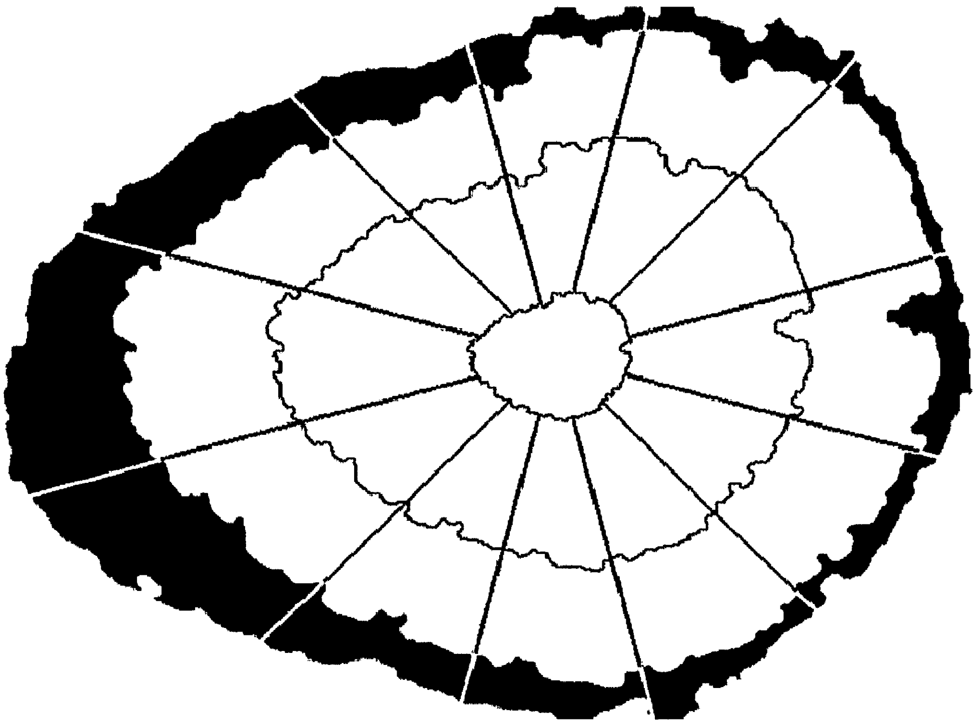

Figure 29. Binary image of the section and sectors. This image was archived for examination of actual section at a macro level.

(Figure 27), which consisted of two concentric rings (inner and outer) of 12 sectors. At any part the junction of the outer and inner rings was two thirds of the radius of the medulla from the centre of gravity. A small central sector of radius one third of the radius of the medulla remained. The image was stored in frame store 6.

Creation of the main masks – The same method of creating 12 radiating lines at 30° intervals was used, as with the creation of the medulla sectors. This time the image was inverted, to create filled slices. The 12 slices were identified, to create individually labelled slices. The image then had the background eroded to fill the spaces between each slice (Figure 28). This image was stored in Image Frame 2. The system printed out a simple image of the sectors, the actual size of the specimen, so that it could be examined at a macro level (Figure 29).

Sector order protocol - In order to compare the distribution of bone from one specimen to another, it was very important that all sectors of the bone were measured in the same order every time. To achieve this each of main sector masks were used in turn to mask the medulla sectors. The main masks were also used to determine the 12 cortical bone sectors. The way in which the VIDAS system finds objects in an image is methodical. When producing an *identified* image, the VIDAS system will scan across the screen, starting at the top left-hand corner of the screen (0, 0). The system will scan the image one scan line at a time. If a pixel is part of an object, the system will label that object, the first object being assigned greylevel 1, the next, greylevel 2 and so on. The main mask image has 12 objects (segments) each of which will be assigned a greylevel 1 – 12. The same main mask was used for all specimens, therefore each segment would always be assigned the same greylevel. The mask command has a greylevel parameter, which can be set or incremented by the macro i.e. an object within one image, which has a particular greylevel, can be used to mask another image. This technique was achieved by incrementing the variable *i* within the for-endfor loop. On each execution of the loop, the mask command would mask the medulla sectors with each of the 12 main masks in the same order each time for every specimen (Figures 30 & 31). Again, as the VIDAS system will measure the object nearest the top of the screen first, the same order will be followed for all specimens. As the order in which the system measured the sectors was morphologically illogical, a list of *'if'* statements were used to assign logical sector number. The centre sector measurement was not included in this procedure. It was simply measured by masking with the central sector mask.

Measurement of trabecular bone – The centre sector 25 was masked and measured first followed by the other 24 sectors which were then measured as described above. Each medulla sector would be used to mask the trabecular bone i.e. the bone which lay beneath each sector was measured (Figure 32). The measurements: *Sasect (Vv) & SAMA* were made (refer to page 55).

Measurement of cortical bone – The main masks, already created, were used again, this time on their own, to mask the cortical bone in Frame Store 3 (Figure 33). The cortical bone, which lay beneath each section, was measured. Again the order in which each section was measured was the same for each specimen. Another list of *'if'* statements were used to assign the proper segment number to each slice. The measurement: *SATS* was made (refer to page 55).

End of loop – Once all measurements were made and input into the various databases, the user would be prompted to either quit, or loop to the start of the macro, to process another specimen.

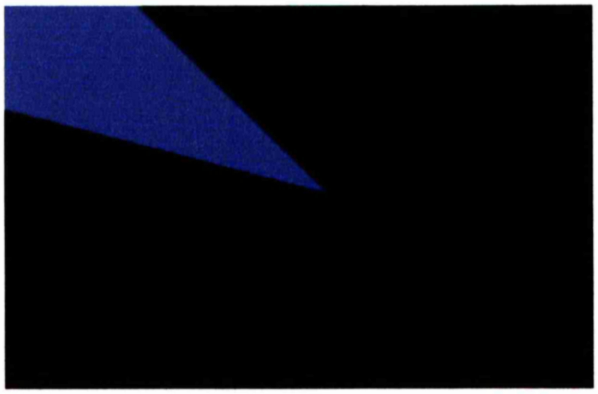

Figure 30. Identified image of a main mask slice.

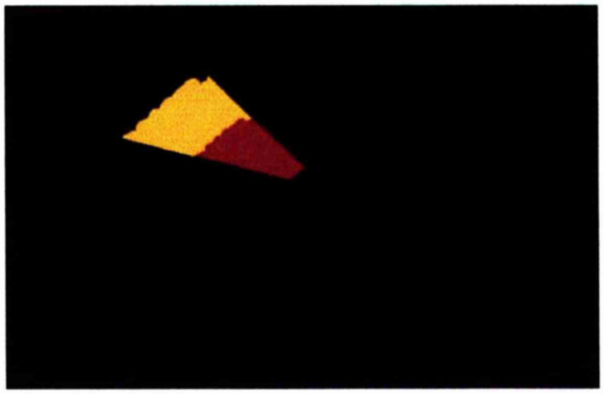

Figure 31. Identified image of medullary sectors masked with main mask.

Figure 32. Identified image of trabecular bone masked with medullary sector.

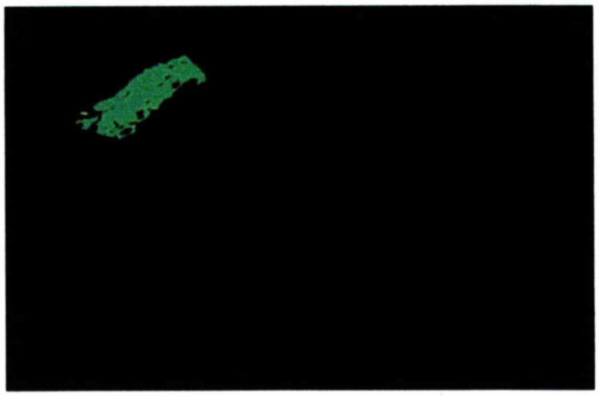

Figure 33. Identified image of cortical bone masked with main mask slice.

Heberden's nodes

Collection and preparation of finger specimens

Fingers were collected from cadavers in the dissecting room of the Laboratory of Human Anatomy.

- 15 Control fingers - Five each of: index, middle and little fingers. These fingers did not show Heberden's nodes.
- 15 Clinically assessed moderate Heberden's nodes - Five each of: index, middle and little fingers. No moderate nodes were found on the ring finger.
- 7 Clinically assessed severe Heberden's nodes (Figure 34) – Two index, two middle and three little fingers.

Radiography of fingers

All specimens were radiographed with the soft tissue X-ray machine. Posteroanterior (Figure 35) and lateral views were obtained for each finger (Figure 36). The film used was Industrex CX Film 100. The exposure time was 7 seconds at 25mV and 10mA for all specimens.

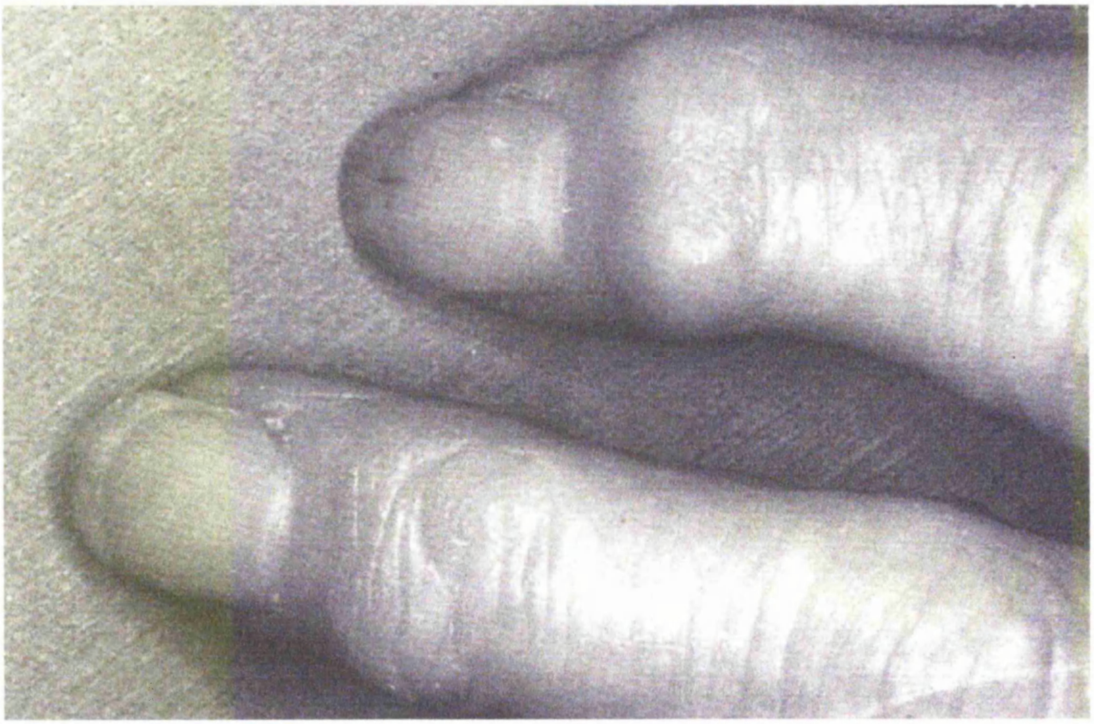

Figure 34. Fingers presenting severe Heberden's nodes.

Image analysis of Heberden's nodes

The VIDAS image analysis system was used to examine radiographs of fingers at the distal interphalangeal joint (Figure 35). The system had to determine whether the morphometric changes observed at the joint (Figure 37) were localised or not. To determine this it was necessary to plot a midline through the heads of the middle phalanges and bases of the distal phalanges. Measurements from these midlines to the most lateral and medial points (posteroanterior plane) and to the most ventral and dorsal points (lateral plane) of the phalanx were taken. As these measurements were taken from a plotted midline, it would be very difficult to accurately obtain these measurements using callipers, but ideally suited to image analysis.

The radiographic films were processed and analysed on the VIDAS system with the aid of a purpose written macro (Figure 38), (Appendix C). Feret dimensions (diameters in the X and Y planes) were made.

Resolution – The image size was set to 512 x 512 pixels. The VIDAS frame store can support twelve images of this format, in the memory at any one time. These extra frames were necessary to facilitate the image processing.

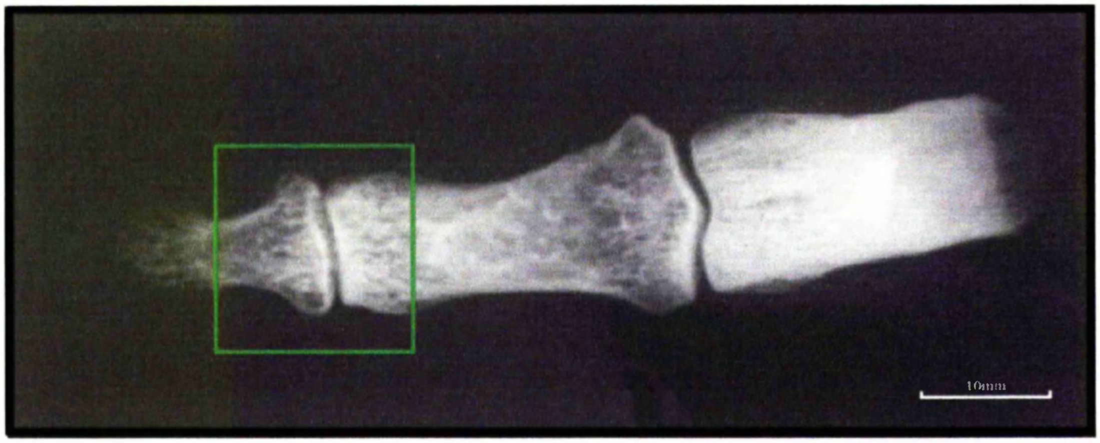

Figure 35. Radiograph of control finger in posteroanterior plane. Distal interphalangeal joint is highlighted.

Figure 36. Radiograph of control finger in lateral plane.

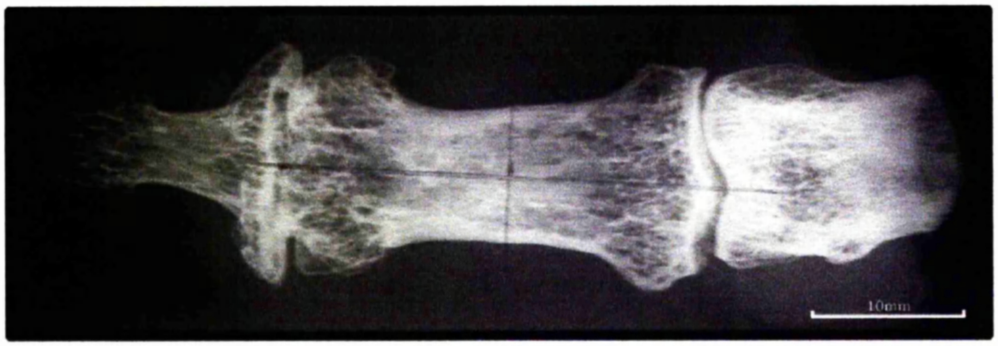

Figure 37. Radiograph of finger with severe Heberden's nodes. Posteroanterior plane.

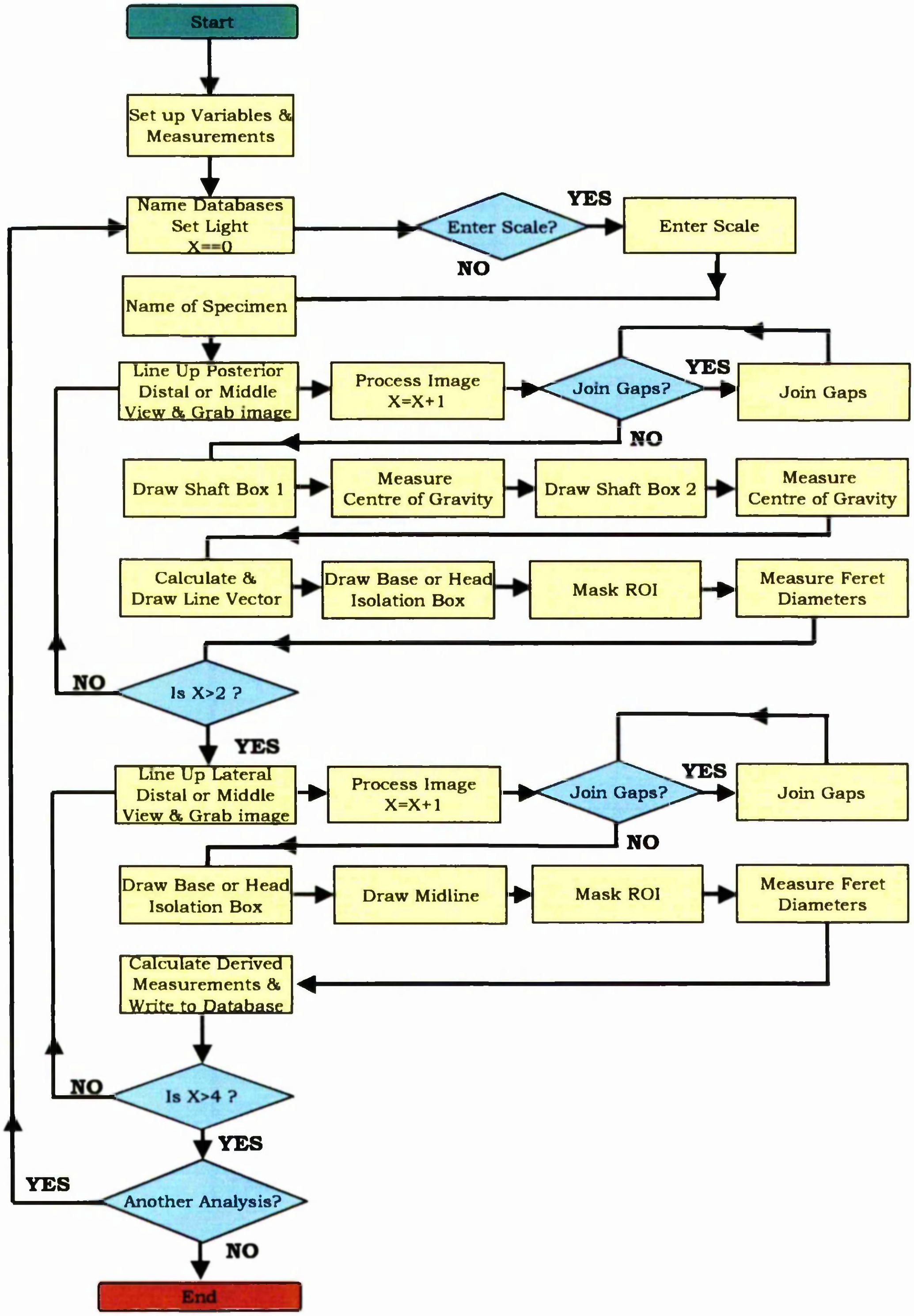

Figure 38. Flow chart of image analysis macro - Heberden's node (Appendix C).

Variables and measurement parameters – The measurements the system would make were: *AREA, CGRAVX, CGRAVY, FERETX* & *FERETY.* Although only Feret diameter measurements were used the area measurements were retained for possible future analysis. The *CGRAVX* and *CGRAVY* (centre of gravity) measurements were necessary for the processing of the midline. Variables were defined to allow derived measurements to be calculated. Measurements and associated variables were defined as:

Feret dimensions of:

Distal phalanx, posteroanterior plane at distal interphalangeal joint.

Midline – Most prominent lateral point (Y Axis) = *LEN1*
Midline – Most prominent medial point (Y Axis) = *LEN2*
LEN1 + *LEN2* = *LEN3*

Middle phalanx, posteroanterior plane at distal interphalangeal joint.

Midline – Most prominent lateral point (Y Axis) = *LEN4*
Midline – Most prominent medial point (Y Axis) = *LEN5*
LEN4 + *LEN5* = *LEN6*

Distal phalanx, lateral plane at distal interphalangeal joint.

Midline – Most prominent dorsal point (Y Axis) = *LEN7*
Midline – Most prominent ventral point (Y Axis) = *LEN8*
LEN7 + *LEN8* = *LEN9*

Middle phalanx, lateral plane at distal interphalangeal joint.

Midline – Most prominent dorsal point (Y Axis) = *LEN10*
Midline – Most prominent ventral point (Y Axis) = *LEN11*
LEN10 + *LEN11* = *LEN12*

Lateral plane, phalanx length.

Distal phalanx, total length (X Axis) = *CDLAT*

Middle phalanx total length (X Axis) = *CMLAT*

To accommodate the differences in finger size the following derived ratios were calculated by the macro:

$$DLEN1 = \frac{LEN1}{CDLAT}$$

$$DLEN2 = \frac{LEN2}{CDLAT}$$

$$DLEN4 = \frac{LEN4}{CMLAT}$$

$$DLEN5 = \frac{LEN5}{CMLAT}$$

$$DLEN7 = \frac{LEN7}{CDLAT}$$

$$DLEN8 = \frac{LEN8}{CDLAT}$$

$$DLEN10 = \frac{LEN10}{CMLAT}$$

$$DLEN11 = \frac{LEN11}{CMLAT}$$

(See Figures 39 & 40).

Data would be stored in two databases, one for raw data and the other for the derived data.

Main loop - The main *'while-endwhile loop'* would begin. The main *'while-endwhile loop'* was divided into two further nested *'while-endwhile loops'*. The first loop would be used to measure the phalanges in the

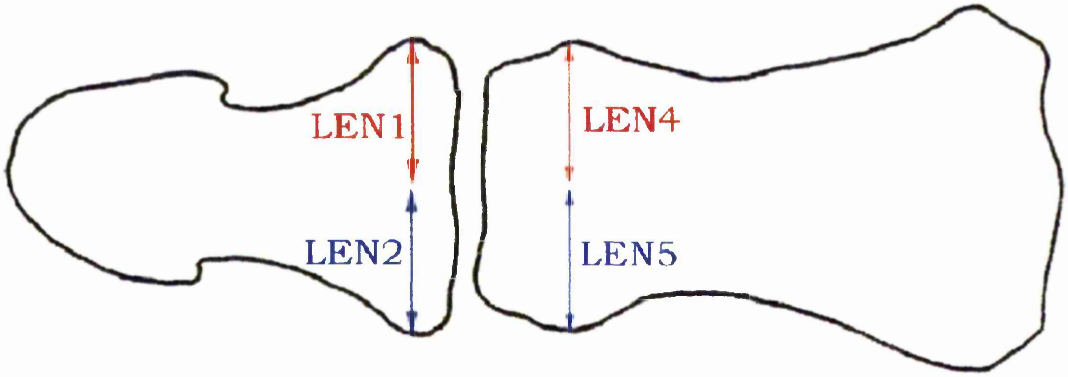

Figure 39. Drawing of distal and middle phalanges in the posteroanterior plane showing Feret diameters to be measured.

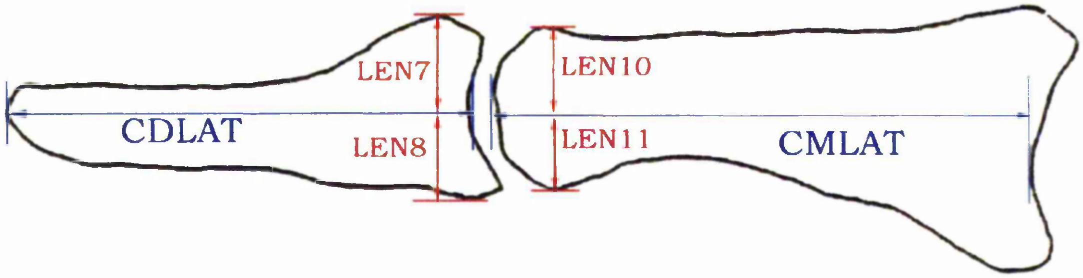

Figure 40. Drawing of distal and middle phalanges in the lateral plane showing Feret diameters to be measured.

posteroanterior plane and the second loop would be used to measure the phalanges in the lateral plane. As there were two phalanges, each loop would execute twice. The variable *'x'* would increment each time the loop executed (used to determine what messages would be displayed for the user and the value of certain imaging parameters).

Scaling – The same scale and magnification was used throughout the experiment. The system measured scale references in both X and Y planes.

Image Acquisition – The user positioned the radiographic image of the phalanx on a grid marked on the light viewing box. This grid helped the user to get the finger as parallel to the x plane as possible. Small variations in the position of the radiograph in the x plane would not effect the position of the midline. The image would then be digitised (Figure 41).

Segmentation of the phalanges – A contrast adjustment was performed on the digitised image. The image was then segmented. The method used was the dynamic thresholding method *'disdyn'*. As the objects were relatively large, the matrix size was also set high (25). A series of image processing functions was then carried out; *scrap, dilate, fill & erode* in an attempt to remove noise and artefacts.

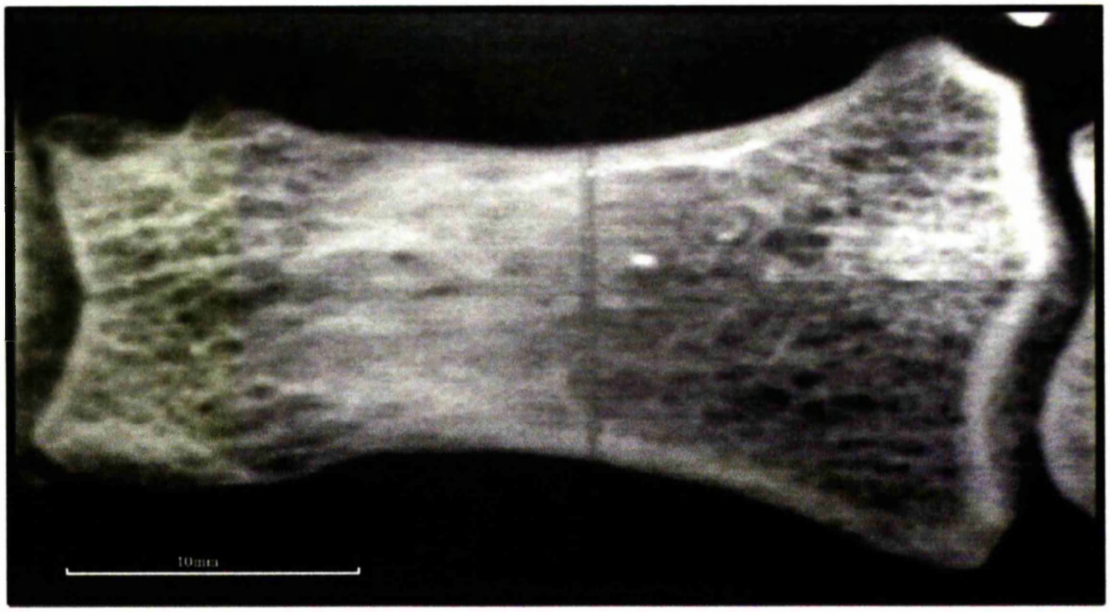

Figure 41. Control finger. Middle phalanx in posteroanterior plane. Greyscale image.

Manual image processing – Radiographs can sometimes produce an artefact shadow of the bone around the outside edge of the bone, which makes edge detection difficult. They can also produce a poor 'grainy' background in the image. These shadows and background artefacts can be extremely difficult to eliminate by automated means. Different methods were tried to achieve full automation of the image processing, with only partial success i.e. some radiographs would process well and others would not. It was found that the best solution was to under-segment the phalanx. On most specimens this was not necessary, but the macro had to account for specimens that would require it. This under-segmentation could result in some parts of the phalanx being missing (around the periphery) in the binary image. The advantage was that no object shadows and background artefacts would be segmented, therefore these would not be present in the resulting binary image. The binary image could then be super-imposed over the greyscale image and the user asked to manually correct the image, by joining any gaps on the periphery of the phalanx.

Determination of the midline on posteroanterior plane images – The problem of determining a midline was overcome by using the shaft of the phalanx as a guide to where the midline lay. It was possible to plot a centre line through the shaft, which was then extended to the end of the phalanx. The shaft was chosen as it was considered to be uniform in shape around the midline and unaffected by disease. The distal phalanx was processed first with exactly the same steps carried out on the middle phalanx, except for the direction to which the lines were drawn i.e. the line was drawn towards the right of the screen on the distal phalanx and to the left of the screen on the middle phalanx. The operator was presented with a binary image of the phalanx. Two thin boxes would be drawn on the shaft of the phalanx (Figure 42). Each box would then be converted into a mask. These thin boxes would mask the binary image of the phalanx, which would result in two thin slices. These slices could then be measured for their centres of gravity (Figure 43). The co-ordinates were installed into four integer variables *'acx'*, *'acy'* for box 1 and *'bcx'* *'bcy'* for box 2. A vector line was drawn in the *'overlay plane'* joining the points and extending the line in the X-axis (Figure 44), the direction of which depended on which phalanx was being processed.

Isolating the head or base of phalanx and creating the two objects on each side of the midline – As Feret diameters of the head or base of the phalanges were to be measured it was necessary to isolate the heads of the middle phalanges and bases of the distal phalanges from the rest of the phalanx. This would ensure that the Feret diameters measured would not be of another part of the phalanx. The user was prompted to draw a box around the part of the phalanx adjacent to the interphalangeal joint (Figure 45). The box was converted to a binary image, filled and then used to mask the binary image of the phalanx. The resulting image (the isolated head or base of phalanx) was then eroded by one iteration. The previously plotted midline was then converted into a binary image and subtracted from base or head binary

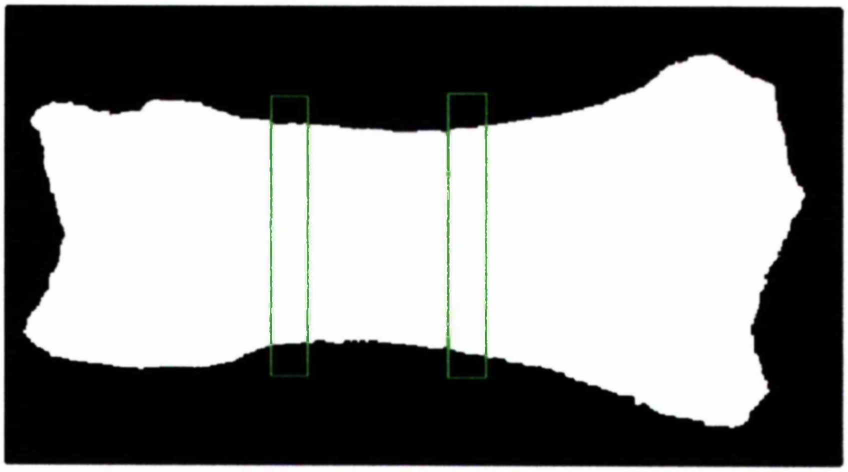

Figure 42. Control finger. Middle phalanx in posteroanterior plane. Binary image showing two manually drawn boxes on the phalanx shaft.

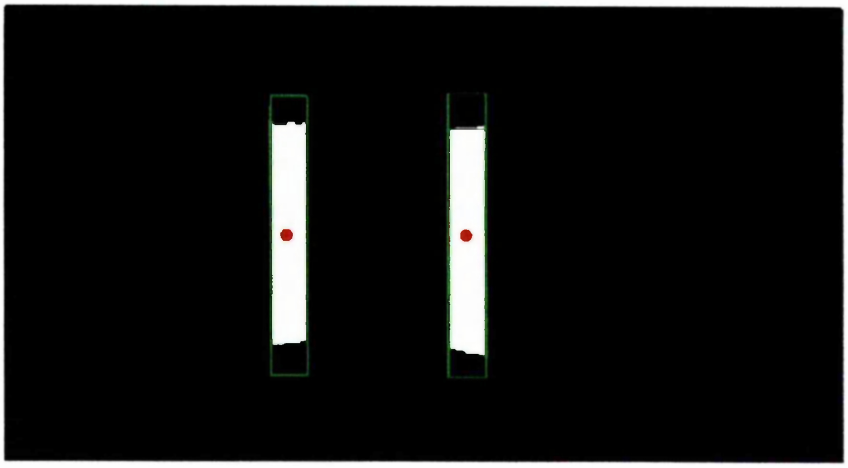

Figure 43. Boxes are used to mask the phalanx shaft. The centre of gravity is plotted.

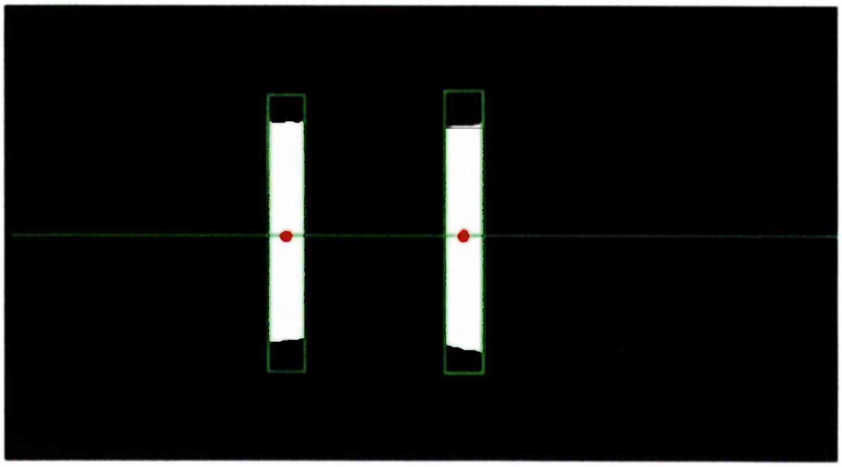

Figure 44. A vector line is plotted through the centre of gravities.

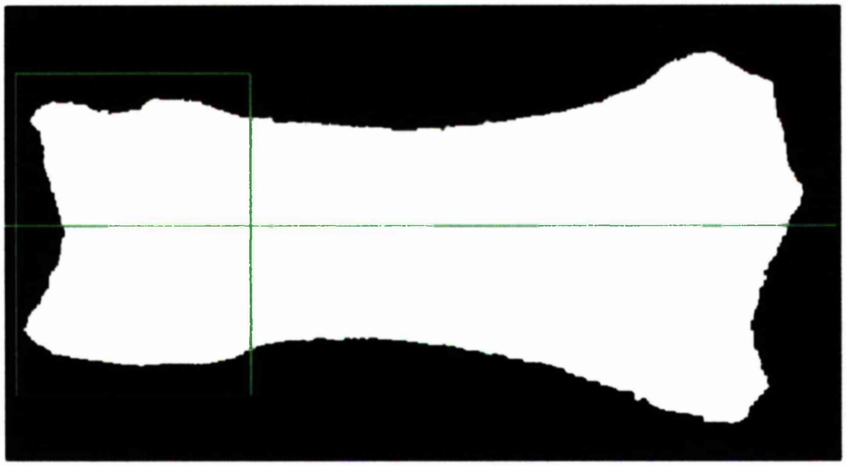

Figure 45. Binary image of middle phalanx. Shows manually drawn box.

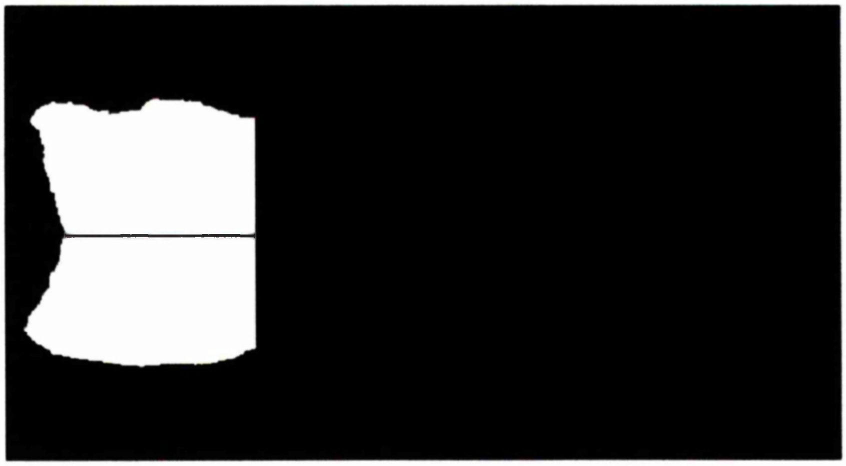

Figure 46. The box and the line are used to mask the binary image.

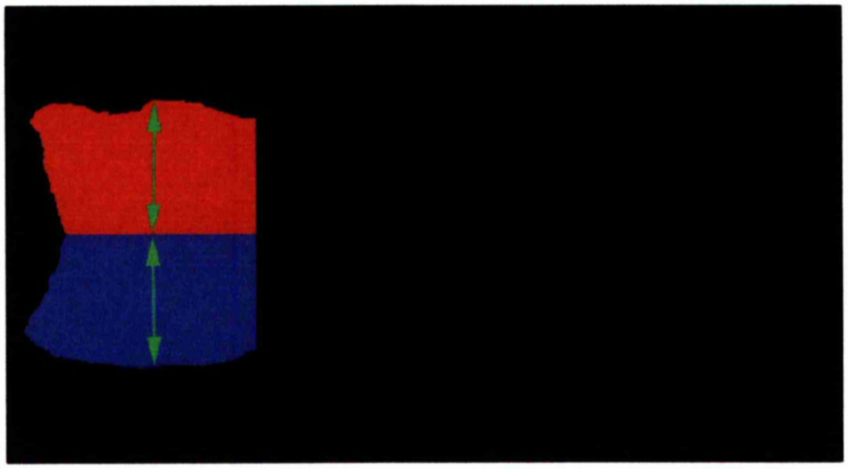

Figure 47. Identified image dilated to fill the gap made by the line. Arrows show the widths measured by the system.

image (Figure 46). This resulted in two objects. The image was *'identified'* (Figure 47). The objects were dilated again by one iteration. Since an earlier erosion had been performed, this ensured that the midline was removed without dilating the outside perimeter of the objects. The measurements detailed above were then made.

Radiographs in the lateral plane - After the radiographs of the two phalanges of the posteroanterior view had been measured the user was prompted to frame the lateral view (Figure 48) of the same specimen and again measure the distal and middle phalanges. The same processing operations were carried out to produce the binary image of the phalanx in this view as were used in the posteroanterior radiographs (Figure 49).

Determination of the midline on lateral plane images – The process of plotting a midline, calculated from phalanx shaft centroids, could not be used on the lateral plane radiographs, as the morphometry of the shaft in the lateral plane is not symmetrical. The midlines were manually drawn on the radiographs by drawing a line from the most distal point of the articular surface of the distal phalanx to its tip and from the most distal point of the articular surface of middle phalanx at the proximal interphalangeal joint to the most distal point of the articular surface of the middle phalanx at the distal interphalangeal joint. After isolating the base or head of the phalanx by drawing a ROI (Figure 50), the operator was then asked to draw a midline, in the VIDAS graphics plane, over the midline drawn on the radiograph. This line was then converted to a binary image and used as a mask to divide the binary image of the isolated phalanx head or base (Figure 51). The same processing operations were carried out to produce the two halves of the head or base of the phalanx as were used in the posteroanterior radiographs. The image was *'identified'* (Figure 52). The maximum Feret diameter in the X plane (phalanx length) was measured from the binary image of the phalanx in the lateral plane. All other measurements were then made as detailed above.

End of loop – Once all measurements and derived measurements were made and written into the various databases, the user would be prompted to measure another specimen or quit the macro.

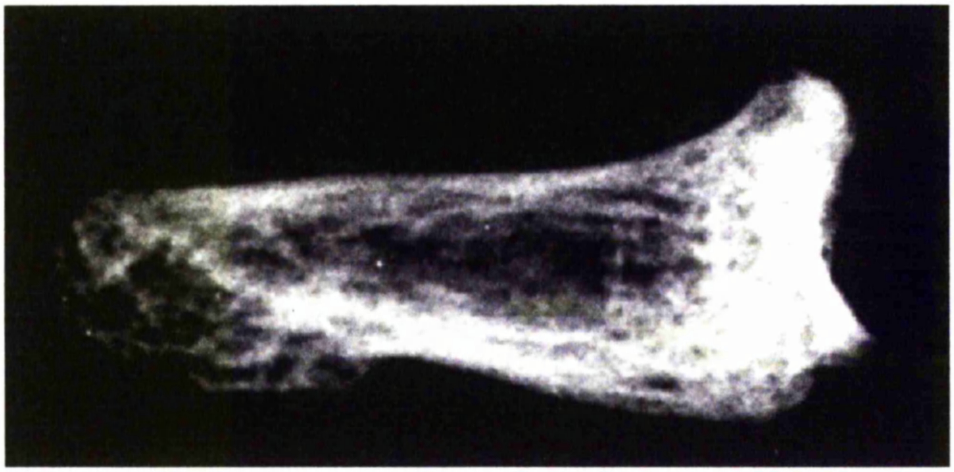

Figure 48. Control finger – distal phalanx. Grey scale lateral plane.

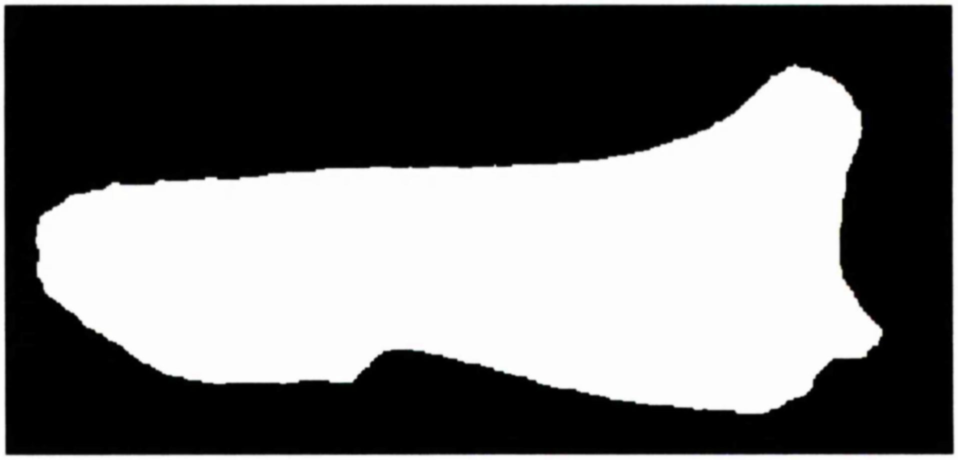

Figure 49. Control finger – distal phalanx. Binary image.

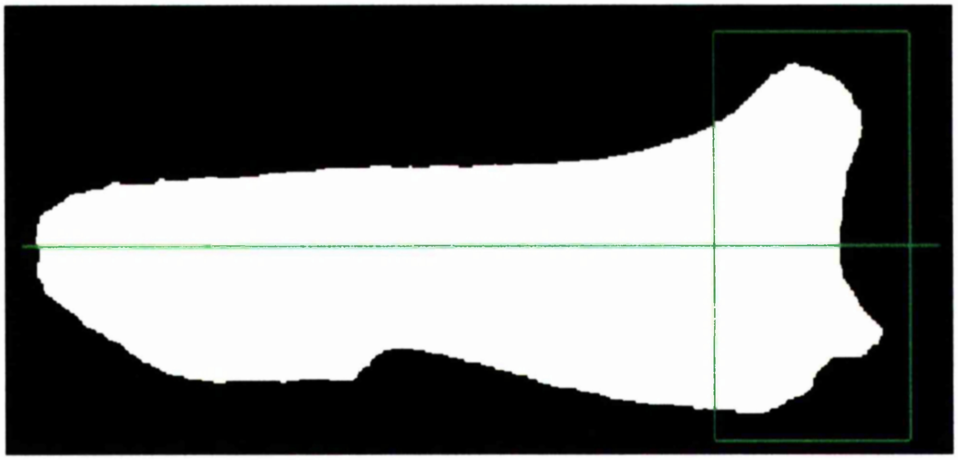

Figure 50. User defined ROI to isolate base of phalanx and midline. Midline in the graphics overlay shown.

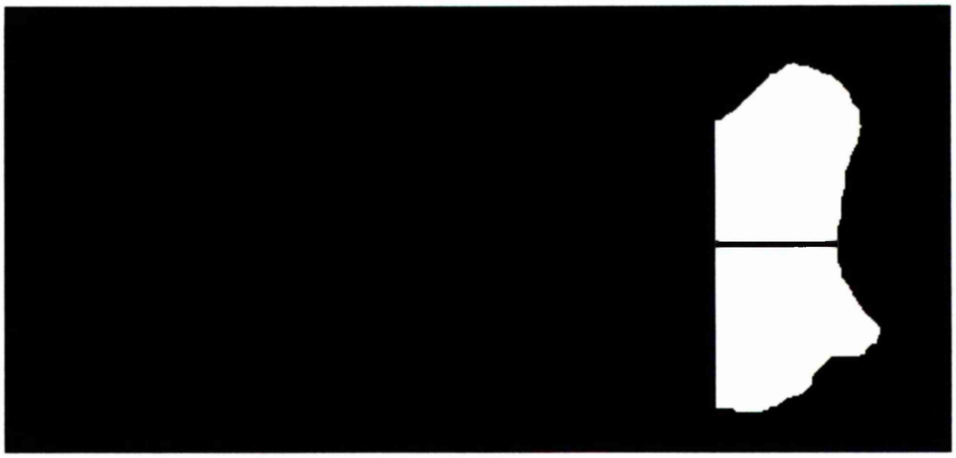

Figure 51. The box and the line are used to mask the binary image.

Figure 52. Identified image dilated to fill the gap made by division line. Measured Feret diameters indicated.

Statistics

Image analysis tests

Microsoft Excel 2000 utilising the "Data analysis tool pack" was used to analyse the image analysis results.

The mean percentage difference was calculated for each test. On the system tests this mean represents an estimate of bias. The standard deviation of the percentage difference is an estimate of random error in the measurements (Parkinson & Fazzalari, 1994).

To determine the amount of variance within and between the measurements a single factor analysis of variance was carried out for each test. This would determine whether any difference within or between data was significant or not.

Femoral head, neck and Heberdens Nodes.

Analyses of variance were carried out using Statistical Graphics Corporation Statgraphics version 2.6 computer package. All other statistical tests were performed with Minitab version 9 statistics package.

Results

Results

Image analysis system and operator tests

Intra observer error

The amount of intra-operator error was tested at every stage of user interactivity in the femoral neck macro.

Scaling – The level of error produced by the scaling/ re-scaling operation was determined. The mean of all measured areas was calculated and the percentage difference, from this mean, for each measurement was determined. The mean percentage difference and standard deviation was found to be:

0.29 ± 0.18%.

The standard deviation of the percentage difference is an estimate of random error in the measurements.

A one-way analysis of variance was carried out to compare each run, which were performed on successive days.

Anova: Single Factor Scaling						
SUMMARY						
Groups	*Count*	*Sum*	*Average*	*Variance*		
Run 1	10	9238.90	923.89	5.50		
Run 2	10	9256.27	925.63	9.18		
Run 3	10	9258.05	925.81	14.99		
ANOVA						
Source of Variation	*SS*	*df*	*MS*	*F*	***P-value***	*F crit*
Between Groups	22.38	2	11.19	1.13	**0.34**	5.49
Within Groups	267.08	27	9.89			
Total	289.46	29				

Table 1. Analysis of Variance – Scaling.

This test shows no significant difference between and within each run.

Focus – The amount of error produced by the focus/ re-focus operation was determined. The mean of all measured areas was calculated and the percentage difference, from this mean, for each measurement calculated. The mean percentage difference and standard deviation was found to be:

0.37 ± 0.29%.

The standard deviation of the percentage difference is an estimate of random error in the measurements.

A one-way analysis of variance was carried out to compare each run.

Anova: Single Factor - Focus						
SUMMARY						
Groups	*Count*	*Sum*	*Average*	*Variance*		
Run 1	10	9245.59	924.56	16.86		
Run 2	10	9209.05	920.91	17.98		
Run 3	10	9257.98	925.80	11.86		
ANOVA						
Source of Variation	*SS*	*df*	*MS*	*F*	***P-value***	*F crit*
Between Groups	129.42	2	64.71	4.156	**0.02**	5.49
Within Groups	420.38	27	15.57			
Total	549.80	29				

Table 2. Analysis of Variance – Focus.

This test shows a significant difference between and within each of the runs with the degree of significance being P < 0.05.

Cortical bone thresholding – The amount of error produced by an expert user (MN) whilst performing the cortical bone threshold operation was determined. The mean of all measured areas was calculated and the percentage difference, from this mean, for each measurement calculated. The mean percentage difference and standard deviation was found to be:

1.13 ± 1.16%.

The standard deviation of the percentage difference is an estimate of random error in the measurements.

A one-way analysis of variance was carried out to compare each run.

Anova: Single Factor - Cortical Thresholding						
SUMMARY						
Groups	*Count*	*Sum*	*Average*	*Variance*		
Run 1	10	555.93	55.59	1.22		
Run 2	10	558.19	55.82	0.96		
Run 3	10	562.86	56.29	0.26		
ANOVA						
Source of Variation	*SS*	*df*	*MS*	*F*	***P-value***	*F crit*
Between Groups	2.5	2	1.25	1.54	**0.23**	5.49
Within Groups	21.92	27	0.81			
Total	24.42	29				

Table 3. Analysis of Variance – Cortical Thresholding.

This shows no significant difference between and within each run.

Trabecular bone thresholding – The amount of error produced by an expert user (MN) whilst performing the trabecular bone threshold operation was determined. The mean of all measured areas was determined and the percentage difference, from this mean, for each measurement calculated. The mean percentage difference and standard deviation was found to be:

2.9 ± 1.8%.

The standard deviation of the percentage difference is an estimate of random error in the measurements. A one-way analysis of variance was carried out to compare the difference in total trabecular area.

Anova: Single Factor - Total Trabecular Area						
SUMMARY						
Groups	*Count*	*Sum*	*Average*	*Variance*		
Run 1	10	654.42	65.44	4.16		
Run 2	10	652.72	65.27	8.1		
Run 3	10	644.44	64.44	3.42		
ANOVA						
Source of Variation	*SS*	*df*	*MS*	*F*	***P-value***	*F crit*
Between Groups	5.7	2	2.85	0.55	**0.59**	5.49
Within Groups	141.14	27	5.23			
Total	146.84	29				

Table 4. Analysis of Variance – Trabecular bone area.

This shows no significant difference between and within each run.

The mean percentage difference and standard deviation of the number of trabecular profiles was found to be:

1.03 ± 0.77%.

A one-way analysis of variance was carried out to compare the difference in trabecular profile count.

Anova: Single Factor - Trabecular Count						
SUMMARY						
Groups	*Count*	*Sum*	*Average*	*Variance*		
Run 1	10	3074	307.4	19.38		
Run 2	10	3081	308.1	25.21		
Run 3	10	3060	306.0	4.44		
ANOVA						
Source of Variation	*SS*	*df*	*MS*	*F*	***P-value***	*F crit*
Between Groups	22.87	2	11.43	0.70	**0.51**	5.49
Within Groups	441.30	27	16.34			
Total	464.17	29				

Table 5. Analysis of Variance – Trabecular profile count.

This shows no significant difference between and within each run.

Non-expert intra observer error – The results obtained by two non-expert operators (RK and EP) were analysed for any difference within each user's runs. The mean of each user's area and count measurements were calculated and the percentage difference, from this mean, for each measurement calculated. The mean percentage differences and standard deviations were found to be:

Run	**Mean and Standard Deviation of % Difference from own mean - Area**	**Mean and Standard Deviation of % Difference from own mean - Count**
RK Run 1	5.14 ± 3.18%	1.61 ± 0.90%
RK Run 2	6.36 ± 3.81%	3.53 ± 2.37%
EP Run 1	8.04 ± 6.30%	7.21 ± 5.00%
EP Run 2	1.94 ± 2.49%	2.34 ± 2.60%

Table 6. Non-expert user percentage difference from own means.

A one-way analysis of variance was carried out to compare the difference between each of the non-expert users' runs for area measurement.

Anova: Single Factor Within RK Area						
SUMMARY						
Groups	*Count*	*Sum*	*Average*	*Variance*		
Run 1	10	658.02	65.80	17.06		
Run 2	10	694.23	69.42	28.68		
ANOVA						
Source of Variation	*SS*	*df*	*MS*	*F*	***P-value***	*F crit*
Between Groups	65.59	1	65.56	2.87	**0.11**	8.29
Within Groups	411.73	18	22.87			
Total	477.32	19				

Table 7. Analysis of Variance – Variance between RK runs (area).

Anova: Single Factor Within EP Area						
SUMMARY						
Groups	*Count*	*Sum*	*Average*	*Variance*		
Run 1	10	750.68	75.07	62.87		
Run 2	10	787.14	78.71	6.47		
ANOVA						
Source of Variation	*SS*	*df*	*MS*	*F*	***P-value***	*F crit*
Between Groups	66.47	1	66.47	1.92	**0.18**	8.29
Within Groups	624.03	18	34.67			
Total	690.50	19				

Table 8. Analysis of Variance – Variance between EP runs (area).

Both results for comparison of non-expert runs, to each other, show no significant difference between and within each run.

Inter observer error

The amount of error between the three operators was tested.

The mean of all MN's (Expert) measurements was calculated. This value was used as the base measurement against which to compare each of the other users' measurements. The percentage difference, from MN's means, for each measurement was calculated. The mean percentage differences and standard deviations were found to be:

Run	**Mean and Standard Deviation of % Difference from MN mean - Area**	**Mean and Standard Deviation of % Difference from MN mean - Count**
RK Run 1	5.20 ± 3.44%	1.53 ± 1.19%
RK Run 2	9.28 ± 4.71%	4.54 ± 3.90%
EP Run 1	16.48 ± 10.50%	11.45 ± 9.80%
EP Run 2	21.00 ± 3.90%	15.64 ± 4.15%

Table 9. Non-expert user percentage difference from expert mean.

A one-way analysis of variance was carried out to compare the difference between all three operators.

Anova: Single Factor – Trabecular Area						
SUMMARY						
Groups	*Count*	*Sum*	*Average*	*Variance*		
MN	20	1307.14	65.36	5.81		
RK	20	1352.25	67.61	25.12		
EP	20	1537.82	76.89	36.34		
ANOVA						
Source of Variation	*SS*	*df*	*MS*	*F*	***P-value***	*F crit*
Between Groups	1494.74	2	747.37	33.33	**< 0.001**	4.99
Within Groups	1278.26	57	22.43			
Total	2773	59				

Table 10. Analysis of Variance – User variance (area).

Anova: Single Factor – Trabecular Count						
SUMMARY						
Groups	*Count*	*Sum*	*Average*	*Variance*		
MN	20	6155	307.75	21.25		
RK	20	6279	313.95	139.73		
EP	20	6969	348.45	580.26		
ANOVA						
Source of Variation	*SS*	*df*	*MS*	*F*	***P-value***	*F crit*
Between Groups	19234.53	2	9617.27	38.92	**< 0.001**	4.99
Within Groups	14083.65	57	247.08			
Total	33318.18	59				

Table 11. Analysis of Variance – User variance (count).

Both results for measured area and trabecular count show a highly significant difference between and within each of the runs with the degree of significance being $P < 0.001$.

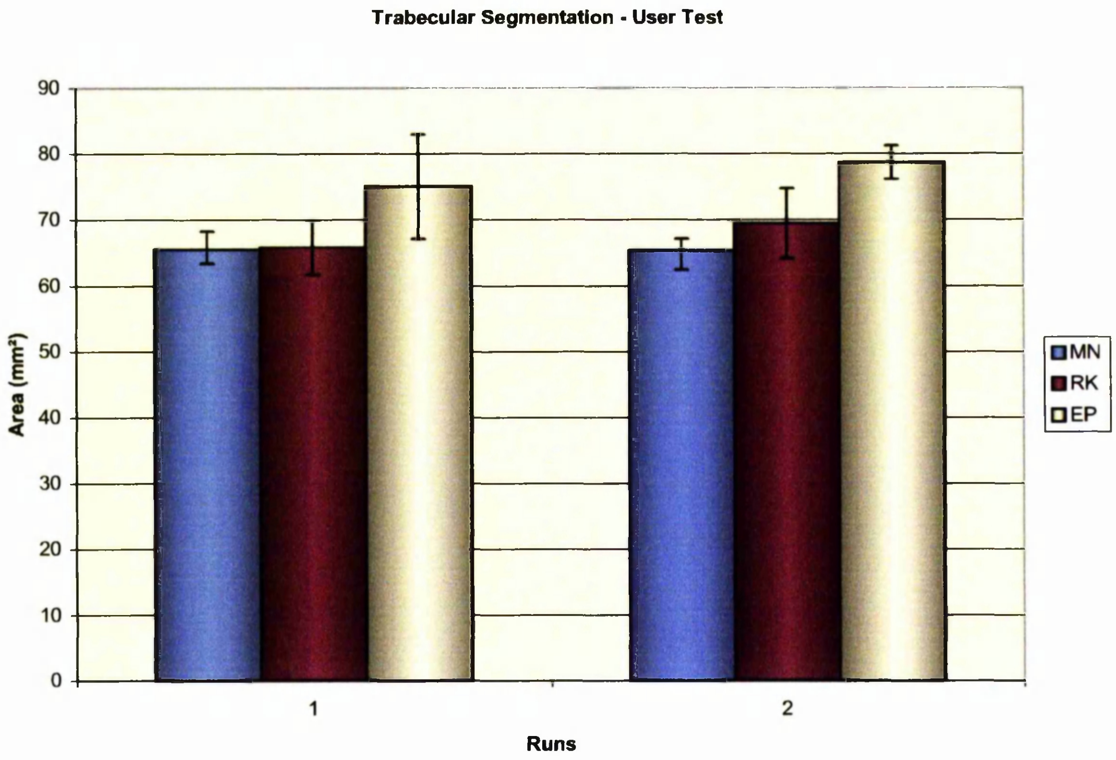

Chart 1. Measured area of trabecular bone – Three different operators.

Magnification effects

The tests were carried out at: low magnification, medium magnification and high magnification to ascertain whether a fractal effect (Coastline of Britain effect) (Mandelbrot, 1967) on the measured area was present. The magnification factor relative to the low magnification were as follows:

Run	**Relative Magnification**
High	x 1.25
Medium	x 1.10
Low	x 1.00

Table 12. Relative magnifications.

The percentage difference from the mean of the high magnification was calculated for the three magnification values.

% Difference Compared to High Mean				
Mag	Mean	High Mean	% Diff Squared	% Diff
High	925.49	925.49	0	**0**
Medium	924.54	925.49	0.010583208	**0.102874722**
Low	922.89	925.49	0.079280743	**0.281568364**

Table 13. Percentage difference of medium and low magnifications compared to the mean of the high magnification result.

A one-way analysis of variance was carried out to compare the difference between all three magnifications.

Anova: Single Factor – Magnification 1.0x – 1.24x						
SUMMARY						
Groups	*Count*	*Sum*	*Average*	*Variance*		
High Mag. (x1.25)	10	9254.95	925.49	13.92		
Med Mag. (x1.1)	10	9245.42	924.54	6.29		
Low Mag. (x 1.0)	10	9228.89	922.89	4.05		
ANOVA						
Source of Variation	*SS*	*df*	*MS*	*F*	***P-value***	*F crit*
Between Groups	34.77	2	17.39	2.15	**0.14**	5.49
Within Groups	218.37	27	8.09			
Total	253.14	29				

Table 14. Analysis of Variance – Magnification level.

This test shows no significant difference between and within each magnification.

As the magnification reduces the measured area reduces. This is due to the relative step-size increasing. Although the magnifications used in this experiment did not show a statistical significant difference in measured area, a further experiment was carried out to ascertain the level of reduced magnification that would return a significant difference. This was found to be at 1.4 times.

A one-way analysis of variance was carried out to compare the difference between all four magnifications.

Anova: Single Factor - Magnification 1.0x - 1.4x						
SUMMARY						
Groups	*Count*	*Sum*	*Average*	*Variance*		
High Mag. (x1.4)	10	9254.95	925.49	13.92		
Med Mag. (x1.1)	10	9245.41	924.54	6.29		
Low Mag. (x1.24)	10	9228.89	922.89	4.05		
Lower Again (x1.4)	10	9190.16	919.02	13.73		
ANOVA						
Source of Variation	*SS*	*df*	*MS*	*F*	***P-value***	*F crit*
Between Groups	244.85	3	81.62	8.6	**< 0.001**	4.38
Within Groups	341.94	36	9.5			
Total	586.79	39				

Table 15. Analysis of Variance – Magnification level (1.0x – 1.4x).

These tests show a highly significant difference between and within each of the runs with the degree of significance being P < 0.001.

The following chart graphically demonstrates a regression effect, on measured area, by reducing the magnification.

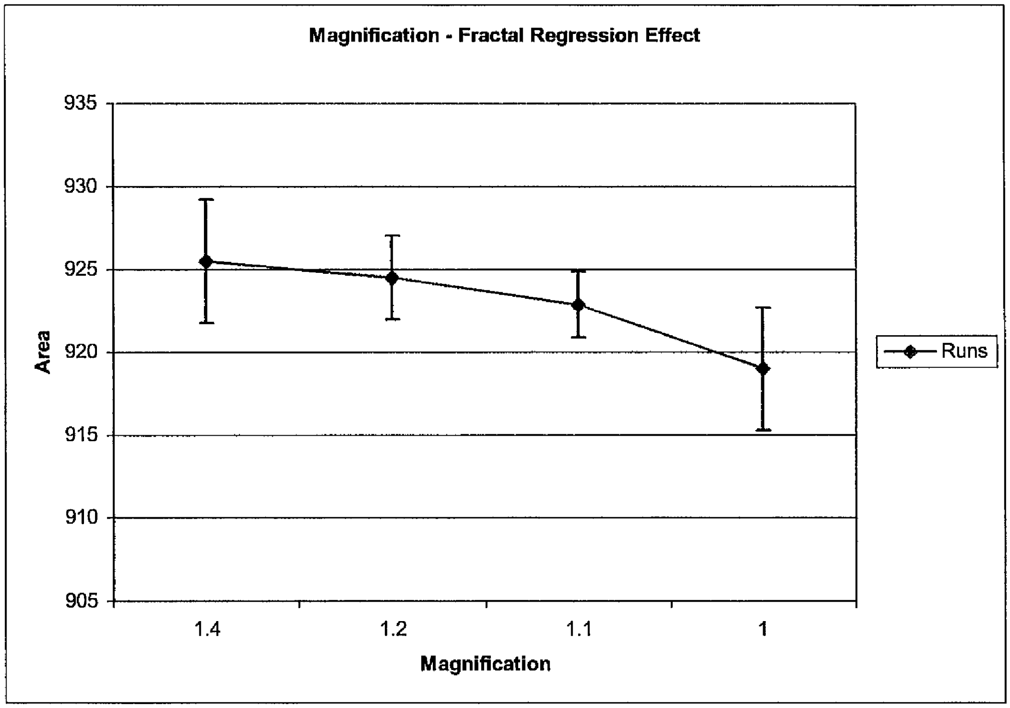

Chart 2. Regression of measured area with reducing magnification.

Femoral head

The results of the femoral head computerised image analysis are summarised (Table 16) to show the means and standard deviations of average absolute area of an intertrabecular space within each zone. A total of five specimens were measured in each group.

Control		**Osteoarthritis**	
Zone 1	0.80 ± 0.39	Zone 1	0.37 ± 0.13
Zone 2	0.57 ± 0.16	Zone 2	0.30 ± 0.05
Zone 3	0.61 ± 0.12	Zone 3	0.43 ± 0.18
Zone 4	0.59 ± 0.21	Zone 4	0.66 ± 0.18

Table 16. Means and standard deviations of the average absolute areas of profiles of intertrabecular spaces (mm^2). n = 5.

The results were examined by analysis of variance. A significant difference was detected:

$p < 0.05$; $F = 3.75$; $df = 39$.

Multiple range tests showed that the difference lay between the osteoarthritic femoral heads and the controls, rather than between the zones.

The average intertrabecular spaces were generally smaller in the osteoarthritic specimens.

There was no statistical difference in the data for the zones on either side of the epiphysial line.

Femoral neck

Cortex

The image analysis system measured the total area (mm^2) of cortical bone in each specimen. A Student's t-test showed no significant differences between the values obtained:

Osteoarthritic specimens - 126.0 ± 31.5

Control specimens - 94.5 ± 28.9

The area of each of the 12 cortical sectors (Fig. 29, page 67) was measured in a sequential order. This was done for the osteoarthritic and control specimens and the results subjected to a one-way analysis of variance. This showed significant differences:

$p < 0.01$; $F = 3.77$; $df = 23$.

Multiple range tests showed that sector 12 (most inferior part of the femoral neck) of the osteoarthritic specimens contained significantly more bone than the corresponding sector of the control specimens. None of the other sectors showed differences which reached a statistical significance.

In control specimens, sectors 7 and 12 contained somewhat more bone than the other sectors. Sector 12 is the most inferior part of the femoral neck, while sector 7 lies in the upper posterior part. In the osteoarthritic femoral necks, the parts of the cortex adjacent to the significantly thicker sector 12, sectors 1 and 2 more anteriorly and sector 11 more posteriorly, also contained more bone than the corresponding sectors of the controls, although the differences did not reach significance. Similarly sector 7 in the osteoarthritic specimens contained more bone than the corresponding sector of the controls. The other sectors were all similar between the two groups. The data indicated that the osteoarthritic specimens contained more bone in the cortex at the inferior part of the neck and suggested that the cortex in the upper posterior part of the neck might also be thicker.

Noting that the inferior sectors of the cortex of the femoral neck seemed generally thickened in the osteoarthritic bones, the sectors were summed to give the amounts of bone in the four quadrants of the section of the femoral neck: anterior (sectors 2, 3, & 4), superior (sectors 5, 6 & 7), posterior (sectors 8, 9 & 10) and inferior (sectors 11, 12 & 1). The values obtained for the quadrants (Table 17) in the osteoarthritic and control specimens were compared with each other by a one-way analysis of variance. The inferior quadrant of the cortex of the femoral neck in the osteoarthritic bones contained significantly more bone than the other quadrants of these specimens or of the controls:

$p < 0.01$; $F = 4.76$; df = 7.

Quadrant	**Control**	**Osteoarthritis**
Anterior	23.22 ± 5.85	26.87 ± 5.40
Superior	21.30 ± 12.06	26.78 ± 16.15
Posterior	19.81 ± 8.88	19.54 ± 2.84
Inferior	30.14 ± 9.88	52.81 ± 18.43

Table 17. Area of cortical bone in anterior, superior, posterior and inferior quadrants of cross sections of femoral neck (mm^2) For each group $n = 5$.

Medulla

The image analysis system measured the total area (mm^2) of trabecular bone in each specimen:

Osteoarthritic specimens	-	**45.3 ± 8.0**
Control specimens	-	**79.3 ± 41.7**

A Student's t-test showed significant difference between the values obtained with the degree of significance being $P<0.05$.

The 25 sectors of the medulla (Fig. 27, page 66) were measured in three groups. The outer and inner group contained 12 sectors and formed an inner and outer ring and a small central zone (sector 25).

Values for the total cross sectional area of trabecular bone in each of the rings and their sum were obtained (Table 18) and compared between the osteoarthritic and control specimens by Student's t-tests but no significant differences were found.

Sectors (rings)	**Control**	**Osteoarthritis**
Outer ring	48.7 ± 22.3	30.4 ± 8.1
Inner ring	28.2 ± 18.6	13.6 ± 6.1
Centre	2.4 ± 1.9	1.3 ± 0.7

Table 18. Total cross sectional area of trabecular bone in rings (mm^2)

In each of the 24 sectors of the outer and inner rings the cross-sectional area of the trabecular bone was measured. The data from each of the 24 sectors (Table 19 & 20) of the osteoarthritic and control specimens were subjected to an analysis of variance. It showed significant differences between the sectors:

df = 239; F = 5.96; p < 0.01.

As expected, it indicated that the larger peripheral regions generally contained more trabecular bone than the smaller deeper regions of the neck. It also showed a general difference between the regions of the osteoarthritic necks and their corresponding control regions.

Outer Ring	**Control**	**Osteoarthritis**
1	5.33 ± 2.70	4.01 ± 1.47
2	4.27 ± 2.08	2.84 ± 0.50
3	3.06 ± 2.01	2.13 ± 0.89
4	3.18 ± 2.02	1.56 ± 0.94
5	3.50 ± 1.76	2.51 ± 0.70
6	4.93 ± 2.33	2.69 ± 1.02
7	4.96 ± 3.23	2.98 ± 2.03
8	3.53 ± 2.89	1.97 ± 0.81
9	3.31 ± 2.07	2.17 ± 1.16
10	3.32 ± 2.10	1.45 ± 0.92
11	3.79 ± 1.36	2.59 ± 1.14
12	5.55 ± 2.17	3.56 ± 0.89

Table 19. Area of trabecular bone in each of the 12 sectors of the outer ring of the medulla (mm^2) For each group n = 5.

Inner Ring	**Control**	**Osteoarthritis**
13	3.42 ± 1.78	1.62 ± 0.89
14	2.75 ± 2.07	1.15 ± 0.27
15	2.11 ± 1.49	1.22 ± 0.83
16	1.71 ± 1.29	1.28 ± 0.72
17	2.04 ± 1.32	1.28 ± 0.57
18	2.29 ± 1.71	1.23 ± 0.57
19	2.29 ± 1.86	1.11 ± 0.43
20	2.05 ± 1.98	0.68 ± 0.57
21	1.96 ± 1.78	0.74 ± 0.29
22	2.09 ± 1.70	0.80 ± 0.36
23	2.32 ± 1.21	1.06 ± 0.66
24	3.10 ± 1.70	1.43 ± 0.79

Table 20. Area of trabecular bone in each of the 12 sectors of the inner ring of the medulla (mm^2) For each group n = 5.

The mean cross sectional area of trabecular bone in every osteoarthritic sector was less than the corresponding control value. Ten of the twenty-four means in osteoarthritis were less than fifty percent of the mean control values. Eight of these ten sectors (sectors 13, 14, 19, 20, 21, 22, 23, 24) lay mostly in the posterior and inferior parts of the inner ring of the medulla. One (sector 4) lay in the upper anterior part of the outer ring and another (sector 10) lay in the lower posterior part of the outer ring.

The amounts of trabecular bone in each region were then summed so that a total amount of trabecular bone for each quadrant, excluding the small central sector, was obtained (Table 21).

Quadrant	**Control**	**Osteoarthritis**
Anterior	12.96 ± 6.55	10.18 ± 3.40
Superior	20.02 ± 11.58	11.80 ± 4.28
Posterior	16.26 ± 11.84	7.81 ± 3.58
Inferior	23.50 ± 9.61	14.26 ± 3.75

Table 21. Area of trabecular bone in anterior, superior, posterior and inferior quadrants of cross sections of femoral neck (mm^2) For each group n = 5.

As before the quadrants were anterior, superior, posterior and inferior. Analysis of variance showed a significant difference:

$p < 0.05$; $F = 3.74$; $df = 39$.

Multiple range tests showed that the difference was a general one in which the osteoarthritic femoral necks contained less trabecular bone than the controls. There were no differences between the four quadrants within the controls or the diseased specimens.

Heberden's nodes

The specimens that showed evidence of the disease were categorised as having moderate nodes and severe Heberden's nodes.

The severe node sample was analysed. It consisted of two index, two middle and three little fingers. These specimens were compared to control groups of five index, middle and little fingers.

On the posteroanterior radiographs, the image analysis system calculated the distance from the midline to the most prominent lateral and medial points of the base of the distal phalanx and the head of the middle phalanx and divided the values obtained by the phalanx length. This would take account of the different phalanx sizes.

On the lateral radiographs, the system also measured the distance from the longitudinal axis of the bone to the most prominent dorsal and ventral points of the base of the distal phalanx and the head of the middle phalanx and divided the values obtained by the phalanx length. This would take account of the different phalanx sizes.

The image analysis system used the following variables to calculate the derived measurements:

$$DLEN1 = \frac{LEN1}{CDLAT}, \quad DLEN2 = \frac{LEN2}{CDLAT} \quad \text{(PA view, distal phalanx)}$$

$$DLEN4 = \frac{LEN4}{CMLAT}, \quad DLEN5 = \frac{LEN5}{CMLAT} \quad \text{(PA view, middle phalanx)}$$

$$DLEN7 = \frac{LEN7}{CDLAT}, \quad DLEN8 = \frac{LEN8}{CDLAT} \quad \text{(Lateral view, distal phalanx)}$$

$$DLEN10 = \frac{LEN10}{CMLAT}, \quad DLEN11 = \frac{LEN11}{CMLAT} \quad \text{(Lateral view, middle phalanx)}$$

Severe nodes – The small number of fingers with severe nodes made the use of an analysis of variance test impractical. Evaluations were made by comparing the individual severe node specimens with the means and standard deviations from the corresponding control group. Differences were described as being one, two or three times the standard deviation of the control mean.

The following charts show the control mean and standard deviation and the corresponding severe fingers. The bars are set either side of a mid-line, which represents the actual phalanx midline computed by the image analysis system. The red stars represent the difference from the control mean in number of standard deviations. The x axis is the normalised ratio of the most prominent part of the phalanx (lateral, medial, dorsal, ventral) to the midline (LEN 1-12) divided by the phalanx length (CDLAT, CMLAT), which produced the DLEN ratios (see page 74).

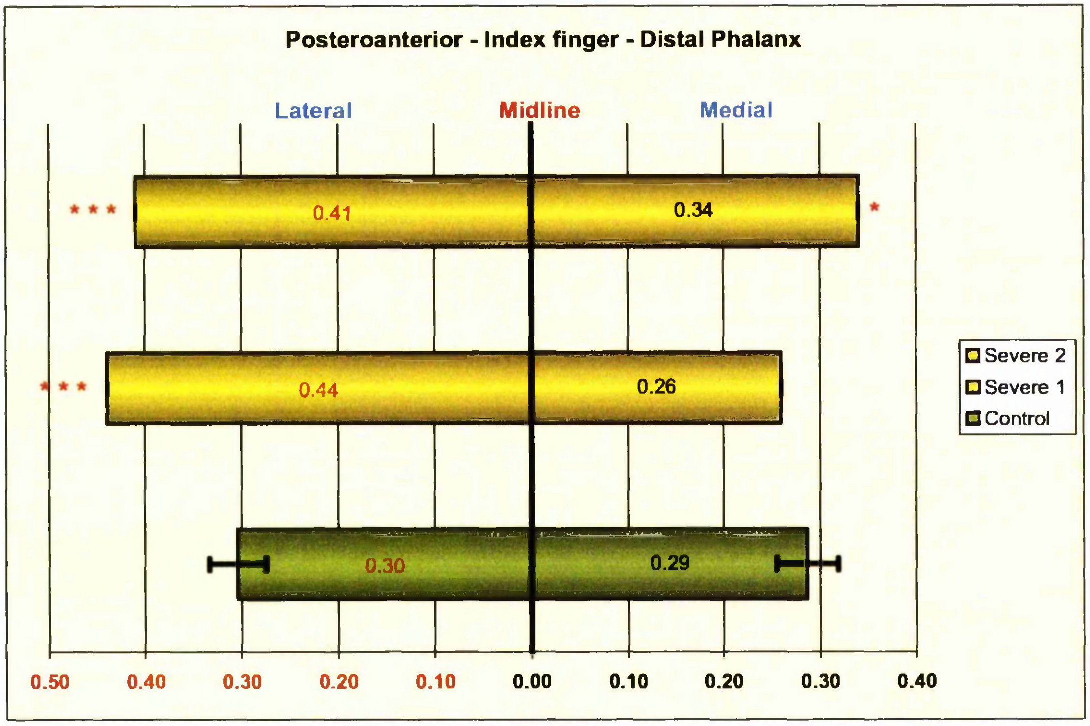

Chart 3. Severe nodes. Posteroanterior - Index finger - Distal Phalanx.

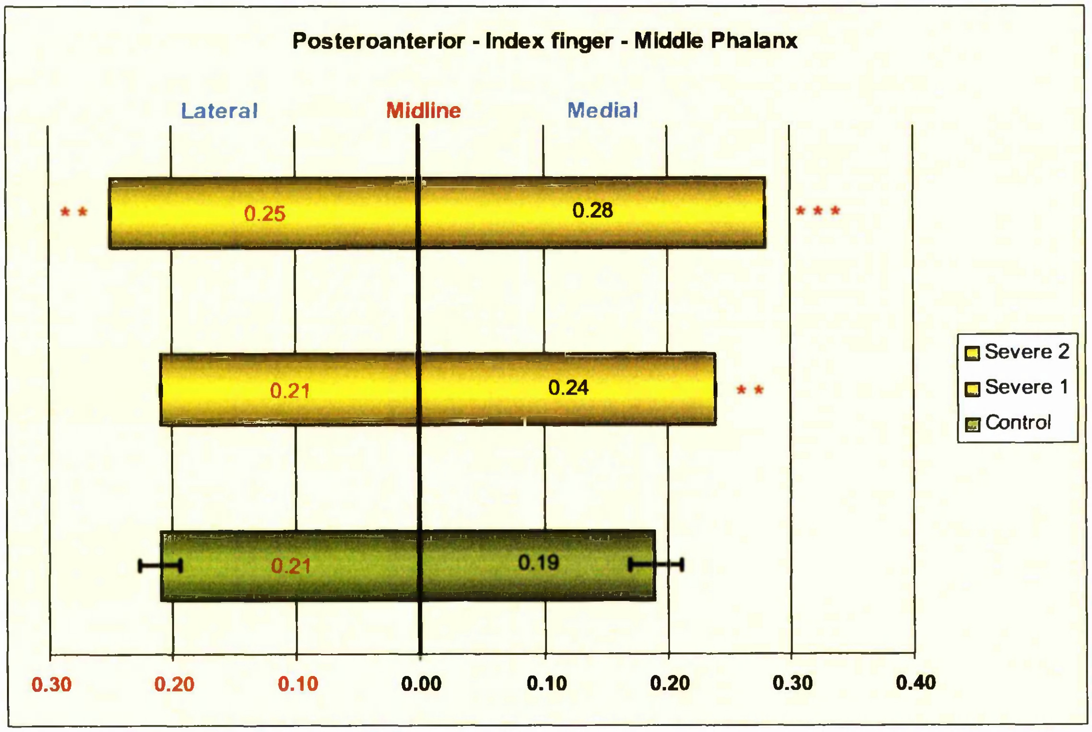

Chart 4. Severe nodes. Posteroanterior - Index finger - Middle Phalanx.

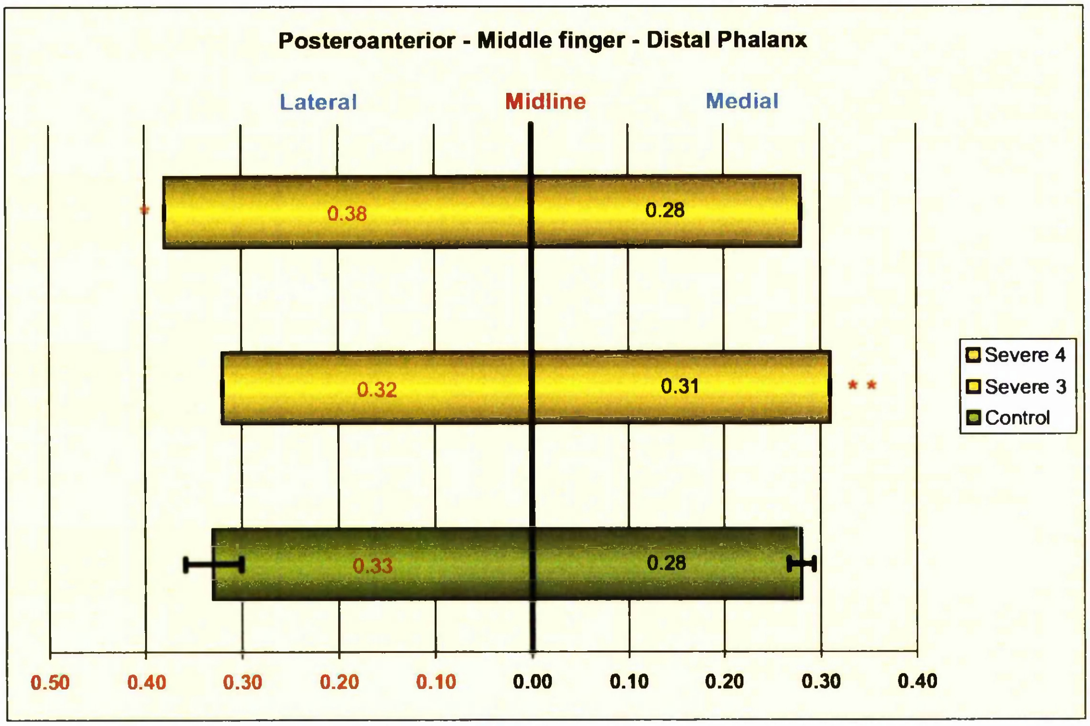

Chart 5. Severe nodes. Posteroanterior - Middle finger - Distal Phalanx.

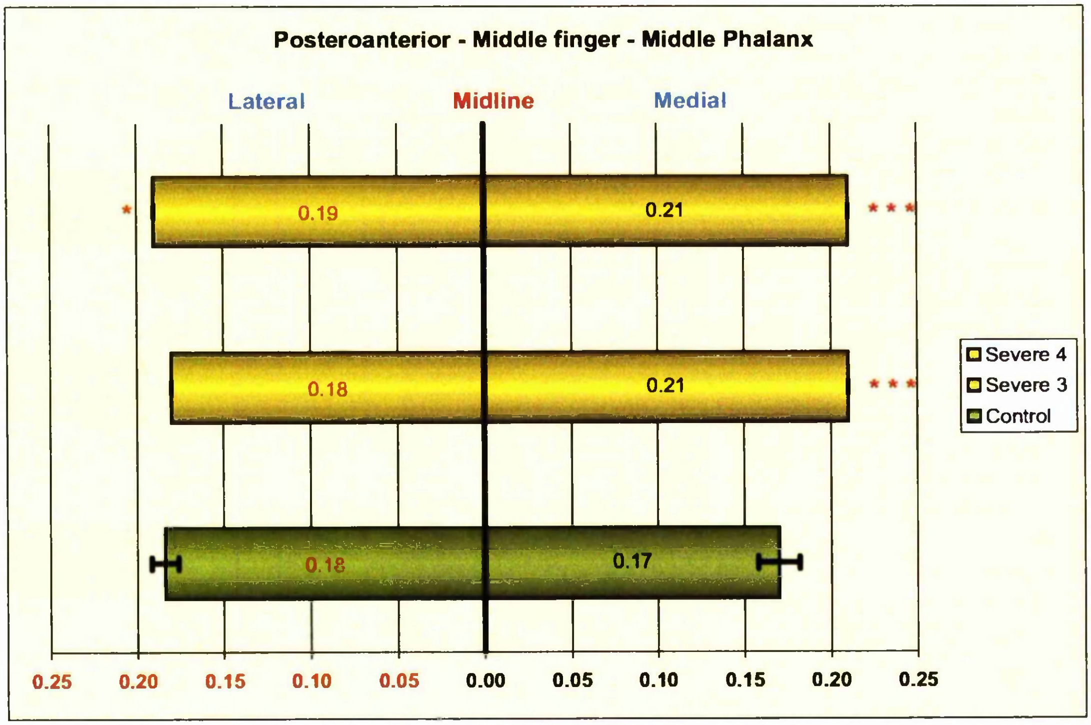

Chart 6. Severe nodes. Posteroanterior - Middle finger - Middle Phalanx.

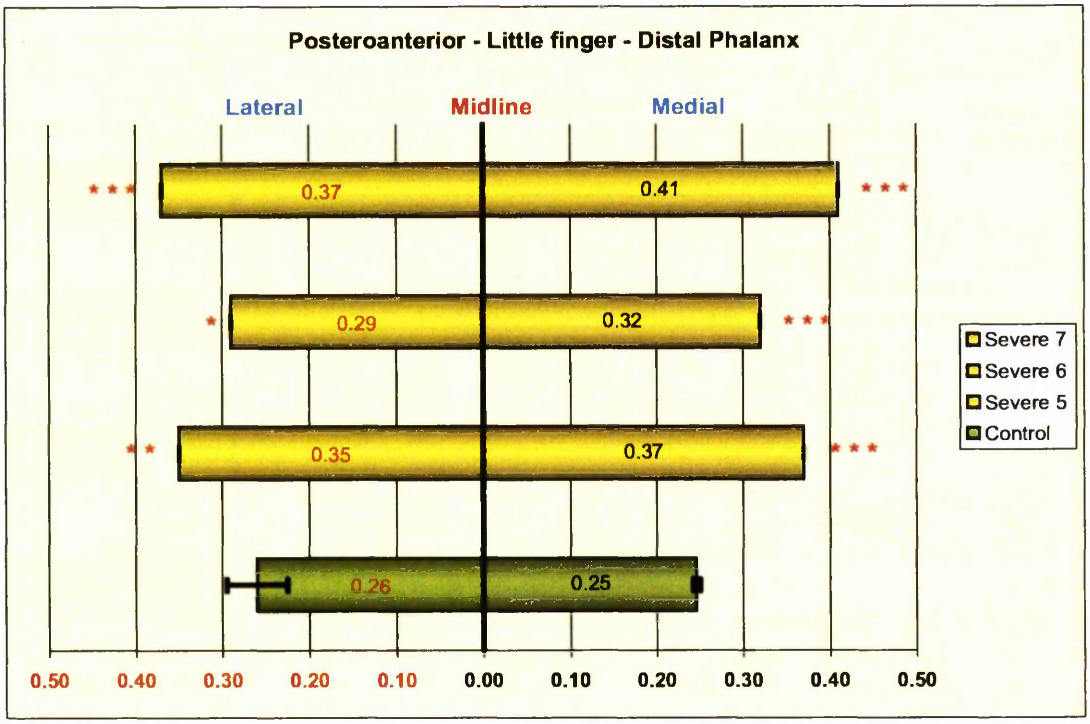

Chart 7. Severe nodes. Posteroanterior - Little finger - Distal Phalanx.

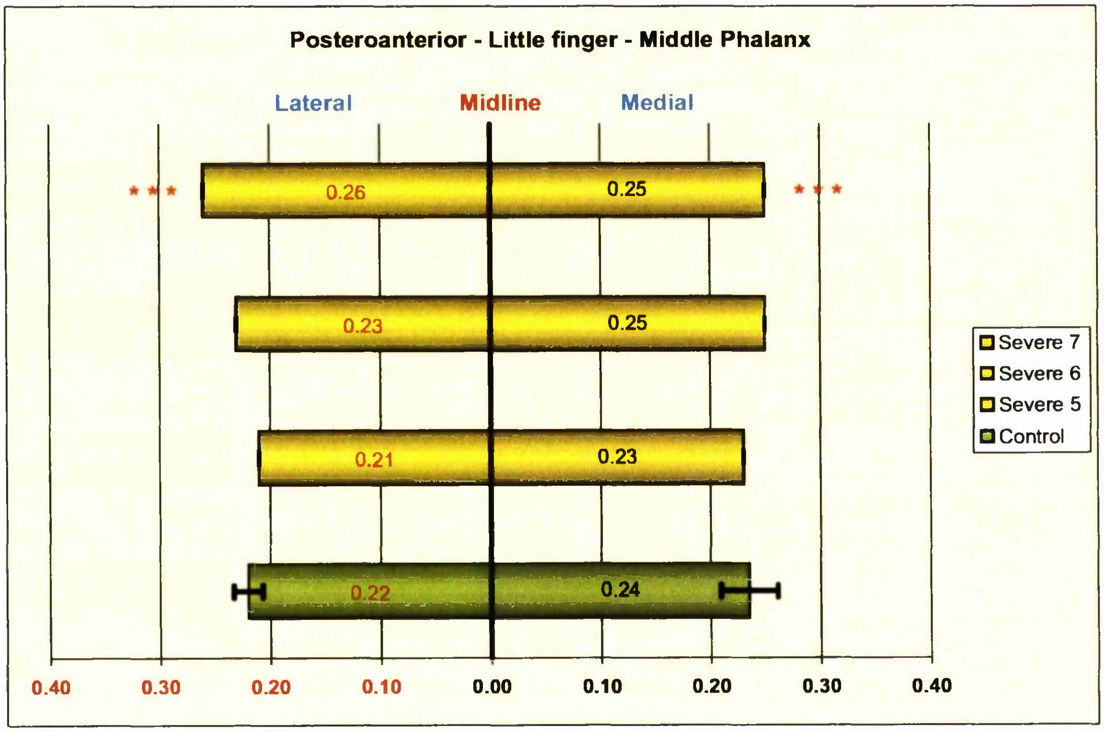

Chart 8. Severe nodes. Posteroanterior - Little finger - Middle Phalanx.

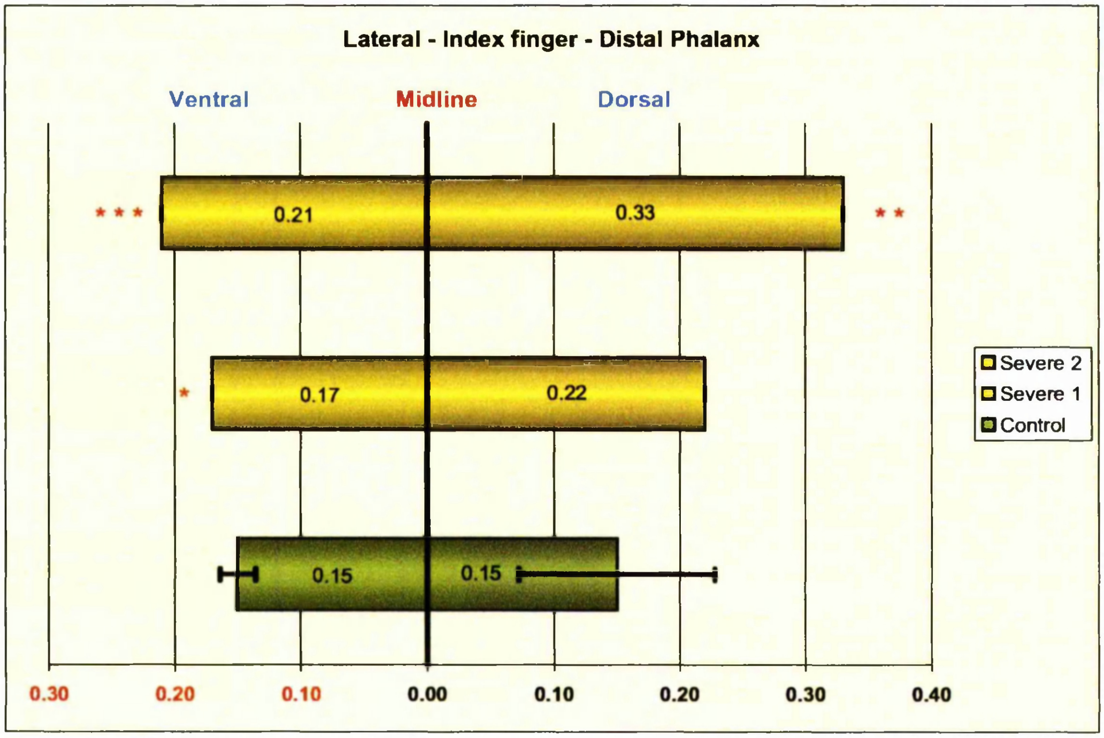

Chart 9. Severe nodes. Lateral - Index finger - Distal Phalanx.

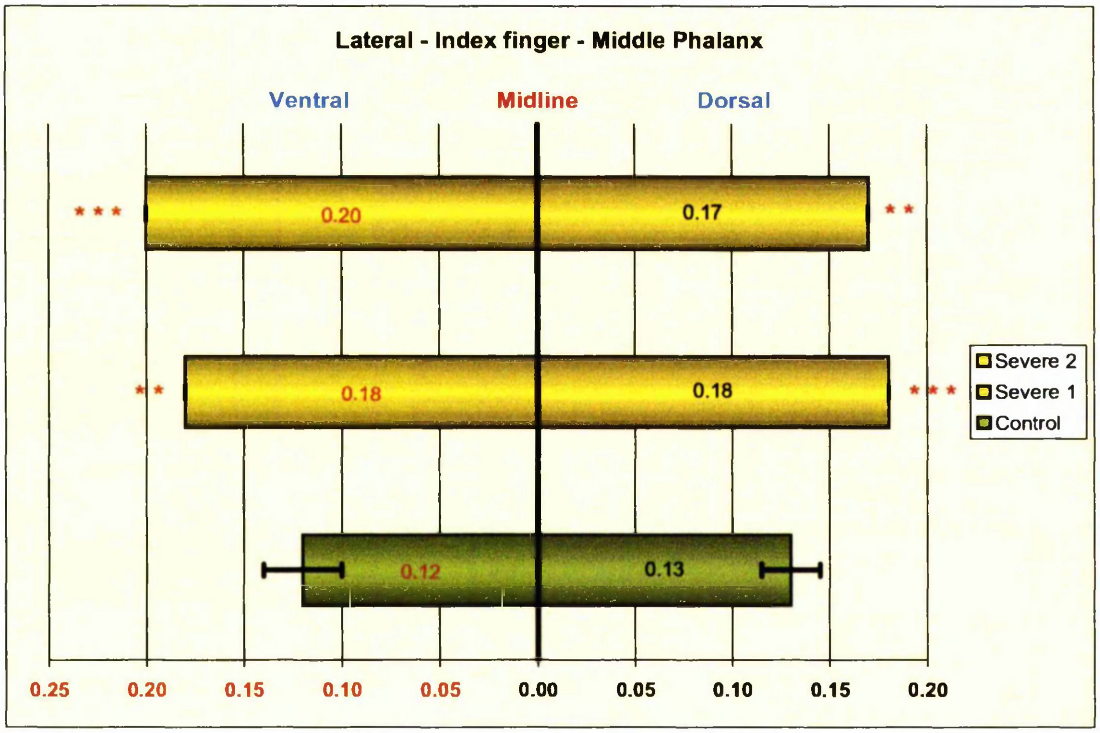

Chart 10. Severe nodes. Lateral - Index finger - Middle Phalanx.

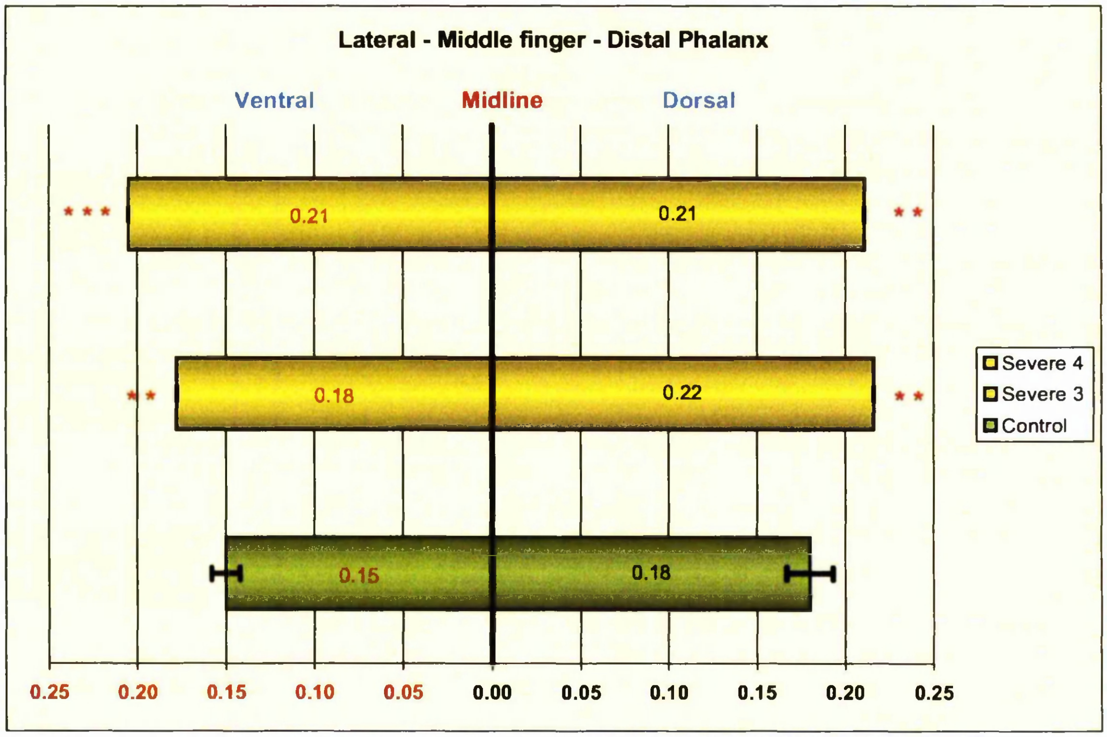

Chart 11. Severe nodes. Lateral - Middle finger - Distal Phalanx.

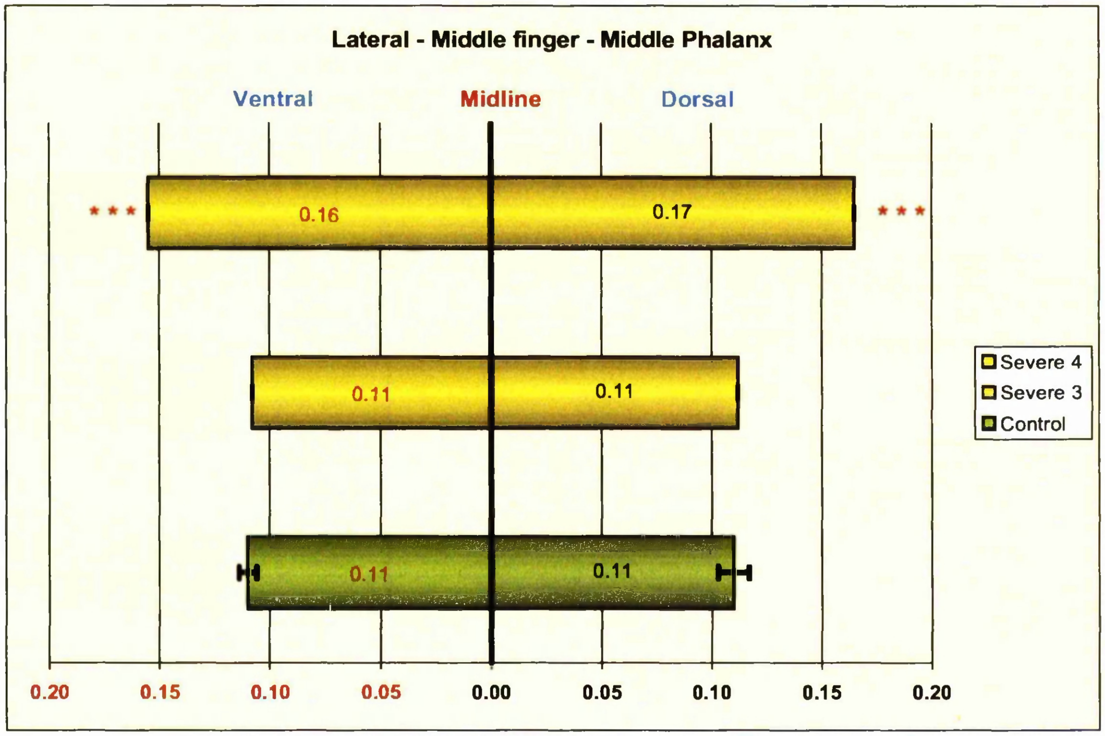

Chart 12. Severe nodes. Lateral - Middle finger - Middle Phalanx.

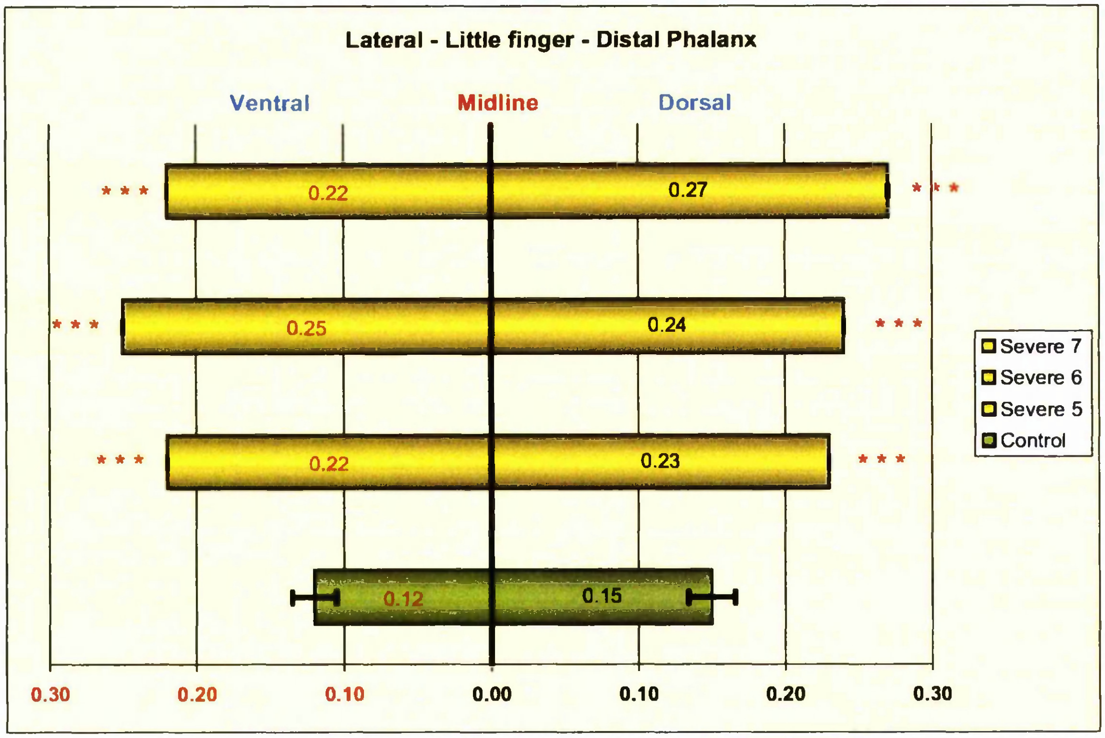

Chart 13. Severe nodes. Lateral - Little finger - Distal Phalanx.

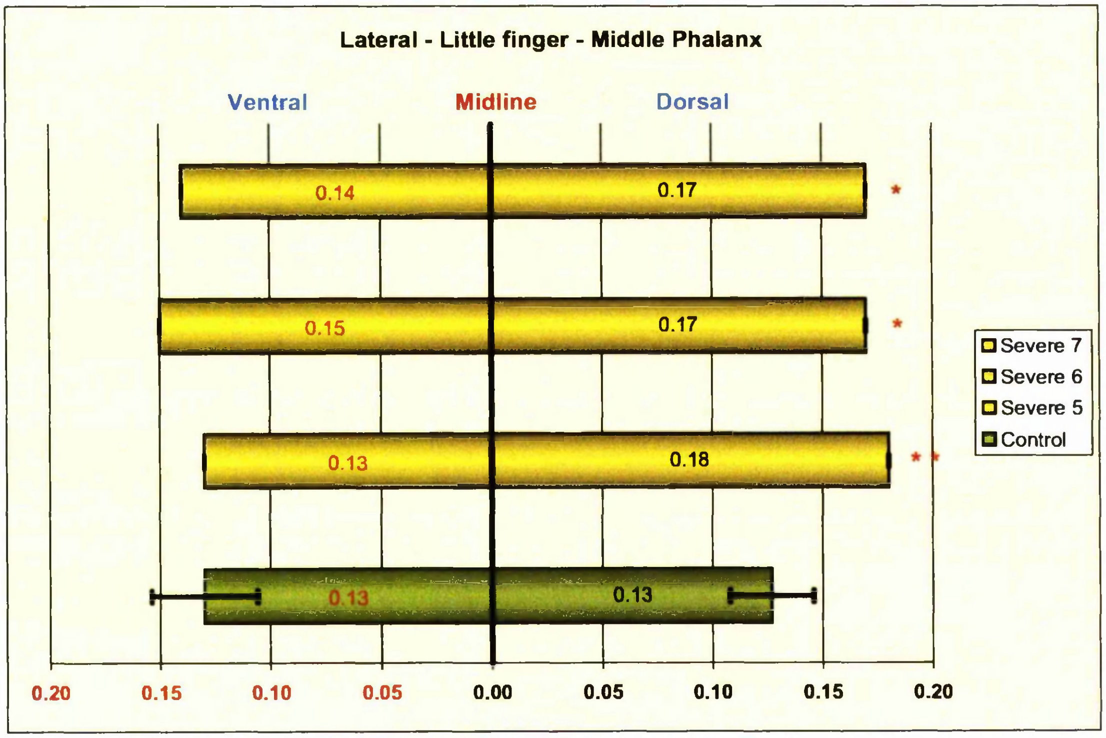

Chart 14. Severe nodes. Lateral - Little finger - Middle Phalanx.

In the posteroanterior radiographs eleven out of the 28 measurements were three or more standard deviations more than the control mean. Four measurements lay beyond two standard deviations of the control mean and a further four lay beyond one standard deviation of the control mean. The remaining nine measurements were less than one standard deviation from the control mean.

In the lateral radiographs twelve out of the 28 measurements were three or more standard deviations more than the control mean. Seven measurements lay beyond two standard deviations of the control mean and a further three lay beyond one standard deviation of the control mean. The remaining six measurements were less from one standard deviation from the control mean.

The measurements indicate that while several phalanges showed bony enlargement on both sides of the midline, a number showed enlargement on one side only suggesting that osteophyte formation in patients with severe Heberden's nodes is a localised rather than generalised phenomenon. The results also indicated the involvement of both phalanges in the disease process in most subjects.

Discussion

Discussion

The aim of this project was to produce image analysis procedures to facilitate the collection of morphometric information from three anatomical sites affected by osteoarthritis. Image analysis procedures were developed to measure the distribution of bone in the femoral head and neck and to measure changes in bone morphometry at the DIP.

The problems associated with creating these procedures and the testing of the image analysis system will be discussed. The problems and potential solutions of attempting to automate the image analysis procedures are reported.

The biological results are preliminary and subsidiary to the main aims of the project, but have been reported to give credence to the image analysis techniques and to demonstrate that the techniques can produce meaningful results when used in real experiments. These data were analysed by another member of the research group. Further analysis of the biological data is required, particularly in the production of normalised data and its statistical analysis. The important biological variable is the individual not the analysis zone which is arbitrary. The relevance of the preliminary biological results will be considered and discussed.

Image analysis

Preparation of specimens

The first stages of image analysis which distinguish any biological structure from its surrounding structures, begin well before the specimen reaches the image analyser. When using histological slides, segmentation of the objects of interest begins with the histological stain. Most image analysis systems will use a form of grey level thresholding to discriminate objects of interest. It is important to ensure that the stain chosen gives high contrast between the object of interest and its surroundings when translated into the grey-scale domain. The difference between shades of red and blue, for example, when converted to a grey-scale can be difficult to determine. Usually the addition of a counter stain only adds to the problems of segmentation in a grey-scale image. The ideal stain would be one that produces a grey phase that is significantly distinct from all other structures within the section (Parkinson & Fazzalari, 1994).

In preparing the femoral neck sections, the goal was to produce histological sections suitable for computerised image analysis. The cortical and trabecular bone had to be stained well enough for the image analysis system to be able to discriminate them from other tissue components. It was found that the use of a modified van Gieson's (1889) stain best achieved this (Appendix D).

The physical size of the tissue blocks caused some technical difficulties, in providing artefact free sections. Tearing and scoring of the sections was common and difficult to avoid. Using a technique, which includes bone decalcification, results in the bone staining less consistently, compared to an undecalcified bone specimen, cut in resin (Mawhinney & Ellis, 1983). The uptake of stain in a resin section results in a far more consistent and even stain which in turn gives much better resolution. This would make any subsequent image processing and segmentation much easier. This process was used by Amir and co-workers (Amir et al, 1992) to carry out a bone distribution study in the femoral head. This would provide a far more accurate specimen for image analysis and would have eliminated the subjective process of manually tracing the inter-trabecular spaces. Unfortunately, it proved impossible to procure the necessary equipment to use this technique.

Whether the specimens are histological sections or X-ray films, the goal is to start off with a specimen that has the best possible contrast.

Image analysis tests

In preparing the femoral neck macro, a series of tests were employed to determine the level of bias that may be introduced from an array of sources. The use of image analysis in biomedical research is increasing and care must be taken to ensure the reliability of the results obtained.

When an experienced operator performs the analysis most of the user-defined operations result in no statistically significant differences in the values obtained between runs. The operation of repeatedly calibrating the image analysis system with an accurate scale has been shown to introduce minimal error and shows no significant difference between runs. An error of less than 0.3% was recorded. The operation of scale calibration must be done with great care and patience as a difference of only a few pixels in the measured length of the scale, can result in a large error in the scale applied.

Over a few hours the sharp focus of CCD camera output when attached to a macro lens or microscope can be lost. This would necessitate the user to re-focus the system. Focusing a specimen on a VDU screen has been shown in this study to introduce a statistically significant error in measured area. An error of less than 0.4% was recorded. This difference is attributed to variance within each of the test runs, rather than between runs, suggesting that it is inherent and unavoidable. This error could be reduced with the use of a higher resolution CCD camera and matched with a higher resolution display screen. Again, this result emphasises the need for rigorous care when setting the focus on a specimen.

When comparing the intra observer thresholding tests for both cortical and trabecular bone, no statistically significant error is seen. This result is seen in both the expert and non-expert tests. This suggests that users settle on their own thresholding protocol and stick to it. An error of less than 3% was recorded for the expert user and between 2 - 8% for the non-expert operators.

When inter observer thresholding is examined a much higher level of difference is observed, with differences being seen up to 21%. The differences were noted between expert and non-expert users. The one-way analysis of variance statistical tests showed a significant difference, between users. This suggests that bone thresholding, is best carried out by the same experienced operator. This presents a problem when comparing results from different laboratories or when the operator must change. The only solution to this is that the operating protocols used should be well defined and careful quality control procedures implemented i.e. the use of a stored control sample to train new operators (Parkinson & Fazzalari, 1994). New or inexperienced operators have been shown to exhibit a learning effect, when measuring bone parameters, getting less and less variation in their measurements as they measure more and more specimens (Delling et al, 1980).

Most studies that have investigated Mandelbrot's (1967) "Coastline of Britain" effect (the smaller the measuring step used results in an increased measured perimeter) on the perimeter length of biological specimens have compared measurements taken at different objective lens magnifications on a microscope. The difference in the microscope objective magnifications is large and produces a significant difference in measured perimeter. This study did not use a microscope to acquire the images but a macro lens fitted directly on the camera. The levels of magnification used in the experiment, was up to a magnitude of 1.25 times. This difference in magnification, as expected, was so small that no significant difference between the three magnifications tested, was seen, but a linear regression effect was noted and supported the hypothesis that a decreased magnification (increase in step-size) results in a lower measured perimeter. A further test determined the magnification difference that would result in the regression becoming statistically significant. This occurred at 1.4 times magnification. The reason for the measured area exhibiting the same phenomena as measured perimeter, albeit less extreme, lies in the way in which the Vidas system measures area. The Vidas system measures area using a pixel counting method. This means that the measurement will be affected by magnification - as is the case with any 'pixel' based system. It may be the pixel effect on the digital representation of a biological structure, in a digital image analysis system that exhibits this fractal problem. This must not be confused with actual shape of the biological structure, as showing a fractal dimension, which some workers have mistakenly reported. When determining whether a biological object has a fractal index or not the object must be examined at a low enough magnification to measure the objects perimeter shape, not the stepped pixel edge of the digital image.

The changes in magnification in the head macro were less than 1.4 times. Any fractal effects on the measurements would not be significant.

It is accepted that it is difficult to produce results, when analysing bone morphometry, which can be directly compared to other workers results. The differences in the methods that are employed in different bone laboratories make these comparisons difficult. It has been suggested that exactly the same protocols (Delling et al, 1980), and nomenclature (Parfitt et al, 1987) be agreed and used universally, even down to the magnification used (Parkinson & Fazzalari, 1994), but these ideas can only be implemented in part as the protocols used in any particular experiment will be determined by the needs of that experiment.

Bone and image analysis

Computers are playing an increasingly important role in biomedical science research. As the affordable power increases year after year we should be looking at new ways in how we can utilise this computing power.

With the increase in computing power comes the ability to fully utilise known techniques. In this study a fully automated method, using dilation followed by binary thinning to determine the outside mask of the section was developed and tried, but was discarded in favour of manual drawing because of the time taken (15 minutes) by the system to do the necessary processing. Binary thinning is a particularly CPU intensive operation as it erodes the object with a chosen kernel whilst keeping the end-points of the object intact. When the same technique was tried on a recently acquired new computer system the operation took less than one second, rendering the technique usable. N.B. The new system could not be readily used to perform the measurements in this project as it uses a different macro scripting language from the VIDAS.

Bone is a complex three-dimensional structure. Many of the existing techniques, used to measure bone, utilise methods that measure structures in two-dimensions and then derive three-dimensional estimates from the values obtained. The advent of machines, such as the X-ray tomographic microscope (Micro-CT machines) makes the collection of data in three-dimensions a reality. Modern high-powered computers, such as the Silicon Graphics ONYX 3200, have no problem in visualising these large datasets. They make it possible to view these reconstructed datasets in visualisation caves (virtual environment laboratory (VEL)), which enable the operator to be fully immersed with the model and even able to manipulate and zoom in and out of the structures. The main problem with analysing three-dimensional datasets is that there are few tools or methods for extracting measurements in three-dimensional space. If we are to move forward in this three-dimensional virtual world, more research is required to develop techniques in three-dimensional morphometry and new visualisation tools.

Femoral head and neck

One of the main aims of this project was to create an image analysis programme to measure and analyse the distribution of bone in the human femoral neck and head. Deciding on the protocols to be used in quantifying the distribution of any definable structures within a biological specimen can be difficult, as there are many different methods which could be applied. A histological section of the femoral neck is a closed structure, cortical bone encompassing the inner trabecular bone. Deciding to measure this structure, as a whole image analysis object, has advantages and disadvantages. The relatively low magnification, required to capture the complete section, results in low resolution which can lead to measurements that are not as accurate as measurements made at a high magnification. Although this is true, the magnification used in the experiment, was high enough to deliver an acceptable accuracy in the measurements made. The idea of measuring the complete section enabled a distribution protocol to be constructed that could easily be understood and interpreted. Given that the total cortical bone measured did not show a significant difference between the osteoarthritic and control specimens and that the total trabecular bone measured showed a vast decrease in the osteoarthritic specimens, it would be reasonable to further examine the specimens to determine whether any local differences were apparent. Dividing the cortical bone into 12 sectors and dividing the medullary bone into 25 sectors results in a fairly detailed representation of the bone distribution. The choice of using a radial-type solution to create the sectors was primarily made because of the shape of the specimen. The specimen is a circular shape and the application of a box or grid system would not have been as accurate as the boxes would overlap at the edges. It would also have been more difficult to compare sectors, as placement of the grid would have been critical. The radial approach ensured that each specimen would have the same number of sectors. Although the sectors were not of identical size the same criteria for sector creation was carried out on each specimen. Given that the specimens were carefully oriented, before image grabbing, the sectors would equate to the same percentage area in each specimen. The number of sectors chosen could be deemed as excessive, but as the computer performed the operations to divide the bone into these sectors, this did not translate into an extra burden for the operator. Also, when starting with a large number of distribution sectors it is possible, as was done in this study, to add the data from a number of sectors into larger sectors. This of course cannot be done in reverse.

The methods used to map the distribution of bone in the femoral head and neck has enabled this study to document a number of differences in the bone architecture of osteoarthritic subjects when compared to subjects with no history of arthritic disease. The loss of intertrabecular space, reflecting thickening that was observed in the trabeculae of the osteoarthritic femoral head specimens, was consistent with the compressive forces conveyed from the articular surface to the neck of the femur. These compressive trabeculae converge on the cortex at the inferior part of the neck, a region clinicians refer to as the *fulcrum*. In this study, measurements of the cortical bone has shown that this *fulcrum* area was thicker in the osteoarthritic than in the control femoral necks.

The inferior region of the femoral head, generally referred to as the non-weight bearing region, showed less trabecular bone in the osteoarthritic specimens and resulted in substantially more intertrabecular space. Trabecular bone was also seen to be reduced in the medulla of the neck.

This study suggests that osteoarthritis results in an increase in the amount of bone within those parts of the proximal femur principally responsible for the transmission of weight and a loss of bone in other areas.

The femoral head macro did not measure the tissue area in which the trabecular tracings were made. The technique should be improved as to allow for these tissue area measurements. This would allow for the production of normalised data.

Other workers have reported increased amounts of bone or thickening of compressive trabeculae in the weight bearing subchondral regions of osteoarthritic femoral heads (Oettmeier & Abendroth, 1989; Crane *et al.*, 1990; Fazzalari *et al.*, 1992; Grynpas *et al.*, 1992). The study by Fazzalari *et al.* (1992) also reported reduced bone in the non-weight bearing region. The present study is the first to correlate architectural changes in the osteoarthritic femoral head with architectural changes in the femoral neck of specimens obtained from the same subject.

Heberden's nodes

The image analysis macro was designed to determine a midline through the distal and middle phalanges in the posteroanterior plane radiographs and calculate the Feret diameters. It also calculated the Feret diameters from a manually determined midline on the lateral plane radiographs. These techniques would have to be consistent, reliable and repeatable for all specimens. No problems were found in these aspects whilst executing the macro. The main difficulty with this image analysis macro, was the problem of segmentation. Standard radiographs are particularly difficult to threshold to a binary image due to the shadowing effect and varying levels of contrast from one specimen to the next. A standard radiograph of the DIP joint is a two-dimensional representation of a complex three-dimensional structure comprising of bone, cartilage and synovial membrane (Dacre and Huskisson, 1989). These elements contribute to the difficulty in defining bony edges in the fairly "soft" radiographic images in this study. This was over-come by slightly under thresholding the image and manually connecting any gaps. This is time consuming and tedious for the operator, but did result in an acceptable binary representation of the radiograph. It has been demonstrated that using digital images of radiographs with a lower number of grey scales i.e. using 5 bit images, results in less accurate analysis (Wenzel A, 1987). The system used in this study uses 8-bit, 256 grey scale resolution image processing. It is generally accepted that the dynamic range of a standard X-ray picture is around the equivalence of a 10-bit digital image (Barber DC, 1983). Modern image analysis systems are now starting to include the power to process up to 14-bit images. This will facilitate imaging operations on images such as standard radiographs, which have a high dynamic range.

The image analysis suggests that some of the phalanges had enlarged on one side only while others had enlarged on both sides. This was true of both the middle and distal phalanges. Although numbers were small, the lateral and medial sides seemed equally affected at the distal phalanx. In the middle phalanx, the osteophytes seemed to lie more commonly on the medial side.

The side of the joint found to be enlarged on general reporting of the radiographs and using image analysis usually, but not always, corresponded with the side on which the largest Heberden's nodes were found. The exceptions may have come about through deformity masking larger osteophytes or exaggerating smaller ones. In one specimen, the posteroanterior radiograph revealed that a degree of subluxation of a joint caused a seemingly non-deformed region of the head of the middle phalanx to be unduly prominent and likely to explain the clinical recognition of a Heberden's node on the side opposite from the main seat of the pathology. In this same specimen, a bony fragment lay on the posterior aspect of the joint and was not included in the measurements. It was readily seen in the lateral view. In another specimen, the bones were generally large and had rounded bony projections on one side of the joint but little joint space narrowing or other evidence of osteoarthritis. In this specimen, from a male subject, clinical examination had classed the finger as having a severe Heberden's node on the medial aspect and image analysis had suggested enlargement localised to this region.

Lateral plane calliper measurements, produced by a previous study carried out in the Laboratory of Human Anatomy, did not correlate well with the image analysis lateral radiograph measurements. This could relate to the interpretation of the radiographs. The image analysis lateral results are therefore tentative and are pending further investigation.

Hart *et al.* (1994) in a large study reported correlation between clinical and radiological assessment of interphalangeal joint disease to be far from perfect. Although, in their large study, they found a general relationship between clinical and radiological gradings, they had several instances in which high radiological scores were given to patients who were given zero for the clinical grade and vice versa. Clearly bony changes may have to be quite gross to become visible or palpable. Some of their subjects with a high clinical but low radiological score may have been due to the use of anterior -posterior radiographs only. One of the middle fingers in this study, assessed as having a severe Heberden's node seemed to have only early osteoarthritis. This study agrees with Hart *et al.*(1994) that radiology is probably more reliable than clinical assessment in diagnosing osteoarthritis at the distal interphalangeal joint.

The study shows that specimens with severe Heberden's nodes exhibited substantial enlargement on both distal and middle phalanges. The computerised image analysis suggests that Heberden's nodes occur as a result of *localised* bony changes in both middle and distal phalanges.

Future work

The image analysis macros could be re-written to run on a newer faster computer. With additional processing power the use of processor intensive techniques such as binary thinning could be employed. This could be applied to automatically create the medulla mask. This would further help the automation of the technique.

The femoral neck technique of creating radial sectors could be modified and utilised on any varying circular type of structure.

An obvious advance would be to secure funding to allow for the production of methylmethacrylate sections. This would eliminate the need to decalcify specimens, which would benefit the contrast possible in the histological staining.

An investigation into osteophyte formation in trigger toe has just begun with the group. The Heberden's nodes macro could be modified to measure osteophyte formation in this new anatomical region.

With the availability of super computers such as the Silicon Graphics Onyx 3200 (512 CPUs), now becoming accessible to large biomedical institutions the possibility of studying large multidimensional datasets is almost upon us. This would enable the morphological study of very large volumes, only restricted by the limits of the data acquisition machine. Real-time or time-lapse datasets could be studied in virtual reality rooms.

Conclusion

Conclusion

The techniques used in the preparation of specimens should reflect the fact that they will be analysed with an image analyser. In particular, bone specimens should ideally be un-decalcified and cut in resin. Staining should provide high contrast between the structure to be examined and its surroundings.

The highest possible resolution, in both CCD camera and VDU should be implemented. This will minimise error introduced by scaling and focusing.

Most of the operator error is produced by differences in the manually chosen thresholding limits. Although intra-operator error is acceptable, the error revealed by comparing the differences between operators is not. The same operator should do all thresholding. Operators should be well trained and follow well defined operator protocols.

Magnification should not be changed during an experiment, or at least never more than times 1.4 in magnitude.

Image analysis macros can be developed to provide reliable and reproducible parameters of bone distribution.

Research is required to develop and investigate new methods to visualise bone in three-dimensions and to develop new three-dimensional morphometric measuring tools.

Areas of the femoral head, which are involved in weight transmission, exhibited a decrease in intertrabecular space.

Image analysis of the osteoarthritic femoral necks show that the cortical bone thickens at the inferior aspect. This region is important in weight transmission. The trabecular bone in osteoarthritic femoral necks showed a decrease in sectioned area. This suggests an imbalance in the normal remodelling processes.

Osteoarthritis appears to result in an increase in the amount of bone within those parts of the proximal femur principally responsible for the transmission of weight and a loss of bone in other areas.

A better understanding of the remodelling mechanisms in the OA human hip may help to determine the contributing factors in the pathogenesis of OA.

Heberden's nodes occur as a result of *localised* bony changes in both middle and distal phalanges.

References

References

Aaron JE., Johnstone DR., Kanis JA., Oakley BA., O'Higgens P., Paxton SK. (1992). An automated method for the analysis of trabecular bone structure. *Computers and Biomedical Research.* **25**, 1-16.

Acheson RM., Chan Y., Clemett AR. (1970) New Haven survey of joint diseases XII: Distribution and symptoms of osteoarthrosis in the hands with reference to handedness. *Annals of the Rheumatic Diseases* **29**, 275-285

Altman RD., Asch E., Block D. (1986). Development of criteria for the classification and reporting of osteoarthritis. *Arthritis and Rheumatism* **29**, 1039-1049.

Altman RD., Fries JF., Bloch DA., Carstens J., Cooke TD., Groften P., Groth H., McShane Dj., Murphy WA., Sharp JT., Spitz P., Williams CA., Wolfe F. (1978) Radiographic assessment of progression in osteoarthritis. *Arthritis and Rheumatism* **30**, 1214-1225.

Ampe J., Dequeker J., Gevers G. (1986). Regional variation of bone matrix components in osteoarthrotic and normal femoral heads. *Clinical Rheumatology,* **5**, 225-230.

Amir G., Pirie CJ., Rashad S., Revell PA. (1992). Remodelling of subchondral bone in osteoarthritis: a histomorphometric study. *Journal of Clinical Pathology.* **45**, 990-992.

Barber DC. (1983). The computer and the medical images. *British Medical Journal.* **287**, 413-417.

Bollet AJ., Handy JR., Sturgill BC. (1963). Chondroitin sulphate concentration and protein-polysaccharide composition of articular cartilage in osteoarthritis. *Journal of Clinical Investigation.* **42**, 853-859.

Boyde A., Jones SJ. (1996). Scanning electron microscopy of bone: Instrument, specimen, and issues. *Microscopy Research and Technique.* **33**, 92-120.

Boyde A., Elliot JC., jones SJ. (1993). Stereology and histogram analysis of backscattered electron images: age changes in bone. *Bone.* **14**, 205-210.

Buckland-Wright JC. (1989). A new high-definition X-ray unit. *British Journal of Radiology.* **62**, 201-208.

Buckland-Wright JC., MacFarlane DG., Lynch JA., Clark B. (1990). Quantitative microfocal radiographic assessment of the progression in osteoarthritis of the hand. *Arthritis and Rheumatism.* **33**, 57-65.

Buckland-Wright JC., MacFarlane DG., Lynch JA. (1991). Osteophytes in the osteoarthritic hand: their incidence, size, distribution and progression. *Annals of the Rheumatic Diseases.* **50**, 627-630.

Buckland-Wright JC. (1994). Quantitative radiography of osteoarthritis. *Annals of the Rheumatic Diseases.* **53**, 268-275.

Chow CK., Kaneko T. (1972). Automatic boundary detection of the left ventricle from cineangiograms. *Computers and Biomedical Research,* **5**,388-410.

Crane GJ., Fazzalari NL., Parkinson IH., Vernon-Roberts B. (1990). Age-related changes in femoral trabecular bone in arthrosis. *Acta Orthopaedica. Scandinavia.* **61**, 421-425.

Compston JE. (1994). Connectivity of cancellous bone: Assesment and mechanical implications. *Bone* **15**, 463-466.

Cooper C., Cook PL., Osmond C., Fisher L., Cawley MI. (1991). Osteoarthritis of the hip and osteoporosis of the proximal femur. *Annals of the Rheumatic Diseases.* **50**, 540- 542

Corvol M. (2000). The chondrocyte: from cell aging to osteoarthritis. *Joint Bone Spine 2000,* **68**, 557-60.

Cross SS., Rogers S., Silcocks PB., Cotton DWK. (1993). Trabecular bone does not have a fractal structure on light microscope examination. *Journal of Pathology* **170**, 311-313.

Croucher PI., Garrahan NJ., Compston JE. (1994). Structural mechanisms of trabecular bone loss in primary osteoporosis: specific disease mechanism or early ageing? *Bone and Mineral.* **25**, 111-121.

Dacre JE., Huskisson EC. (1989). The automatic assessment of knee radiographs in osteoarthritis using digital image analysis. *British Journal of Rheumatology.* **28**, 506-510.

Delesse MA. (1847). Mechanical processes to determine the composition of rock. *C.R. Academic Science Paris.* **25**, 544-545.

Delling G., Luehmann H., Baron R., Mathews CHE., Olah A. (1980). Investigation of Intra- and Inter-Reader Reproducibility. *Bone Histomorphometry – Third International Workshop.* 419-427.

Desai MM., Zhang P., Hennessy CH. (1999). Surveillance for morbidity and mortality among older adults--United States, 1995-1996. *Morbidity and Mortality Weekly Reports CDC Surveillance Summaries.* **48(SS08)**, 7-25.

Dieppe PA., Huskisson EC., Crocker PR., Willoughby DA. (1976). Apatite deposition disease. A new arthropathy. *Lancet* **1**, 266-269.

Edmonston SJ., Breidahl WH., Singer KP., Day RE., Price RI. (1994). Segmental trends in cancellous bone structure in the thoracolumber spine: Histological and radiological comparisons. *Australasian Radiology.* **38**, 272-277.

Ewers BJ., Dvoracek-Driksna D., Orth MW., Haut RC. (2001). The extent of matrix damage and chondrocyte death in mechanically traumatised articular cartilage explants depends on rate of loading. *Journal of Orthopaedic Research.* **19**, 779-784.

Farkas T.,Boyd RD., Schaffler MB., Radin EL., Burr DB. (1987). Early vascular changes in rabbit subchondral bone after repetitive impulsive loading. *Clinical Orthopaedics and Related Research,* **219**, 259-67.

Fazzalari NL. (1980). An automatic quantitative image analysing computer. *Australian Physical and Engineering Sciences in Medicine.* **3-4**, 193-198.

Fazzalari NL., Vernon-Roberts B., Manthey B., Parkinson I.H. (1990). Relationships between changes in articular cartilage and bone in the femoral head in osteoarthritis of the hip. *Journal of Orthopaedic Rheumatology.* **3**, 144-169.

Fazzalari NL., Moore RJ., Manthey BA., Vernon-Roberts B. (1992). Comparative study of iliac crest and subchondral femoral bone in osteoarthritic patients. *Bone.* **13**, 331-335.

Felson D. (1993). The course of osteoarthritis and factors that affect it. *Rheum Dis Clin N Amer.* **19**, 607-615.

Felson DT., Zhang Y. (1998). An update on the epidemiology of knee and hip osteoarthritis with a view to prevention. *Arthritis and Rheumatism.* **41**, 1343-1355.

Feret LR. (1931). The size of the grains. *International association for properties in materials,* Zurich. **2**, GroupD.

Flautre B., Hardouin P. (1994). Microradiographic aspect on iliac bone tissue in postmenopausal women with and without vertebral crush fractures. *Bone* **15**, 477-481.

Garrahan NJ., Mellish RWE., Compston JE. (1986). A new method for the two-dimensional analysis of bone structure in human iliac biopsies. *Journal of Microscopy.* **142**, 341-349.

Gannon FH., Sokoloff L. (1999) Histomorphometry of the aging human patella: histologic criteria and controls. *Osteoarthritis Cartilage*, **7**, 173-181.

Goldstein SA., Goulet R., McCubbrey D. (1993). Measurement and significance of three-dimensional architecture to the mechanical integrity of trabecular bone. *Calcified Tissue International.* **53**, S127-S133.

Grotz WH., Mundinger FA., Gugel B., Exner V., Kirste G., Schollmeyer PJ. (1994). Bone fracture & osteodensitometry with Dual Energy x-ray Absorptiometry in kidney transplant recipients. *Transplantation.* **58**, 912-915

Grynpas MD., Alpert B., Katz I., Lieberman I., Pritzker KPH. (1991) Subchondral bone in osteoarthritis. *Calcified Tissue International.* **49**, 20-26.

Hadler NM., Gillings DB., Imbus HR., Levitin PM., Makuc D., Utsinger PD., Yount WJ., Slusser D., Moskovitz N. (1978). Hand structure and function in an industrial setting. *Arthritis and Rheumatism* **21**, 210-220.

Hahn M., Vogel M., Pompesius-Kempa M., Delling G. (1992). Trabecular bone pattern factor. A new parameter for simple quantification of bone microarchitecture. *Bone.* **13**, 327-330.

Hart DJ., Mootoosamy I., Doyle DV., Spector TD. (1994). The relationship between *osteoarthritis* and *osteoporosis* in the general population: the Chingford Study. *Annals of the Rheumatic Diseases.* **53**, 158-162.

Heberden, W. (1803). "Commentries on the History and Cure of Diseases. 2nd Edition *Payne, London.* 148.

Hough A. (1983). Variants of osteoarthritis – a pathological overview. *Journal of Rheumatology.* **10**, 2.

Howard RT., Cohen M. (1947). Quantitative metallography by point-counting and lineal analysis. *Transaction of AIME.* **172**, 413.

Howell PGT., Boyde A. (1994). Monte Carlo simulations of electron backscattering in lamellar bone. *Bone.* **15**, 285-291.

Ikeda S., Tsurukami H., Ito M., Sakai A., Sakata T., Nishida S., Takeda S., Shiraishi A., Nakamura T. (2001). Effect of trabecular bone contour on ultimate strength of lumbar vertebra after bilateral ovariectomy in rats. *Bone* **28**, 625-633.

Jaffe FF., Mankin HJ., Weiss C., Zarins A. (1974). Water binding in the articular cartilage of rabbits. *Journal of Bone and Joint Surgery – American Volumes.* **56**, 1031-1039.

Joyce-Loebl. (1985). Image analysis – Principles & practice. *Joyce-Loebl.* 24.

Kellgren JH., Lawrence JS. (1957). Radiographic assessment of osteoarthrosis. *Annals of the Rheumatic Diseases.* **16**, 494-501.

Kellgren JH., Moore R. (1952). Generalized osteoarthritis and heberden's nodes. *British Medical Journal.* **1**, 181-187.

Kellgren JH. (1961). Genetic Predisposition. *British Medical Journal* **2,1**.

Kellgren JH. (1961). Osteoarthritis in patients and populations. *British Medical Journal* **2,1**.

Keuttner K., Goldberg VM. (1995). *Osteoarthritic disorders* xxi-xxv. American Academy of Orthopedic Surgeons, Rosemont.

Kingsmill VJ., Boyde A. (1998). Mineralisation density of human mandibular bone: quantitative backscattered electron image analysis. *Journal of Anatomy.* **192**, 245-256.

Kingsmill VJ., Boyde A., Jones SJ. (1999). The resorption of vital and devitalized bone in vitro: significance for bone grafts. *Calcified Tissue International.* **64**, 253-256.

Kingsmill VJ., Boyde A. (2000). Osteoclastic resrorption of equine cranial and postcranial bone in vitro. *Journal of Bone Mineral Research.* **18**, 148-152.

Kinney JH., Lane NE., Haupt DL. (1995). In vivo, three-dimensional microscopy of trabecular bone. *Journal of Bone Mineral Research.* **10**, 264-270.

Layton MW., Goldstein SA., Goulet RW., Feldkamp LE., Kubinski DJ., Bole GG. (1988). Examination of subchondral bone architecture in experimental osteoarthritis by microscopic computed axial tomography. *Arthritis and Rheumatism*, **31**, 1400-1405.

Lawrence RC., Hochberg MC., Kelsey JL., McDuffie FC., Medsger TA Jr., Felts WR., Shulman LE. (1989). Estimates of the prevalence of selected arthritic and musculoskeletal diseases in the United States. *Journal of Rheumatology.* **16**, 427-441.

Lippiello L., Hall D., Mankin HJ. (1977). Collagen synthesis in normal and osteoarthritic human cartilage. *Journal of clinical Investigation.* **59**, 593.

Maki K., Miller., Okano T., Hatcher S., Yamaguchi T., Kobayashi H., Shibasaki Y. (2001). Cortical bone mineral density in asymmetrical mandibles: a three-dimensional quantitative computed tomography study. *European Journal of Orthodontics.* **23**, 217-232.

Mandelbrot BB. (1967). How long is the Coast of Britain. Statistical Self Similarity and Fractional Dimension. *Science.* **155**, 636-638.

Mankin HJ., Lippiello L. (1970). Nucleic acid and protein synthesis in epiphyseal plates of rachitic rats. An autoradiographic study. *Journal of Bone and Joint Surgery – American Volumes.* **52**, 424-434.

Mawhinney WHB., Ellis HA. (1983). A technique for plastic embedding of mineralised bone. *Journal of Clinical Pathology.* **36**, 1197-1199.

Mellish RWE., Ferguson-Pell MW., Cochran GVB., Lindsay R., Demptster DW. (1991). A new manual method for assessing two-dimensional cancellous bone structure: comparison between iliac crest and lumbar vertebra. *Journal of Bone Mineral Research.* **6**, 689-696.

Mudinger A., WiesmeierB., Dinkel E., Helwig A., Beck A., Moenting JS. (1993). Quantitative image analysis of vertebral body architecture - improved diagnosis in osteoporosis based on high resolution computed tomography. *British Journal of Radiology.* **66**, 209-213.

Muller G., Hanschke M. (1998). In vitro model of characterizing the effects of compressive loading on proteoglycans in anatomically intact articular cartilage. *Occupational Health and Industrial Medicine.* **38**, 2-2(1).

O'Brien FJ., Taylor D., Dickson GR., Lee TC. (2000). Visualisation of three-dimensional microcracks in compact bone. *Journal of Anatomy.* **197**, 413-420.

Oettmeier R., Abendroth K. (1989). Osteoarthritis and bone: osteologic types of osteoarthritis of the hip. *Skeletal Radiology.* **18**, 165-174.

Oloyede A., Flachsmann R., Broom ND. (1992). The dramatic influence of loading velocity on the compressive response of articular cartilage. *Connective Tissue Res*earch, **27**, 211-224.

Ostu N. (1978). A threshold selection method from grey-level histogram. *Transactions on Systems, Man and Cybernetics,* **SMC-8**, 62-66.

Parkinson IH., Fazzalari NL. (1994). Cancellous bone structure analysis using image analysis. A*ustralasian Physical & engineering Science in Medicine.* **17**, 64-70.

Parsons DF., Marko M., Leith A. (1990). The relative merits of direct morphometry of reconstructions of whole cells, and statistical morphometry by stereology of random sections of cells. *Cell Biophysics.* **17**, 227-242.

Pritzker KPH. (1998). Osteoarthritis. *Oxford University Press.* 50-61.

Radin EL., Paul IL. (1970). Does cartilage compliance reoduce skeletal impact loads? The relative force-attenuating properties of articular cartilage, synovial fluid, periarticular soft tissue and bone. *Arthritis and Rheumatism,* **13**, 139-144.

Radin EL., Paul IL. (1971). Importance of bone in sparing articular cartilage from impact. *Clinical Orthopaedics and Related Research.* **78**, 342-344.

Radin EL., Parker HG., Paul IL. (1971). Pattern of degenerative arthritis. Preferential involvement of distal finger-joints. *Lancet,* **1**, 377-379.

Radin EL. (1972-73). The physiology and degeneration of joints. *Seminars Arthritis and Rheumatology* **2**, 245-257.

Radin EL., Paul IL., Rose RM. (1972). Role of mechanical factors in pathogeneses of primary osteoarthritis. *The Lancet,* **1**, 519-522.

Radin EL., Rose RM. (1986). Role of subchondral bone in the initiation and progression of cartilage damage. *Clinical Orthopaedics and Related Research,* **213**, 34-40.

Reed MG., Howard CV. (1998). Surface-weighted star volume: concept and estimation. *Journal of Microscopy.* **190**, 350-356.

Resnick D. (1988). Common disorders of synovium-lined joints: pathogenesis, imaging abnormalities, and complications. *American Journal of Roentgenology* **151**, 1079-1093.

Russ JC. (1995). The image processing handbook. Second edition. *CRC Press.*

Schnitzler. (1993). Bone Quality: A Determinant for certain risk factors for bone fragility. *Calcified Tissue International.* **53**, S27-S31.

Serra J. (1982). Image analysis and mathematical morphology. *London, Academic Press.*

Silberberg R (1990). Diseases of Joints. *Anderson's Pathology Volume 2* 2071-2074.

Sokoloff L. (1979). The Aetiopathogenesis of Osteoarthritis. *Pitman Medical publishing.* 1-15.

Stecher RM (1941). Heberden's nodes. Heredity in hypertrophic arthritis of the finger joints. *American Journal of Medical Science.* **201**, 801-809.

Vesterby A., Gunderson HJG., Melson J. (1989). Star volume of marrow space and trabeculae of the first lumber vertebra. *Bone* **10**, 7-13.

van Gieson I. (1889) Laboratory notes and technical methods for the nervous system. *New York Medical Journal.* **50**, 57.

van Saase JL., van Romunde LK., Cats A., Vandenbroucke JP., Valkenburg HA. (1989). Epidemiology of osteoarthritis: Zoetermeer survey. Comparison of radiological osteoarthritis in a Dutch population with that in 10 other populations. *Annals of the Rheumatic Diseases.* **48**, 271-280.

Venn MF. (1979). Chemical composition of human femoral and head cartilage: influence of topographical position and fibrillation. *Annals of the Rheumatic Diseases.* **38**, 57-62.

Weibel ER. (1979). Stereological Methods. Practical Methods for Biological Morphometry Vol 1. *London Academic Press.*

Wenzel A. (1987). Effect of varying gray-scale resolution for detectability of bone lesions in intraoral radiographs digitized for teletransmission. *Scandinavian Journal of Dental Research* **95**, 483-492.

West BJ. (1990). Fractal physiology and chaos in medicine. Singapore: World Scientific.

Wolff J. (1892). The Law of Bone Remodelling. *Royal Academy, Berlin.*

Wootton R., Springgall DR., Polak JM. (1995). Image analysis in histology. Conventional and confocal microscopy. *Postgraduate Medical Science.*

Zaia J., Liu B., Boynton R., Barry F. (2000). Structural analysis of cartilage proteoglycans and glycoproteins using matrix-assisted laser desorption/ ionisation time-of-flight mass spectrometry. *Analytical Biochemistry.* **277**, 94-103.

Glossary

&

Appendices

Definition of image analysis terminology

A full explanation of all image analysis terminology would be exhaustive and superfluous. Below is an explanation of the image analysis terminology and system commands relevant to this study.

The VIDAS system interpreter is case sensitive. Some commands are in uppercase others in lowercase.

AREA

The number of pixels in an object multiplied by the scaled pixel area.

Binary image

All pixels in an image are represented by either, 0 for black, or 1 for white. In an image analyser the value given to white is usually 255.

Boolean operators

Are operations carried out on a binary image, which follow clearly defined logical rules i.e. AND, OR, XOR & NOT. These functions are used to correlate two binary images.

CGRAVX

Coordinate of the centre of gravity of an object in the X plane. Measured in pixels with coordinate 0,0 being in the upper-left corner on the image. The variable is of real type and is obtained by summation over the area of the object as: $CGRAVX = \frac{\sum_{obj} x_i}{AREA(pixels)}$.

CGRAVY

Coordinate of the centre of gravity of an object in the Y plane. Measured in pixels with coordinate 0,0 being in the upper-left corner on the image. The variable is of real type and is obtained by summation over the area of the object as: $CGRAVY = \frac{\sum_{obj} y_i}{AREA(pixels)}$.

Classification

The logical sorting of image data into definable differentiated bins. We use the image analyser to try to extract unique information from an object within a field to create a feature of the object. This information can then be used to identify the feature in another field.

contour

Command used to extract the outside contour of a binary image.

Contrast adjustment (normim)

A greyscale processing function that increases the contrast of the image by scaling the grey values linearly into the full dynamic range of the image memory. The limits of the grey value range are adjusted according to: $N_{low} = N_{high} = \frac{Threshold}{2000} N_{tot}$

where; N_{low}, N_{high} = cumulated number of pixels with grey values lower or higher than the normalisation limits.

N_{tot} = total number of pixels in the image.

$Threshold$ = thousandths of the maximum frequency in the grey value histogram (typical range is 1-10).

Values that are >255 or <0, are usually clipped to exclude scattered noise pixels from re-scaling.

Digital greyscale image

The VIDAS system is capable of capturing and processing 8 bit images. Each pixel in an 8 bit image can have a value from 0 – 255, resulting in an image with 256 discrete greylevels. The value 0, representing pure black and 255 representing pure white. The spatial resolution is variable, but in this study all image sizes were either 512 x 512 or 768 x 512 pixels.

Digitise

The process in which an image is collected via a camera and a digital representation of its analogue form created. This digital image can be stored in the computers memory (Frame store) and further processed.

dilate

Can be applied to any grey value. Particularly useful in binary processing. The function can dilate the outside layer of a binary object. The command can be iterated. The type of dilation can be set by adjusting the kernel shape i.e.

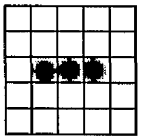
1

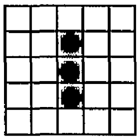
2

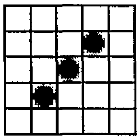
3

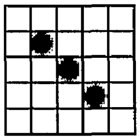
4

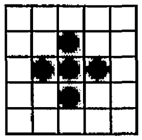
5

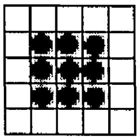
6

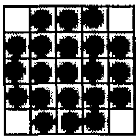
7

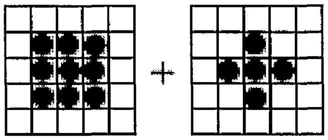
8

This study only used dilation and erosion on binary images, therefore no grey texture was required to be taken into account. This study always used kernel shape 7.

DMAX

Maximum diameter of an object. DMAX can be described, as pulling a pair of callipers over an object in the longest possible dimension. The system determines this measurement by selecting the largest Feret diameter measured in 32 different directions.

DMIN

Minimum diameter of an object. Same as DMAX, only selecting the shortest Feret diameter.

erode

Opposite of dilate (see above).

Feature Vectors

The set of measurement parameters. Divided into field specific or object specific measurements.

FCIRCLE

Circularity form factor. Measures how much an objects shape deviates from a circle. $FCIRCLE = \frac{4\pi AREA}{PERIM^2}$.

FERETX

The distance between two parallel tangents in the X plane.

FERETY

The distance between two parallel tangents in the Y plane.

FIELDCOUNT

A field based internal measurement parameter that counts the total number of “identified” objects in a binary image.

fill

Binary function used to fill holes within binary objects.

for–endfor

Programming loop that executes for a specified number of times.

Frame grabber

A hardware device used to convert an analogue video image into a digital form. These electronic digital images can be dynamically stored and further processed.

Frame store

The RAM installed in a frame grabber. Used to store digital images. The number of images stored in the frame store is dependant on the image size and the amount of installed RAM. The VIDAS system's frame grabber can store 12 images at 512 x 512 pixels. More up-to-date systems use the computers' system RAM for storing images.

Grabbed or grab

Action carried out by frame grabber. See frame grabber.

Identify or identified images

Connectivity test. Defines separate binary objects in an image. Each binary object is given an individual value label of one of the 256 grey scale values (except 0, which is the value given to the background). This greylevel will be common to all pixels in that object. A special LUT called "ident" is applied, which displays neighbouring objects in contrasting colours. The variable Conn_8 is used to define the nature of connectivity. If the variable is true, connecting pixels at 45° will be considered to be connected. If the variable is false these pixels will be considered a separate object i.e.

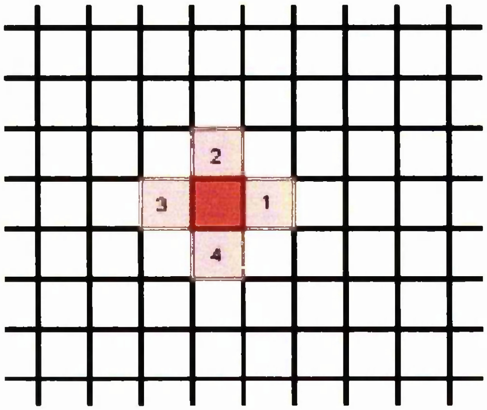

4-Connectivity

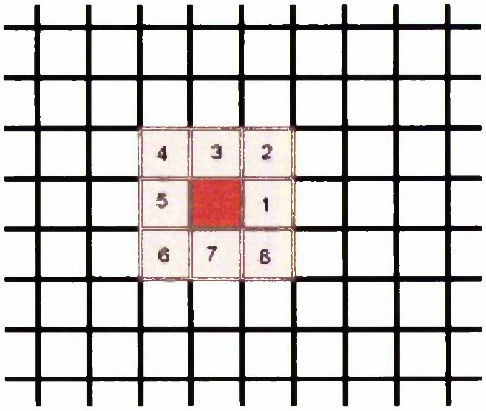

8-Connectivity

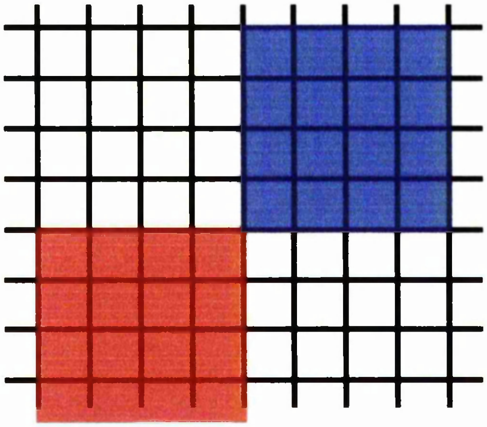

4-Connectivity. Two objects.

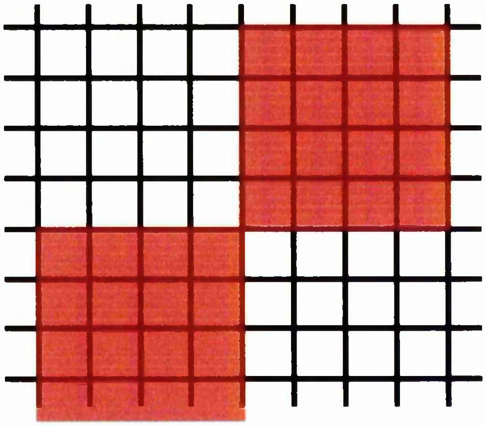

8-Connectivity. One Object.

This study always set the variable Conn_8 = true (8-Connectivity).

if–endif

Conditional programming nest.

Integer

Type of variable. Must be a whole number. Usually used in programming for counting iterations e.g. variable *x* = *1*.

Interpreter

A computer interface that allows a user to program the processor using a high level language.

Invert

Each pixel has its grey value inverted e.g. 255 becomes 0, 254 becomes 1, 253 becomes 2...etc.

Look up tables (LUT)

Each 8 bit image is represented by 256 values. Usually, in a greyscale image, these values are represented by a grey shade from 0, representing pure black and 255 representing pure white. Special LUT's can be constructed to apply different values to each of the 256 values e.g. colours can be applied instead of a grey shade. This tool can be used to make the visualisation of certain features easier to the human eye.

Macro

Macro is the term given to a list of commands that are executed, in order, by a computer. An image analyser cannot perform complex tasks without programming the system. Various different methods of programming image analysers have been developed by manufactures, to facilitate the programming of their systems. The simplest form of recording a macro is to simply record the order in which menu items are selected. This is easy for any non-programmer to do, but the functionality and power of these systems are restricted. Another well-used method is the icon/ flow method. Icons, which perform imaging routines, are dragged onto a flow line. These flow lines can be looped and fairly complex routines can be set-up. The most commonly used method, is that of a system that provides a high level programming language e.g. "PASCAL", "BASIC" or "C", which can be scripted in executable lines. These high level languages, provided in image analysis systems, usually provide special imaging commands unique to image analysis, resulting in a proprietary based macro scripting tool. The system used in this project, VIDAS 2.5 by Kontron Elektronik GmbH, uses such a system. It is a proprietary scripting programming language with a syntax closely related to the programming language "C". The interface, which allows the user to program the system, is called the "Interpreter".

mask

Masks the contents of a grey or binary image with the contents of a binary image. The command can select the area below the mask or the area outside the mask.

Measf

A function used to measure all objects defined in a field feature vector.

Measo

A function used usually nested within a while – endwhile loop, to instruct the image analyser to measure the next available identified object.

Object/ features

A describable and separate individual component in an image. In a binary image the objects or features must be "identified".

Overlay graphics/ graphics plane.

Terminology given to operations that allow vector graphics to be superimposed over the greyscale image. A binary image can be converted into the graphics plane and displayed as an overlay graphic. An overlay graphic can be converted into a binary image.

Pixel

The smallest spatially-digitised unit of an image. A single pixel has a single grey level.

Real

Type of variable. Usually used in programming to hold a real number value e.g. variable $x = 2.4567$.

rotate

Command used to perform programmed geometric spatial distortions in an image. This command was used to "shrink" binary objects.

Scaling factors

A geometric scaling can be input into the system. This calibration is done in the X and Y direction to eliminate any distortion in the XY planes. A scale bar is placed under the camera at the same distance and magnification as the specimen. The unit type is input. In essence this procedure tells the system how many pixels in the X and Y direction are equal to the scale unit: $ScaleX = \frac{units}{pixel}$ $ScaleY = \frac{units}{pixel}$

This study did not use any densitometric scaling.

scrap

The function used to eliminate or select defined objects, by area, in a binary image.

Segmentation

Extraction of features within a grey scale image into meaningful regions. Objects are usually converted to a binary representation. The process of segmentation is called "Thresholding". Many different methods of thresholding are available but can be divided into two main categories: point dependant techniques and region dependant techniques. In this project we only used point dependant methods. Point dependent thresholding (PDT) is where each pixel is labelled according to its greylevel. This study used two methods of PDT: two-threshold levels and dynamic thresholding.

The two-threshold levels method discriminates objects, from the background, by setting two thresholds. The VIDAS system uses a greylevel threshold method (Chow *et al.*, 1972) & (Ostu, N 1978). The threshold limits can be selected numerically (set within the macro) or interactively. The output image is either binary or its original greylevel. The dynamic thresholding method generates a binary image by computing a single adaptive threshold. Local noise is removed from the image by subtracting a low pass filtered image, of the original, from the original. By adjusting the size of the matrix, of the low pass filter, objects in selected size ranges can be discriminated. This form of thresholding is particularly useful for thresholding small objects from a varying background. This was the method used to threshold trabecular bone.

Shade correction

Most lenses will pass more light through the centre than at the edges. This can produce a shading effect on the periphery of the image. If a reference image is grabbed (usually a blank screen), this image can be subtracted from the object image, resulting in a corrected image.

Skeletonised

A technique applied to a binary image, which results in the image being eroded or thinned down to a single pixel in thickness.

String

Type of variable. Usually used in programming to hold a text value e.g. variable *x* = *"specimen name"*.

Threshold

A grey level value which separates regions of interest from the background. Usually used to convert the selected grey level(s) to a binary representation.

TOTALAREA

A field based internal measurement parameter that sums the area of all "identified" objects in a binary image.

Variable

Used in computer programming to assign particular programming values. Three types: integer, real and string.

while–endwhile loop

Computer programming function that has programming code between the while and the endwhile markers. The code is continually executed in a loop until a condition is true.

APPENDIX A

Image analysis macro program – Femoral Head

```
#####################################################
#   Macro to measure the intertrabecular spaces in femoral head
#   within 4 separate sectors of a ROI.
#
#   Author - Matt Neilson
#   IBLS
#   University of Glasgow
#####################################################
tvchan 3,3
clearmes
resetvec
resetpar
InitDios AREA,FERETX,FERETY,DMAX,DMIN,FCIRCLE
global rabarea,ferx,fery,form,max,min,mag,magt,spec,specim,avetrab,avecnt
trabarea=avetrab=avecnt=ferx=fery=form=mag=magt=max=min=0.0
spec=specim ="spec"
trab[]=spec,trabarea,ferx,fery,max,min,form,avetrab
reply ="Y"
x=y=0
clall
loadlut "grey"
setframe "F512"
beep 300,900
beep 400,1700
adjustint 255,65,_OFF
while 1
 x=0
 loadlut "grey"
 clearmes
 clall
 ovcolour 3
 tvon
 beep 100,1000
 beep 100,1000
 write
 write "FRAME SECTOR THEN PUT SCALE BAR UNDER THE CAMERA"
 pause
 tvinp 5
 gscaldef 5,"bonetrab",1.0,1.0,"mm",_ON,_ON
 gscalsel "bonetrab",_OFF
 clearmes
```

```
write
read "TYPE IN MAGNIFICATION FACTOR ";mag
setframe "F768"
clearmes
read "ENTER THE NAME OF THE SPECIMEN ";specim
while 1
  x=x+1
  If x==5:break
  clall
  tvon
  loadlut "grey"
  spec=specim+ string(x)
  clearmes
  write "Database will be ";spec
  beep 100,1000
  beep 100,1000
  write "PUT TRACING UNDER THE CAMERA ON AREA ";x
  pause
  tvinp 1
  normim 1,2,20
  clearmes
  beep 100,1000
  beep 100,1000
  write "DISCRIMINATE  !!!"
  dis2lev 2,3,0,175,_ON,_OFF,3
  write
  beep 100,1000
  beep 100,1000
  write "DRAW ROUND THE AREA"
  basicmask 2,4
  mask 3,4,5,255,0,_ON
  display 5
  scrap 5,5,_OFF,0,22,_ON,_ON
  display 6
  fill 5,6
  display 3
  erode 6,3,7,255,2
  identify 3,3,_ON,_OFF
  erode 3,3,7,0,2
  DBerase spec
  DBcreate spec,"trab"
  y=0
  avecnt=0.0
  magt=(mag*mag)
  while 1
    y=y+1
    Measo 3
    if _STATUS:break
    trabarea=(AREA/magt)
    ferx=(FERETX/mag)
```

```
     fery=(FERETY/mag)
     form=FCIRCLE
     max=(DMAX/mag)
     min=(DMIN/mag)
     avecnt=avecnt+trabarea
     avetrab=avecnt/y
     DBopen spec,"trab"
     DBappend spec
   endwhile
   DBclose spec
 endwhile
 for x=1, x<5, x=x+1
   spec=specim +string(x)
   outlist spec,_OFF
 endfor
 x=0
 clearmes
 write
 beep  200,1000
 beep 200,1000
 read "DO YOU WANT TO INPUT ANOTHER SET (Y/N) ";reply
 If reply == "N" | | reply =="n":break
endwhile
beep 200,1000
beep 300,1000
clearmes
write
write "END OF MACRO!!!!!"
```

APPENDIX B

Image analysis macro – Femoral neck

```
#####################################################
#  Macro to measure the morphology, distribution and
#  connectivity of cortical and medullary bone in the human
#  femoral neck.
#  Author - Matt Neilson
#  IBLS
#  University of Glasgow
#####################################################
tvchan 3,3
clearmes
resetpar
clall
setframe "F768"
loadlut "grey"
beep 300,900
beep 400,1700
adjustint 255,65,_OFF
clearmes
clall
ovcolour 3
InitDios AREA,CGRAVX,CGRAVY
InitField FIELDCOUNT,TOTALAREA
global cx,cy,Sector,Sectarea,Sarea,SAsectA,SAMA,Cortical,Trabecular,TotalBone
global TotalSect,Perc,Ratio,NoProf,ArProf,PTrb,PTrm,PCort,MedArea,Specimen
Sector=0
Sarea=Sectarea=Cortical=Trabecular=TotalBone=Perc=TotalSect=Ratio=NoProf=0.0
ArProf=PTrb=PTrm=PCort=MedArea=0.0
Specimen="name"
bone[]=Specimen,TotalSect,TotalBone,MedArea,Cortical,Trabecular,Perc,PCort,PTrb,PTrm,Ratio,NoProf, ArProf
while 1
 clall
 clearmes
 write ""
 read "TYPE IN THE NAME OF THE SPECIMEN ";Specimen
 clearmes
 loadlut "grey"
 tvon
 write ""
 write "PUT SCALE BAR UNDER THE CAMERA"
 pause
```

```
tvinp 1
gscaldef 1,"bone1",1.0,1.0,"mm",_ON,_ON
gscalsel "bone1",_OFF
clearallov
clearmes
write “”
write "SET LIGHT !!! "
loadlut "bone1"
getim "bonelite",3
tvalign 1,_ON,_ON
clearmes
loadlut "grey"
write ""
write "PUT SPECIMEN THEN BLANK SLIDE UNDER THE CAMERA"
tvon
pause
tvinp 1
shaddef 1,6
clearmes
write ""
write "PUT SPECIMEN UNDER THE CAMERA"
tvon
pause
tvinp 2
clearallov
reply :="Y"
tvoff
shadcorr 2,1,6,_ON,0
normim 1,2,10
 while 1
   clovl 2
   loadlut "grey"
   clearmes
   write ""
   write "CORTICAL BONE - THRESHOLDING "
   write "SEGMENT DARK AREAS"
   dis2lev 2,3,0,94,_ON,_ON,3
   clearmes
   write ""
   reply="Y"
   read "DO YOU WANT TO THRESHOLD LIGHTER SHADES (Y/N) ";reply
   if reply =="y" || reply =="Y"
      dis2lev 2,4,0,120,_ON,_ON,3
      clearmes
      write ""
      write "DRAW ROUND OVER SEGMENTED AREA TO BE ERASED"
      write "SPACE for NEXT STEP     END to finish"
```

```
    eraseinside 4,5,1,0
    display 3
    add 3,5,3,2
  endif
  scrap 3,3,_OFF,0,40,_ON,_ON
  clearmes
  write ""
  write "JOIN UP ANY GAPS"
  write "SPACE for NEXT STEP    ENTER FOR AUTOCLOSE"
  write "END to finish"
  combine 3,2,6,,0.5,0.5
  basicmask 6,4
  display 3
  add 4,3,4,2
  dilate 5,6,7,255,2
  fill 6,6
  erode 6,6,7,255,4
  scrap 6,6,_OFF,0,30000,_ON,_ON
  clearmes
  reply:="Y"
  read "Are you happy !!";reply
  if reply =="y" | | reply =="Y":break
 endwhile
identify 6,6,_ON,_OFF
measobj 6,"data",_OFF
DBopen "data","data"
DBread "data"
write AREA
TotalSect=AREA
loadlut "grey"
dis2lev 6,6,1,4,_ON,_OFF,1
display 2
clearmes
write "TRABECULAR BONE - DARK or FULL THRESHOLDING"
disdyn 2,5,5,9,_ON,_OFF,_ON
clearmes
write ""
scrap 5,5,_OFF,0,5,_ON,_ON
reply :="Y"
 while 1
  clearmes
  reply="Y"
  read "DO YOU WANT TO ADD 2nd THRESHOLDING (Y/N)
  ";reply
  if reply =="n"  | |reply =="N":break
  write "THRESHOLD LIGHT AREAS"
  disdyn 2,6,5,23,_ON,_OFF,_ON
  clearmes
  write "DRAW ROUND LIGHT SEGMENTED AREA TO BE
  RETAINED "
```

```
    eraseoutside 6,6,1,0
    scrap 6,6,_OFF,0,10,_ON,_ON
    add 5,6,5,2
    clearmes
    display 5
    reply="Y"
    read "ARE YOU HAPPY WITH THIS SEGMENTATION (Y/N) ";reply
    if reply =="y" || reply =="Y":break
  endwhile
reply ="y"
loadlut "grey"
clearmes
write "CREATING MEDULLA MASK"
close 4,4,7,255,3
scrap 4,4,_OFF,0,500,_ON,_ON
xorim 6,4,1
scrap 1,1,_OFF,0,1200,_ON,_ON
dilate 1,1,7,255,1
fill 1,1
erode 1,1,7,255,1
measobj 1,"data",_OFF
DBopen "data","datak"
DBread "data"
MedArea=AREA
identify 1,1,_ON,_OFF
gscalsel "1:1-scale",_OFF
measobj 1,"data",_OFF
DBopen "data","data"
DBread "data"
cx=int(CGRAVX)
cy=int(CGRAVY)
dis2lev 1,1,1,255,_ON,_OFF,1
loadlut "grey"
mask 5,1,5,255,0,_ON
scrap 5,5,_OFF,0,5,_ON,_ON
identify 5,5,_ON,_OFF
gscalsel "bone1",_OFF
measfield 5,"data",_OFF
DBopen "data","data"
DBread "data"
Trabecular=TOTALAREA
NoProf=FIELDCOUNT
ArProf=Trabecular/NoProf
display 3
clearmes
mask 3,4,3,255,0,_ON
mask 3,1,3,255,0,_OFF
identify 3,3,_ON,_OFF
measfield 3,"data",_OFF
```

```
DBopen "data","datak"
DBread "data"
Cortical=TOTALAREA
Perc=((Cortical+Trabecular)/TotalSect)*100
Ratio=Cortical/Trabecular
TotalBone=Cortical+Trabecular
PTrb=((Trabecular/TotalSect)*100)
PCort=((Cortical/TotalSect)*100)
PTrm=((Trabecular/MedArea)*100)
pause
DBcreate "boneDB1","bone"
DBopen "boneDB1","bone"
DBappend "boneDB1"
outlist "boneDB1",_OFF
clearallov
clear 6
clear 2
clearmes
display 2
write
write "CREATING MEDULLA SECTOR AREAS................"
loadlut "grey"
step=15
for i=1,i<360/step,i=i+2
  a = cx+int(550*cos(step*i/_DEG))
  b = cy-int(550*sin(step*i/_DEG))
  Gvector 2,cx,cy,a,b,255
endfor
erode 2,2,5,0,1
subtract 1,2,6,2
cga=int(cx/3)
cgb=int(cy/3)
cgx=int(cx/1.25)
cgy=int(cy/1.25)
write "USING 'rotate' TO SHRINK BINARY IMAGE........."
display 2
rotate 1,2,cx,cy,0.0,0.66,0.66,-cga,-cgb,_OFF
display 6
contour 2,6,6,7,0,_OFF,_ON
display 1
rotate 1,2,cx,cy,0.0,0.2,0.2,-cgx,-cgy,_OFF
orim 2,6,6
display 2
contour 2,6,6,7,0,_OFF,_ON
subtract 6,4,4,3
clearmes
write
write "PLOTTING IMAGE"
plotim 4,3,_OFF,0.0,0.0,4.5,4.5,_ON,_OFF,_ON,_OFF,"name"
clearmes
```

```
write
write "IDENTIFYING MEDULLA SECTORS............"
identify 6,6,_ON,_OFF
erode 6,6,5,0,2
clearmes
mask 6,2,6,255,0,_OFF
copy 2,4
clear 2
write
write "CREATING MAIN MASKS...................."
for i=1,i<360/step,i=i+2
  a = cx+int(550*cos(step*i/_DEG))
  b = cy-int(550*sin(step*i/_DEG))
  Gvector 2,cx,cy,a,b,255
endfor
invert 2,2
erode 2,2,5,255,1
identify 2,2,_ON,_OFF
erode 2,2,5,0,2
clearmes
write
write "MEASURING TRABECULAR BONE DISTRIBUTION........."
dbo=Specimen+"O"
dbm=Specimen+"M"
dbi=Specimen+"I"
DBerase dbo
DBerase dbm
DBerase dbi
SAMA=Sarea=Sectarea=SAsectA=0.0
Sector=t=0
dis[]=Sector,Sarea,Sectarea,SAsectA,SAMA,MedArea
DBcreate dbo,"dis"
DBcreate dbm,"dis"
DBcreate dbi,"dis"
gscalsel "bone1",_OFF
display 4
Measo 4
Sectarea=AREA
mask 5,4,4,1,0,_ON
Measf 4
Sector=25
Sarea=TOTALAREA
SAsectA=Sarea/Sectarea
SAMA=SAsectA/MedArea
DBopen dbi,"dis"
DBappend dbi
for i=2,i<14,i=i+1
  clearmes
  write
  write "MAIN MASK ";i-1;" MASKING MEDULLA SECTORS"
```

```
clear 1
mask 6,2,1,i,0,_ON
display 1
while 1
   measstop
   Measo 1
   if _STATUS:break
   Sectarea=AREA
   clearmes
   write "MEASURING SECTOR AREA....................."
   mask 5,1,4,1,0,_ON
   display 4
   write
   write "MEASURING TRABECULAR BONE AREA............"
   Measf 4
   Sarea=TOTALAREA
   SAsectA=Sarea/Sectarea
   SAMA=SAsectA/MedArea
   display 1
   scalim 1,1,1,1,0,0,0,255,1
   if Sectarea>4.5
      t=t+1
      if t==1:Sector=1
      if t==2:Sector=13
      if t==3:Sector=2
      if t==4:Sector=14
      if t==5:Sector=3
      if t==6:Sector=15
      if t==7:Sector=4
      if t==8:Sector=16
      if t==9:Sector=5
      if t==10:Sector=17
      if t==11:Sector=6
      if t==12:Sector=18
      if t==13:Sector=12
      if t==14:Sector=24
      if t==15:Sector=23
      if t==16:Sector=11
      if t==17:Sector=19
      if t==18:Sector=7
      if t==19:Sector=22
      if t==20:Sector=10
      if t==21:Sector=20
      if t==22:Sector=8
      if t==23:Sector=21
      if t==24:Sector=9
      if Sector <13
         DBopen dbo,"dis"
         DBappend dbo
      endif
```

```
      if Sector >12 && Sector <25
        DBopen dbm,"dis"
        DBappend dbm
      endif
    endif
  endwhile
endfor
outlist dbo,_OFF
outlist dbm,_OFF
outlist dbi,_OFF
outhist dbo,"SAMA",10,_OFF,_OFF,0,_ON,_ON,0.00,
100.00,100.00,"","OUTSIDE"
outhist dbm,"SAMA",10,_OFF,_OFF,0,_ON,_ON,0.00,
100.00,100.00,"","MIDDLE"
display 2
clearmes
write
write "MEASURING CORTEX BONE DISTRIBUTION............."
resetvec "cortdis"
Sector=1
global SATS
SATS=0.0
dbc=Specimen+"C"
DBerase dbc
cortdis[]=Sector,Sarea,SATS
DBcreate dbc,"cortdis"
display 1
for i=2,i<14,i=i+1
  clearmes
  write
  write "MASKING CORTEX WITH MASK ";i-1
  mask 3,2,1,i,0,_ON
  if i-1==1:Sector=1
  if i-1==2:Sector=2
  if i-1==3:Sector=3
  if i-1==4:Sector=4
  if i-1==5:Sector=5
  if i-1==6:Sector=6
  if i-1==7:Sector=12
  if i-1==8:Sector=11
  if i-1==9:Sector=7
  if i-1==10:Sector=10
  if i-1==11:Sector=8
  if i-1==12:Sector=9
  Measf 1
  Sarea=TOTALAREA
  SATS=Sarea/TotalSect
  DBopen dbc,"cortdis"
  DBappend dbc
endfor
```

```
 outlist dbc,_OFF
 outscat dbc,"SATS",dbc,"Sector",_OFF,_OFF,_ON,_ON,0.00,
100.00,0.00,100.00,""
 loadlut "grey"
 clearmes
 beep 220,600
 beep 220,900
 beep 220,1200
 beep 100,1200
 beep 100,1200
 beep 350,1200
 write
 reply:="Y"
 read "Do you want to measure another slide (y/n) ";reply
 if reply =="n"||reply =="N":break
endwhile
write
write “END OF MACRO!!!!!”
```

APPENDIX C

Image analysis macro – Heberden's nodes

```
#####################################################
#  Macro to measure the morphology of Heberden's nodes on
#  phalanges of the little, middle and index fingers.
#
#  Author - Matt Neilson
#  IBLS
#  University of Glasgow
####################################################
resetvec
resetpar
tvchan 3,3
setframe "F512"
InitObj AREA,CGRAVX,CGRAVY,FCIRCLE,FERETX,FERETY
global acx,axy,bcx,bcy,name,base,raw,reply
global LEN1,LEN2,LEN3,LEN4,LEN5,LEN6,LEN7,LEN8,LEN9,
LEN10,LEN11,LEN12
global DLEN1,DLEN2,DLEN4,DLEN5,DLEN7,DLEN8,DLEN10,
DLEN11,CDLAT,CMLAT
name="spec1"
base="hebder"
raw="hebraw"
reply="y"
LEN1=LEN2=LEN3=LEN4=LEN5=LEN6=LEN7=LEN8=LEN9=
LEN10=LEN11=LEN12=0.0
DLEN1=DLEN2=DLEN4=DLEN5=DLEN7=DLEN8=DLEN10=
DLEN11=CDLAT=CMLAT=0.0
bonex[]=name,DLEN1,DLEN2,DLEN4,DLEN5,DLEN7,DLEN8,
DLEN10,DLEN11
bonraw[]=name,LEN1,LEN2,LEN3,LEN4,LEN5,LEN6,LEN7,
LEN8,LEN9,LEN10,LEN11,LEN12,CDLAT,CMLAT
while 1
 x=0
 clearmes
 read "ENTER THE NAME OF THE DERIVED DATABASE ";base
 write
 beep 1000,1000
 read "ENTER THE NAME OF THE RAW DATABASE ";raw
 clall
 loadlut "grey"
 tvon
 beep 600,1000
 clearmes
 write
 write "FOCUS & SET LIGHT"
```

```
pause
clearmes
beep 900,400
gscalsel "bone1",_OFF
write
read "DO YOU WANT TO ENTER A SCALE ";reply
if reply =="y"|| reply =="y"
  tvon
  beep 100,800
  beep 100,800
  write
  write "LINE UP SCALE BAR"
  pause
  tvinp 1
  gscaldef 1,"bone1",1.0,1.0,"mm",_ON,_ON
endif
clearmes
write
read "ENTER THE NAME OF THE SPECIMEN ";name
beep 500,900
while 1
  clall
  loadlut "grey"
  x=x+1
  gscalsel "1:1-scale",_OFF
  if x==1
     write
     write "LINE UP DISTAL POSTERIOR IMAGE &"
     write "POSITION SPECIMEN IN GRID"
  endif
  if x==2
     write
     write "LINE UP MIDDLE POSTERIOR IMAGE &"
     write "POSITION SPECIMEN IN GRID"
     beep 600,600
  endif
  tvon
  pause
  tvinp 1
  clearmes
  beep 500,800
  normim 1,2,10
  display 2
  disdyn 2,3,25,146,_ON,_ON,_ON
  display 4
  scrap 3,4,_OFF,0,20,_ON,_ON
  dilate 4,5,7,255,1
  display 5
  fill 5,6
  display 6
```

```
erode 6,7,7,255,1
display 7
beep 300,800
clearmes
copy 7,1
greyovl 1,2,3,1,255
copyovl 3,4
clearmes
beep 400,900
while 1
   write
   write "JOIN ANY GAPS"
   write "Space = Next Line"
   write "Enter = Autoclose"
   write "End    = End"
   drawline 3,4,0
   copyovl 4,5
   clear 5,0
   ovlgrey 5,1,6,255
   display 7
   fill 6,7
   write
   read "DO YOU WANT TO JOIN GAPS AGAIN (Y/N) ";reply
endwhile
scrap 7,7,_OFF,0,15800,_ON,_ON
clearmes
write
write "DRAW FIRST CO-ORD BOX"
write "Cursor = Frame Size"
write "End    = End"
beep 600,1000
clovl 8
drawframe 7,8,0,0,200,300,_ON
clear 8,0
ovlgrey 8,8,8,255
clovl 8
fill 8,8
mask 7,8,9,255,0,_ON
measobj 9,"bonbuf",_OFF
DBopen "bonbuf","buf"
DBread "bonbuf"
acx=int (CGRAVX)
acy=int (CGRAVY)
clearmes
write
write "DRAW 2nd CO-ORD BOX"
write "Cursor = Frame Size"
write "End    = End"
beep 600,1000
drawframe 7,8,0,0,200,300,_ON
```

```
clear 8,0
ovlgrey 8,8,8,255
clovl 8
fill 8,8
mask 7,8,9,255,0,_ON
measobj 9,"bonbuf",_OFF
DBopen "bonbuf","buf"
DBread "bonbuf"
bcx=int (CGRAVX)
bcy=int (CGRAVY)
clovl 7
display 7
if x==1:Gvector 7,(acx+270),acy,(bcx-20),bcy,-1
if x==2:Gvector 7,(acx+250),acy,(bcx-270),bcy,-1
wait 500
clearmes
beep 600,900
write
write "DRAW BOX AROUND BASE or HEAD of PHALANX"
write "Cursor = Frame Size"
write "End      = End"
drawframe 7,8,0,0,200,200,_ON
clear 9,0
copyovl 8,9
ovlgrey 9,9,9,255
clovl 9
fill 9,9
mask 7,9,10,255,0,_ON
erode 10,10,7,255,1
display 11
clear 11,0
copyovl 7,11
ovlgrey 11,11,11,255
clovl 11
mask 10,11,12,255,0,_OFF
display 12
identify 12,12,_ON,_OFF
erode 12,12,7,0,1
gscalsel "bone1",_OFF
DBopen "bonbuf","buf"
measobj 12,"bonbuf",_OFF
DBopen "bonbuf","buf"
DBup "bonbuf"
DBread "bonbuf"
if x==1
   LEN1=FERETY
   write LEN1
   DBread "bonbuf"
   LEN2=FERETY
endif
```

```
  if x==2
    LEN4=FERETY
    DBread "bonbuf"
    LEN5=FERETY
  endif
  clall
  beep 400,900
  beep 400,900
  if x==2:break
endwhile
x=2
while 1
  write x
  x=x+1
  loadlut "grey"
  clall
  beep 400,900
  beep 400,900
  if x==3
    write
    write "LINE UP LATERAL DISTAL IMAGE &"
    write "POSITION SPECIMEN IN GRID"
  endif
  if x==4
    write
    write "LINE UP LATERAL MIDDLE IMAGE &"
    write "POSITION SPECIMEN IN GRID"
  endif
  beep 600,600
  tvon
  pause
  tvinp 1
  clearmes
  beep 500,800
  normim 1,2,10
  disdyn 2,3,25,146,_ON,_ON,_ON
  display 4
  scrap 3,4,_OFF,0,20,_ON,_ON
  clearmes
  beep 800,400
  dilate 4,10,5,255,1
  fill 10,10
  clear 9
  erode 10,9,5,255,1
  clearmes
  copy 9,1
  greyovl 1,2,3,1,255
  copyovl 3,4
  clearmes
  beep 400,900
```

```
while 1
   write
   write "JOIN GAPS"
   write "Space = Next Line"
   write "Enter = Autoclose"
   write "End   = End"
   drawline 3,4,0
   copyovl 4,5
   clear 5,0
   ovlgrey 5,1,6,255
   display 7
   fill 6,7
   write
   read "DO YOU WANT TO JOIN GAPS AGAIN (Y/N) ";reply
   if reply =="n" | | reply =="N" :break
endwhile
scrap 7,7,_OFF,0,10500,_ON,_ON
clearmes
beep 800,400
write
write "DRAW BOX AROUND BASE or HEAD of PHALANX"
write "Cursor = Frame Size"
write "End    = End"
beep 600,1000
clovl 8
drawframe 7,8,0,0,200,300,_ON
clear 8,0
ovlgrey 8,8,8,255
clovl 8
fill 8,8
display 9
mask 7,8,9,255,0,_ON
erode 9,9,7,255,1
clearmes
beep 200,400
write
write "DRAW MIDLINE"
drawline 7,12,0
display 12
clear 12,0
ovlgrey 12,12,12,255
clovl 12
display 9
mask 9,12,9
erode 9,9,7,255,1
identify 9,9,_ON,_OFF
erode 9,9,7,0,2
if x==3
   measobj 9,"bonbuf",_OFF
   DBopen "bonbuf","buf"
```

```
     DBup “bonbuf”
     DBread "bonbuf"
     LEN7=FERETY
     write LEN7
     DBread "bonbuf"
     LEN7=FERETY
     write LEN8
     DBread "bonbuf"
     CDLAT=FERETX
     measobj 7,"bonbuf",_OFF
     DBopen "bonbuf","buf"
     DBread "bonbuf"
     CDLAT=FERETX
  endif
  if x==4
     measobj 9,"bonbuf",_OFF
     DBopen "bonbuf","buf"
     DBup “bonbuf”
     DBread "bonbuf"
     LEN7=FERETY
     write LEN7
     DBread "bonbuf"
     LEN7=FERETY
     write LEN8
     DBread "bonbuf"
     CMLAT=FERETX
     measobj 7,"bonbuf",_OFF
     DBopen "bonbuf","buf"
     DBread "bonbuf"
     CDLAT=FERETX
  endif
  DBclose "bonbuf"
  if x==4:break
endwhile
DLEN1=LEN1/CDLAT
DLEN2=LEN2/CDLAT
DLEN7=LEN7/CDLAT
CLEN8=LEN8/CDLAT
DLEN4=LEN4/CMLAT
DLEN5=LEN5/CMLAT
DLEN10=LEN10/CMLAT
DLEN11=LEN11/CMLAT
DBappend base
outlist base,_OFF
DBclose base
DBopen raw,"bonraw"
LEN3=LEN1+LEN2
LEN6=LEN4+LEN5
LEN9=LEN7+LEN8
LEN12=LEN10+LEN11
```

```
  DBappend raw
  outlist raw,_OFF
  DBclose raw
  clearmes
  beep 500,500
  beep 500,500
  write
  read "DO YOU WANT TO ENTER ANOTHER SPECIMEN ";reply
  if reply== "n"|| reply =="N":break
endwhile
beep 200,1000
beep 300,1000
clearmes
write
write "END OF MACRO!!!!!"
```

APPENDIX D

Modified van Gieson Stain.

De-wax and hydrate.	
Wash in water.	
Stain in Weigert's haematoxylin.	5 minutes
Blue in tap water.	
Differentiate in 1% acid alcohol (if necessary).	30 seconds
Blue in tap water.	
van Gieson.	3-5 minutes
Depending on specimen decalcification etc.	
Rinse in tap water. At least 5 minutes.	
Dehydrate in 90% alcohol and then absolute alcohol.	
Rinse rapidly in fresh absolute alcohol.	
Clear and mount.	

V.G Stain Preparation:

Picric acid sat. aqueous solution.	50ml
1% acid fuchsin aqueous solution.	9ml
Distilled water.	50ml